Modeling radiation belt electrons with information theory informed neural network

Simon Wing[1], Drew L. Turner[2], Aleksandr Y Ukhorskiy[3], Jay Robert Johnson[4], Thomas Sotirelis[5], Romina Nikoukar[6], and Giuseppe Romeo[1]

[1]Johns Hopkins University
[2]The Johns Hopkins University Applied Physics Laboratory
[3]Applied Physics Laboratory Johns Hopkins University
[4]Andrews University
[5]Johns Hopkins University Applied Physics Laboratory
[6]Johns Hopkins University Applied Physics Lab

November 22, 2022

Abstract

An empirical model of radiation belt relativistic electrons (m = 560–875 MeV G^{-1} and I = 0.088–0.14 R_E $G^{0.5}$) with average energy ~ 1.3 MeV is developed. The model inputs solar wind parameters (velocity, density, interplanetary magnetic field (IMF) |B|, Bz, and By), magnetospheric state parameters (SYM-H, AL), and L*. The model outputs radiation belt electron phase space density (PSD). The model is operational from L* = 3 to 6.5. The model is constructed with neural network assisted by information theory. Information theory is used to select the most effective and relevant solar wind and magnetospheric input parameters plus their lag times based on their information transfer to the PSD. Based on the test set, the model prediction efficiency (PE) increases with increasing L*, ranging from –0.043 at L* = 3 to 0.76 at L* = 6.5. The model PE is near 0 at L* = 3–4 because at this L* range, the solar wind and magnetospheric parameters transfer little information to the PSD. This baseline model complements well a class of empirical models that input data from Low Earth Orbit (LEO). Using solar wind observations at L1 and magnetospheric index (AL and SYM-H) models solely driven by solar wind, the radiation belt model can be used to forecast PSD 30–60 min ahead.

Modeling radiation belt electrons with information theory informed neural network

Simon Wing[1], Drew L. Turner[1], Aleksandr Y. Ukhorskiy[1], Jay R. Johnson[2], Thomas Sotirelis[1], Romina Nikoukar[1], and Giuseppe Romeo[1]

[1]The Johns Hopkins University, Applied Physics Laboratory, Laurel, Maryland, USA

[2]Andrews University, Berrien Spring, Michigan, USA

Abstract. An empirical model of radiation belt relativistic electrons (μ = 560–875 MeV G^{-1} and I = 0.088–0.14 R_E $G^{0.5}$) with average energy ~ 1.3 MeV is developed. The model inputs solar wind parameters (velocity, density, interplanetary magnetic field (IMF) |B|, Bz, and By), magnetospheric state parameters (SYM-H, AL), and L*. The model outputs radiation belt electron phase space density (PSD). The model is operational from L* = 3 to 6.5. The model is constructed with neural network assisted by information theory. Information theory is used to select the most effective and relevant solar wind and magnetospheric input parameters plus their lag times based on their information transfer to the PSD. Based on the test set, the model prediction efficiency (PE) increases with increasing L*, ranging from –0.043 at L* = 3 to 0.76 at L* = 6.5. The model PE is near 0 at L* = 3–4 because at this L* range, the solar wind and magnetospheric parameters transfer little information to the PSD. This baseline model complements well a class of empirical models that input data from Low Earth Orbit (LEO). Using solar wind observations at L1 and magnetospheric index (AL and SYM-H) models solely driven by solar wind, the radiation belt model can be used to forecast PSD 30–60 min ahead.

Plain Language Summary

An empirical model of radiation belt relativistic electrons with energy 1–2 MeV is developed. The model inputs solar wind parameters, magnetospheric state parameters, and L*. L* gives a measure of radial distance from the center of the Earth with a unit of R_E (radius of the Earth = 6378 km). The model outputs radiation belt electron phase space density (PSD). The model is operational from L* = 3 to L* 6.5. The model is constructed with information theory informed neural network. Information theory is used to select the relevant solar wind and magnetospheric parameters and their lag times based on the amount of information they provide to the radiation belt electrons. The model performance increases with increasing radial distance (L*) because at distances close to Earth (L* = 3–4) the solar wind and magnetospheric parameters provide little information about the radiation belt electron PSD. The model can be used to forecast radiation belt PSD 30–60 min ahead.

ORCID ID: 0000-0001-9342-1813

Keywords: radiation belt, relativistic electrons, solar wind drivers, machine learning, information theory, empirical model, phase space density.

Index terms: 2774, 2784, 2720, 2730, 4499

Broad Implications: A radiation belt relativistic electron model based on neural network assisted by information theory is developed. The model performs well and complements a class of empirical models that input observations from LEO.

Key points: (1) An empirical model to predict state of radiation belt relativistic electrons is developed; (2) The model PE increases with increasing L* with a max of 0.76 at L* = 6.5; (3) The model complements a class of empirical models that input observations from LEO.

1. Introduction

The Earth's radiation belts are populated by electrons having energies of hundreds of keVs to several MeVs or even higher. These electrons are hazardous to satellites that encounter them in the inner-magnetosphere r ~1.2–8 R_E, including at the geosynchronous orbit (GEO), and at their foot points at low earth orbit (LEO) in the ionosphere, where 1 R_E = radius of the Earth = 6378 km. The MeV electrons can penetrate deep into spacecraft systems, leading to anomalous system, subsystem, or payload malfunctions while those with energies < 1 MeV can accumulate on or near the surface of the spacecraft structure, leading to potentially hazardous electrical discharges.

It has long been recognized that the variabilities of the radiation belt electrons, to a large extent, are driven ultimately by variability of the solar wind (e.g., *Baker et al*., 1990, 2018; 2019; *Li et al*., 2001; 2005; *Reeves*, 2007; *Ukhorskiy et al*., 2004; *Reeves et al.*, 2013; *Xiang et al*., 2017; *Pinto et al*., 2018; *Zhao et al*., 2017, *Alves et al*., 2017). However, many solar wind parameters positively and negatively correlate with one another, which can complicate the interpretation as to which solar wind parameters are the real drivers and which parameters are only coincidentally correlated with the radiation belt electrons (e.g., *Wing et al*., 2016; *Wing and Johnson*, 2019; *Borovsky*, 2018; 2020; *Maggiolo et al*., 2017; *Wing et al*., 2021). For example, solar wind velocity (V_{sw}) positively correlates with radiation belt electron fluxes (J_e) (e.g., *Baker et al*., 1990; *Reeves et al*., 2011; *Balikhin et al*., 2011; *Paulikas and Blake*, 1979; *Li et al*., 2001; 2005; *Wing et al*., 2016; 2020). Solar wind density (n_{sw}) negatively correlates with radiation belt J_e (e.g., Li et al., 2005; *Lyatsky and Kazanov*, 2008a; *Kellerman and Shprits*, 2012; *Rigler et al*., 2007; *Balikhin et al*., 2011; *Wing et al*., 2016; 2020). However, V_{sw} negatively correlates with n_{sw} (e.g., *Wing et al*., 2016; 2021; *Borovsky*, 2020).

Radiation belt electrons also have strong dependences on the magnetospheric state, which

can be proxied by geomagnetic activity indices such as SYM-H and AL (e.g., *Reeves et al*., 1998; *Baker et al.*, 2019; *Lyatsky and Khazanov*, 2008b; *Borovsky and Denton*, 2014; *Tang et al*., 2017b; *Borovsky*, 2017; *Zhao et al*., 2017). SYM-H index gives a measure of the strength of the ring current and geomagnetic storms (*Iyemori*, 1990) while AL gives a measure of the strength of the westward auroral electrojets and substorms (*Davis and Sugiura*, 1966). SYM-H is similar to Disturbance Storm Time (Dst) index (*Dessler and Parker*, 1959), except that SYM-H index has one minute time resolution whereas Dst index has one hour resolution. Unfortunately, SYM-H and AL both also correlate with solar wind parameters, which raises the question how much additional unique information these two magnetic indices provide to the radiation belt electrons and what their response lag times may be, given the solar wind parameters (*Wing et al*., 2021).

Wing et al. (2016; 2021) showed that information theoretic tool such as conditional mutual information can be quite useful to untangle the intertwined solar wind and magnetospheric drivers of the radiation belt electrons. They were able to isolate the effect of individual drivers and their response lag times. Moreover, they ranked the solar wind and magnetospheric parameters based on the information transfer of these parameters to the radiation belt J_e (*Wing et al.*, 2016) and more recently, electron phase space density (PSD) (*Wing et al*., 2021). Thus, those studies provided relevant and useful information for radiation belt modeling.

Machine learning algorithms such as neural networks (NN) and deep learning (*Rumelhart and McClelland*, 1987; *Schmidhuber*, 2015) has found wide applications in space weather, particularly in empirical modeling. For example, NN have been used to develop models for Kp (e.g., *Boberg et al*., 2000; *Wing et al*., 2005; *Wintoft et al*., 2017), geomagnetic storm (*Wu and Lundstedt*, 1997), source regions of particle precipitation (*Newell et al*., 1990; 1991), high-frequency (HF) backscattered signals (*Wing et al*., 2003). NN have also been used to construct

empirical radiation belt models (e.g., *Koons and Gorney*, 1991; *Perry et al*., 2010; *Ling et al*., 2010; *Smirnov et al*., 2020; *Claudepierre and O'Brien*, 2020; *Pires de Lima et al*., 2020; *Chen et al*., 2019; *Simms and Engebretson*, 2020). These empirical models generally complement physics-based models, e.g., DREAM (*Reeves et al.*, 2012), SPACECAST (*Horne et al*., 2013), VERB (*Shprits et al*. 2009) and other empirical models that use different approaches, e.g., NARMAX (*Wei et al*., 2011; *Balikhin et al*., 2016), Kalman filter (*Coleman et al*., 2018), linear prediction filter (*Baker et al*., 1990; *Kellerman et al*., 2012; *Chen et al*., 2019). For operational purpose, one may need to consider trade-offs among accuracy, computational speed, computing resource requirements, availability of input parameters, ease of use, etc.

The Van Allen Probes or Radiation Belt Storm Probe (RBSP) mission ended in 2019 and there is no dedicated follow-on mission to the equatorial radiation belts planned in the near future. The Polar Operational Environmental Satellite (POES) program, which provides observations of the precipitating radiation belt electrons, may end in the next several years and there is no current plan to replace those assets. Moreover, as discussed later, NN models that input the past values of the output parameters tend not to be able to respond accurately and timely to sudden changes in the solar wind drivers, e.g., sudden arrivals of density/pressure pulses or coronal mass ejections (CMEs) (e.g., *Wing et al.*, 2005).

The present study develops an empirical model of radiation belt electron PSD using an information-theory informed NN as the core of the model (*Johnson and Wing*, 2018). From the consideration of the versatility of running the model in real time and the aforementioned challenges, our model inputs only solar wind and magnetospheric state parameters (proxied by geomagnetic indices) and outputs outer radiation belt electron PSD. The input parameters and their lag times are determined from *Wing et al*. (2021) information theoretic analysis of the solar

117 wind and magnetospheric drivers of PSD.

118

119 **2. Data set**

120 The NASA's Van Allen Probe (RBSP) mission, which was launched in 2012, consisted of
121 two identically instrumented spacecraft in near-equatorial orbit (about 10° inclination) with
122 perigee at 600 km altitude and apogee at 5.8 R_E geocentric (*Mauk et al.*, 2013). The MAGnetic
123 Electron Ion Spectrometer (MagEIS) is part of the Energetic particle, Composition, and Thermal
124 plasma Suite (ECT) instrument on board of RBSP (*Spence et al.,*, 2013). MagEIS measured the
125 energy range of 30 keV to 4 MeV for electrons and 20 keV to 1 MeV for ions (*Blake et al*., 2013).

126 Radiation belt electron dynamics can often be well-organized by electron PSD as a function
127 of the three by their adiabatic invariants and PSD (μ, I, L*) where μ = the first adiabatic invariant
128 related to the gyromotion perpendicular to the magnetic field line, I = the second adiabatic
129 invariant related to the bounce motion along the field line (some studies use K instead of I, but
130 they are related) (*Green and Kivelson*, 2004), and L* = the third adiabatic invariant related to the
131 curvature and gradient drift motion around the Earth (actually L* is inversely proportional to the
132 traditional third invariant Φ) (*Roederer*, 1970; *Schulz and Lanzerotti*, 1974).

133 The radiation belt electron PSD from MagEIS is calculated at 1 min resolution using TS04
134 magnetic field model (*Tsyganenko and Sitnov*, 2005) and a method similar to that used in *Turner*
135 *et al*., 2014a; 2014b). We select the electrons with μ = 560–875 MeV G^{-1} and I = 0.088–0.14 R_E
136 $G^{0.5}$. These electrons have an average energy of about 1.3 MeV over L* = 2.9–6.5 and are
137 concentrated near the magnetic equator (i.e., mirroring at low magnetic latitudes); thus, they are
138 representative of the core population of relativistic electrons in Earth's outer radiation belt.

139 The solar wind, AL, and SYM-H data 2013-2018 at 1-min resolution from the OMNI

dataset were used and provided by NASA (http://omniweb.gsfc.nasa.gov/). Both the PSD and OMNI data 2013-2018 are averaged with 30 min sliding window.

We merge each OMNI solar wind parameter (V_{sw}, n_{sw} etc.) with the RBSP electron PSD (data from both RBSP A and B are used). The merged dataset has ~64,500 points distributed from L* = 2.9 to 6.5. However, the distribution is not uniform across L*, as shown in Figure 1.

3. Methodology

It has been increasingly popular to use NN, including deep learning, to develop empirical space weather models, including radiation belt models. However, a novelty with our approach is that we use information theory to assist with the modeling. Figure 2 shows the schematic of the model.

The model inputs solar wind, magnetospheric parameters, and L*; and outputs radiation belt electron PSD. *Wing et al*. (2021) ranked the solar wind and magnetospheric parameters based on the information transfer to the PSD (see Table 1 in *Wing et al*. (2021)). We select the top 8 parameters as the model input parameters, namely solar wind velocity, SYM-H, AL, solar wind dynamic pressure, IMF |B|, IMF Bz, solar wind density, and IMF By (in decreasing order by the amount of information transferred from the parameter to radiation belt electron PSD). The solar wind dynamic pressure usually tracks the solar wind density fairly well and the information content in the dynamic pressure is entirely captured by the solar wind speed and density, so we omit solar wind dynamic pressure. The input parameters and their lag times are listed in Table 1. The model outputs PSD with no time lag with respect to the arrival time of the solar wind at the magnetosphere (nowcast).

The NN architecture used is the standard feedforward–backpropagation network, which is

sometimes referred to as multi-layered perceptrons (MLP). The NN architecture has 5 layers: 1 input layer (531 nodes), 1 output layer (1 node), and 3 hidden layers (each has 800 nodes). The model is developed using python and Tensorflow machine learning package, which is an open source package (*Abadi et al*., 2016).

All the input and output parameters are normalized. The PSD distribution is skewed to the left as shown in Figure 3a. In order to get higher performance, log PSD is used rather than PSD. Log PSD (Figure 3b) reduces the skewness in the original PSD distribution, which would help training the NN. Both RBSP A and B data are split into two sets: (1) training set and (2) test set. The training set consists of data in the time intervals (2013.5–2015.5), (2016–2017), (2017.5–2018.5) while the test set consists of (2013–2013.5), (2015.5–2016), (2017–2017.5), and (2018.5–2019.0). Staggering the training and test sets ensures no systematic temporal bias (e.g., solar cycle dependencies) are present in the resulting model.

4. Results

In order to show the model performance, we select two long events from the test set where there are at least two weeks of continuous solar wind observations, AL and SYM-H records, and RBSP electron PSD observations: (1) 2013 April 27 – May 13 and (2) 2017 Mar 13 – 29. These intervals are selected also because they exhibit a wide range of solar wind driving as well as geomagentic storm and substorm dynamics. Thus, they are intended to show how well the model can perform under average and unusual solar wind and magnetospheric conditions. They are certainly not intended to show the best examples of the model performance.

Figures 4 plots solar wind velocity (a), density (b), SYM-H (c), AL (d), L* and model PSD (e), Δ log PSD = log(observed PSD) – log(model PSD) (f), and observed and model PSD (g) for

186 the first half of the first event, 2013 April 27 – May 5. Panel d shows quasi-periodic substorms
187 (minimum AL > –400 nT) throughout the interval, which is fairly typical (*Borovsky and*
188 *Yakymenko*, 2017). However, an unusual feature of this interval is that there is a sharp density
189 pulse (maximum ~15 cm^{-3}) that is followed by a moderate storm (minimum SYM-H ~ –60 nT)
190 and large substorm (minimum AL ~ –900 nT) on May 1. Panel g shows that there is a drop in
191 PSD on May 1, which may be attributed to magnetopause shadowing due to the sharp rise in solar
192 wind density and dynamic pressure (e.g., *Li et al.*, 2001; *Kellerman and Shprits*, 2012; *Turner et*
193 *al*., 2012; *Ukhorskiy et al*., 2006). However, the PSD seems to have recovered by the end of May
194 2. Panels f and g show that the model generally performs reasonably well throughout this interval
195 even in the presence of quasi periodic substorms, but it does not do as well around the
196 density/pressure pulse and the storm and substorm on May 1–2. At high L*, L* > 4, the model
197 PSD appears to track the decrease and then the increase of the observed PSD reasonably well.
198 However, at low L*, L* < 4, the model PSD decreases significantly, by more than an order of
199 magnitude, whereas the observed PSD does not appear to be affected much by the density pulse.
200 Figure 4f shows that most of the time the observed and model PSD are within the same
201 order of magnitude of each other, $|\Delta \log PSD| < 1$ $(c^3\ MeV^{-3}\ cm^{-3})^{-1}$. Large $|\Delta \log PSD|$ generally
202 corresponds to low PSD and low L* that is in the slot region. In order to show this, several dotted
203 vertical red lines are drawn to connect some of the largest $|\Delta \log PSD|$ in Figure 4f to their
204 corresponding PSD in Figure 4g. This trend can be seen throughout Figure 4. When PSD is low,
205 a little discrepancy from the observed value would lead to large $|\Delta \log PSD|$. Low PSD may be
206 less relevant for space weather than high PSD within the outer radiation belt. It should be noted
207 that as shown in Figure 4, most of the time, the error is small, $|\Delta \log PSD| < 1$ $(c^3\ MeV^{-3}\ cm^{-3})^{-1}$,
208 for high and low PSD,

Figure 5 presents the interval 2013 May 05–13, which is the second half of the first event, in the same format as Figure 4. As in Figure 4, panel d shows quasi periodic moderate and small susbstorms (minimum AL > ~ –300 nT) throughout the interval. This interval starts out with a small storm (minimum SYM-H ~ –28 nT) on May 5, and a narrow density pulse (maximum density ~ 19 cm^{-3}) on May 6. There is a brief PSD decrease that occurs at or just before the storm onset on May 5, but the model misses this brief drop in PSD (panel g), resulting in a brief large discrepancy (Δ log PSD < –2 $(c^3\ MeV^{-3}\ cm^{-3})^{-1}$) on panel f. Unlike the density/pressure pulse in Figure 4, the density/pressure pulse on May 6 does not seem to affect the observed PSD that much, but the model responds by decreasing its PSD, particularly at L* < 4, resulting in a brief large discrepancy (Δ log PSD > 1 $(c^3\ MeV^{-3}\ cm^{-3})^{-1}$) on May 6 (panel g). The rest of the interval has no storm, but there are small and moderate substorms (minimum AL > –300 nT). The model performs well ($|\Delta$ log PSD| < 1 $(c^3\ MeV^{-3}\ cm^{-3})^{-1}$) during this interval, except near the end at low L* (L* < 4) where Δ log PSD > 1 $(c^3\ MeV^{-3}\ cm^{-3})^{-1}$. It is not clear what causes the model to underestimate PSD at this time. As in Figure 4, several dotted vertical red lines from some of the largest $|\Delta$ log PSD| are drawn in panels f and g to show that generally large $|\Delta$ log PSD| corresponds to low PSD, but most of the time the error is small for large and small PSD.

Figure 6 presents the interval 2017 Mar 13–21, which is the first half of the second event in the same format as Figures 4 and 5. This interval shows the worst model performance out of the four intervals presented herein and one of the worst intervals seen in the entire test set. As in the previous intervals, there are quasi periodic small and moderate substorms (minimum AL > –350 nT) in panel d. The solar wind velocity fluctuates but is lower than average, < 400 km s^{-1}, throughout the interval. There is a broad density pulse (maximum ~ 23 cm^{-3}) on Mar 15, which is followed by a small storm (minimum SYM-H ~ – 20 nT) and moderate substorm (minimum AL

~ –350 nT) near the beginning of Mar 16. There is no significant change in the observed PSD that can be attributed to these solar wind parameters and magnetospheric activity indices (storm and substorm). However, the increase of solar wind density/pressure followed by substorm injections cause the model PSD to first decrease due to the expected magnetopause shadowing (e.g., *Li et al.*, 2001; *Kellerman and Shprits*, 2012; *Turner et al*., 2012; *Ukhorskiy et al*., 2006; *Wing et al*., 2016; 2021) and then increase due to the expected storm-time acceleration and substorm injections (e.g,, *Baker et al*., 1996; *Tang et al.*, 2017a; *Boyd et al*., 2016; *Wing et al*., 2016; 2021; *Meredith et al*., 2001; *Li et al*., 2009). It is not clear why this expected behavior is not observed in the RBSP PSD. Because the model significantly decreases its PSD while the observed PSD does not significantly change, the model PSD severely underestimates the observed PSD at all L* as seen in panels f and g. As before, several dotted vertical red lines from some of the largest |Δ log PSD| are drawn in panels f and g to show that large |Δ log PSD| fairly consistently corresponds to low PSD.

Figure 7 presents the interval 2017 Mar 21–29, which is the second half of the second event in the same format as Figure 6. The solar wind velocity is higher than average, > 500 km s^{-1}, throughout most of the interval. This interval has two interesting features, one at the beginning and one at the end of the interval. At the beginning of the interval, there is a density pulse (maximum ~ 32 cm^{-3}) which is followed by a large substorm (minimum AL ~ –750), but there is no indication of a corresponding geomagnetic storm. In response to the density/pressure increase, both the observed and model PSDs first decrease and then increase on Mar 21–22. However, the model PSD decreases more than the observed PSD, resulting in a large discrepancy with Δ log PSD > 2 $(c^3\ MeV^{-3}\ cm^{-3})^{-1}$. However, the model PSD increases quickly such that by the end of Mar 21, it has more or less caught up with the observed PSD. Thereafter, the model PSD tracks the observed PSD fairly well as they are both recovering from the electron loss due to the

magnetopause shadowing. The PSD completely recovers by the middle of the day on Mar 22 and thereafter, the model PSD generally performs well (Δ log PSD < 1 (c^3 MeV^{-3} cm^{-3})$^{-1}$) as shown in panels f and g. As before, several dotted vertical red lines from some of the largest |Δ log PSD| are drawn to show that large |Δ log PSD| fairly consistently corresponds to low PSD.

At the end of the interval, there is another density pulse (maximum ~22 cm^{-3}) that is followed by a large or moderate storm (minimum SYM-H ~ – 80nT) and three large substorms (two with minimum AL ~ –1000 nT one with minimum AL ~ –750 nT) on Mar 27. In response, the observed PSD decreases soon after the density/pressure pulse in the first half of Mar 27 and then increases. The observed PSD completely recovers by the middle of the day on Mar 28. The model PSD tracks the observed PSD fairly well during this highly disturbed period (Δ log PSD < 1 (c^3 MeV^{-3} cm^{-3})$^{-1}$) as shown in panels f and g.

Figures 4–7 show that the model performs well and the error is small for large and small PSD. There are instances when the error is large, |Δ log PSD| > 1 (c^3 MeV^{-3} cm^{-3})$^{-1}$, but these points are usually associated with low PSD.

The model performance has also been evaluated statistically. There are 23,853 number of points in the test set. Based on the evaluation of model PSD for the entire test set: root mean square (rmse) = 3.1×10^{-6} c^3 MeV^{-3} cm^{-3}; the mean absolute percent error (mape) = 115%; the median absolute percent error = 57%; and the prediction efficiency (PE) = 0.62. PE is defined as $PE = 1 - \frac{\sum_1^n (o_i - m_i)^2}{\sum_1^n (o_i - <o>)^2}$ where o = observed PSD, m = model PSD, <o> = mean observed PSD. PE = 1 indicates the model PSD exactly matches the observed PSD while PE = 0 indicates the model simply outputs the mean value. PE < 0 indicates the model output is worse than simply outputting the mean for each point in the test set.

The model performance has a dependence on L*. The data are binned from L* = 3 to 6.5

into 7 bins with each bin having 0.5. Figure 8a plots the PE as a function of L*, which ranges from from –0.043 for L* = 3 to 0.76 for L* = 6.5. Figure 8b shows the histogram of the number of points in each bin. The L* = 6–6.5 bin has the fewest points, n = 227 and hence the PE for this bin may be less accurate than those for other L* bins. The PE for the entire test set (0.62) is close to that obtained for L* = 4.5–5.5 because this L* range has the most data points as shown in Figure 8b.

The model PSD accuracy generally increases with increasing distance from the Earth (increasing L*). The model PE for L* = 3–4 is nearly 0 because the solar wind and magnetospheric drivers have less influence on the PSD at this location that at L* > 4. Indeed, *Wing et al*. (2021) showed that the solar wind density transfers information to PSD only at L* > 4.5. Solar wind velocity and AL transfer information to PSD at L* > 4 and only small amount of information at L* = 3.5–4. Out of all the parameters that are inputted to the model, only SYM-H transfers information to PSD all the way to L* = 3, but the amount of information transfer at L* = 3–3.5 is small. Conversely, the input parameters (solar wind parameters, SYM-H, and AL) provide significant information about PSD at L* > 4 (*Wing et al*., 2021) and consequently, the model performance improves at this L* range.

The model PE is similar to that obtained by DREAM (*Reeves et al*., 2012) at L* > 4.5 and slightly better than that obtained by DREAM at L* < 4.5. As with DREAM, our model performs better than AE8min (*Vette*, 1991) and CRRESELE (*Brautigam and Bell*, 1995) models. For many years, AE8 series model was considered standard for engineering applications. (AE8min model is superseded by a newer model, AE9, (*Ginet et al*., 2013), but like AE8, AE9 is a statistical model that is not relevant to individual event-based prediction).

We have also compared our model PE with that of PreMevE 2.0, which inputs solar wind

velocity, POES and Los Alamos National Laboratory (LANL) geosynchronous satellite observations of MeV electrons at LEO and GEO, respectively, (*Pires de Lima et al*., 2020). The comparison is inexact because PreMevE 2.0 uses 5-hour time resolution, and forecasts 100 keV – 2MeV electron fluxes one day ahead. If these differences can be ignored, PreMevE 2.0 performs better than our model at L = 2.8–4.5 (PE = 0.6–0.8), but not as well at L = 4.5–6 (PE = 0.4–0.6). Their high PE at L < 4.5 can be attributed to the model inputting POES data. As noted by the authors, PreMeVE 2.0 forecasted values often lag behind the observations when the fluxes suddenly jump in response to the sudden change in the solar wind drivers (*Pires de Lima et al*., 2020), presumably because the NN assigns more weight to the POES electron fluxes than to the solar wind velocity as discussed in the next Section.

5. Discussion and conclusion

The radiation belt electron PSD has dependences on the solar wind drivers and the state of the magnetosphere. The PSD also has a strong dependence on its past values because the magnetospheric dynamics can often be characterized, to a large extent, as being persistent. Because of this magnetospheric persistence characteristic, knowledge of the previous values of PSD (or J_e), either directly from in situ satellites or inferred from the precipitating electrons, would immensely help NN learn more easily and reduce the error of the output PSD (or J_e) significantly (e.g., *Pires de Lima*, 2020; *Ling et al*., 2010). However, a common problem for supervised learning NN models is that during the learning phase, the models would learn quickly that they would do very well if they assigned a lot of weight on the previous values and far less weight on the solar wind input parameters. As a result, the model output would, to some extent, mimic the input value with some time lag and would not be able to respond correctly and timely to sudden changes in

the solar wind drivers, e.g., sudden arrival of CMEs or density/pressure pulses. This persistence behavior is widely seen not just in the radiation belt models, but also in other magnetospheric models that input past values of the predicted parameters (e.g., *Wing et al*., 2005; *Pires de Lima*, 2020).

The present study develops an empirical radiation belt model that inputs solar wind parameters, the magnetospheric state parameters as proxied by AL and SYM-H, and L* (i.e., location in the radiation belts). The model outputs radiation belt electron PSD at a particular set of adiabatic invariant coordinates (μ = 560–875 MeV G^{-1} and I = 0.088–0.14 R_E $G^{0.5}$, and user-input L*). It is, of course, more challenging to model PSD without having its past values as a reference. On the other hand, the model PSD does not exhibit the undesired persistence behavior where the output PSD would simply mimic the observed PSD with a time lag. Also, this new model can operate independent of input data from any radiation belt observatories, whether they be in the near-equatorial plane (e.g., Van Allen Probes) or at LEO (e.g., POES). This renders the model robust for operational space weather purposes.

The study demonstrates how information theory can be used to assist empirical modeling of the radiation belt electron variability. Information theory is used to select the solar wind parameters and magnetospheric indices (proxy for the magnetospheric state) and their optimal lag times. The rather large number of past values, up to 72 hours, used in some input parameters (see Table 1) are justified because the results from information theory analysis reveals long range linear and nonlinear causal relationship between these parameters and PSD (*Wing et al*., 2021). Information theory analysis also helps explain the model performance such as increasing PE with increasing L* as discussed in Section 4. Recently, there has been increasing amount of efforts put into developing "explainable" models, which stems from the desire to build more confidence on

347 the usage of black box models such as neural networks. The fact that all the input parameters and
348 their lag times have been shown to transfer information to PSD (instead of choosing input
349 parameters in an ad hoc manner) and the model performance falls within the expected behavior of
350 information theory analysis, should help build confidence in our model.

351 Moreover, we have used one of the simplest neural network architecture, namely feed
352 forward-backpropagation or MLP architecture. Although the neural network dimension is wide
353 and deep, the simple architecture allows for relatively quick training and development time (the
354 model was developed on a laptop computer). However, despite the simple architecture, the model
355 appears to perform well. Using PE as a metric, the model performs as well as or slightly better
356 than DREAM (*Reeves et al*., 2012) and performs better than AE8min (*Vette*, 1991) and
357 CRRESELE (*Brautigam and Bell*, 1995) models. Moreover, in our model, the error is generally
358 small, $|\Delta \log \mathrm{PSD}| < 1$ $(c^3\ \mathrm{MeV}^{-3}\ \mathrm{cm}^{-3})^{-1}$. There are instances when the error is large, but these
359 points are usually associated with low-PSD slot region, which is expected considering the very
360 high and sharp gradient in PSD at the boundary between the outer belt and the slot. Also, low PSD
361 may have smaller space weather impacts. The good performance can be attributed, at least partly,
362 to the usage of information theory, which guides the selection of the input parameters and their lag
363 times.

364 Interestingly, just like our model, the DREAM model PE increases with increasing L* but
365 for a different reason. DREAM performs better at higher L* because the model was developed
366 using data at $L^* > 4.2$ (*Reeves et al*., 2012) whereas our model performs better at higher L* because
367 solar wind and magnetospheric indices (SYM-H, AL) transfer more information to higher L* than
368 lower L*. This behavior can be contrasted to a class of empirical models that input precipitating
369 radiation belt electrons observed at LEO. For example, the PEs for PreMevE (*Chen et al*., 2019)

and PrevMevE 2.0 (*Pires de Lima et al*., 2020) generally decrease with increasing L because the models input POES data. PreMevE inputs only observations from POES at LEO and LANL at GEO (*Chen et al*., 2019). The lower performance with increasing L is also seen in another model, SHELLS, which inputs POES data (and Kp) (*Claudepierre and O'Brien*, 2020). They suggested that this behavior can be explained by (1) pitch angle scattering rate, which is proportional to |B|, decreases with increasing L; (2) rate of radial diffusion increases with L; and (3) low to high altitude mapping accuracy decreases with increasing L due to deviation from dipolar field. Thus, it can be seen that based on the performance as a function of L or L*, our model can complement a class of empirical models that input POES data or in general, LEO satellite data.

For operational consideration, the model can input solar wind observations that are routinely available from the solar wind monitor at L1 and forecast PSD 30–60 min ahead. The input AL can be obtained from an AL forecast/nowcast model that is driven entirely by solar wind (e.g., *Luo et al*., 2013; Li et al., 2007; *Weigel et al*., 1999; *Amariutei et al*., 2012). Likewise, the input SYM-H can be obtained from a SYM-H or Dst forecast/nowcast model that is driven entirely by the solar wind (e.g., *Temerin and Li*, 2006; *Cai et al*., 2009; *Bhaskar and Vichare*, 2019; *Chandorkar et al*., 2017; Siciliano et al., 2021). The *Luo et al*. (2013) AL and *Temerin and Li* (2006) Dst forecasts are routinely made available at the University of Colorado website http://lasp.colorado.edu/space_weather/dsttemerin/dsttemerin.html.

The present model, which uses simple neural network architecture, is intended to serve as a baseline model. To follow up on the present study, we plan to use a more sophisticated neural network architecture, long short term memory (LSTM), which was designed to work with time series data, and hence holds promises for better performance.

Acknowledgments. The solar wind, SYM-H, and AL dataset were obtained from NASA OMNIweb https://omniweb.gsfc.nasa.gov/. The RBSP MagEIS Level 4 data can be obtained from https://spdf.gsfc.nasa.gov/pub/data/rbsp/ and the PSD data can be obtained from https://rbspgway.jhuapl.edu/psd. Simon Wing acknowledges support of NASA Van Allen Probe Contract NNN16AA09T and NASA Grants NNX16AQ87G, 80NSSC20K0704, 80NSSC19K0843, 80NSSC19K0822, 80NSSC20K0188, 80NSSC20K1279, and 80NSSC20K1271. This work has benefitted from discussions within the International Space Science Institute (ISSI) Team # 455 "Complex Systems Perspectives Pertaining to the Research of the Near-Earth Electromagnetic Environment."

References

Abadi, M., A. Agarwal, P. Barham et al. (2016), TensorFlow: Large-Scale Machine Learning on Heterogeneous Distributed Systems, Technical Report, arXiv:1603.04467

Alves, L.R., Souza, V.M., Jauer, P.R. *et al.* The Role of Solar Wind Structures in the Generation of ULF Waves in the Inner Magnetosphere. *Sol Phys* **292,** 92 (2017). https://doi.org/10.1007/s11207-017-1113-4

Amariutei, O. A. and Ganushkina, N. Yu.: On the prediction of the auroral westward electrojet index, Ann. Geophys., 30, 841–847, https://doi.org/10.5194/angeo-30-841-2012, 2012

Baker, D. N., R. L. McPherron, T. E. Cayton, and R. W. Klebesadel (1990), Linear prediction filter analysis of relativistic electron properties at 6.6 R_E , J. Geophys. Res., 95(A9),15133–15140, doi:10.1029/JA095iA09p15133.

Baker, D. N., Pulkkinen, T. I., Angelopoulos, V., Baumjohann, W., and McPherron, R. L. (1996), Neutral line model of substorms: Past results and present view, *J. Geophys. Res.*, 101(A6), 12975– 13010, doi:10.1029/95JA03753.

Baker, D.N., Erickson, P.J., Fennell, J.F. *et al.* Space Weather Effects in the Earth's Radiation Belts. *Space Sci Rev* **214,** 17 (2018). https://doi.org/10.1007/s11214-017-0452-7

Baker, D. N., Hoxie, V., Zhao, H., Jaynes, A. N., Kanekal, S., Li, X., & Elkington, S. (2019). Multiyear measurements of radiation belt electrons: Acceleration, transport, and loss. *Journal of Geophysical Research: Space Physics*, 124, 2588– 2602. https://doi.org/10.1029/2018JA026259

425 Balikhin, M. A., R. J. Boynton, S. N. Walker, J. E. Borovsky, S. A. Billings, and H. L.
426 Wei(2011), Using the NARMAX approach to model the evolution of energetic electrons
427 fluxes at geostationary orbit, Geophys. Res. Lett., 38, L18105, doi:10.1029/2011GL048980.
428 Balikhin, M. A., Rodriguez, J. V., Boynton, R. J., Walker, S. N., Aryan, H., Sibeck, D. G.,
429 and Billings, S. A. (2016), Comparative analysis of NOAA REFM and SNB^{3}GEO tools for
430 the forecast of the fluxes of high-energy electrons at GEO, *Space Weather*, 14, 22– 31,
431 doi:10.1002/2015SW001303
432 Bhaskar, Ankush, and Geeta Vichare (2019), Forecasting of SYMH and ASYH indices for
433 geomagnetic storms of solar cycle 24 including St. Patrick's day, 2015 storm using NARX
434 neural network, J. Space Weather Space Clim., 9, A12, DOI: 10.1051/swsc/2019007
435 Blake, J.B., Carranza, P.A., Claudepierre, S.G. *et al.* (2013), The *Magnetic Electron Ion*
436 *Spectrometer* (MagEIS) Instruments Aboard the Radiation Belt Storm Probes (RBSP)
437 Spacecraft. *Space Sci Rev* **179,** 383–421, https://doi.org/10.1007/s11214-013-9991-8
438 Boberg, F., P. Wintoft, and H. Lundstedt (2000), Real time Kp prediction from solar wind data
439 using neural networks, Phys. Chem. Earth, 25, 275-280.
440 Borovsky, J. E., and Denton, M. H. (2014), Exploring the cross correlations and autocorrelations
441 of the ULF indices and incorporating the ULF indices into the systems science of the solar
442 wind-driven magnetosphere, *J. Geophys. Res. Space Physics*, 119, 4307– 4334,
443 doi:10.1002/2014JA019876.
444 Borovsky, J. E., and Yakymenko, K. (2017), Substorm occurrence rates, substorm recurrence
445 times, and solar wind structure, *J. Geophys. Res. Space Physics*, 122, 2973– 2998,
446 doi:10.1002/2016JA023625.

Borovsky, J. E. (2017). Time-integral correlations of multiple variables with the relativistic-electron flux at geosynchronous orbit: The strong roles of substorm-injected electrons and the ion plasma sheet. *Journal of Geophysical Research: Space Physics*, 122, 11,961– 11,990. https://doi.org/10.1002/2017JA024476

Borovsky, J. E. (2018), On the origins of the intercorrelations between solar wind variables. *Journal of Geophysical Research: Space Physics*, 123, 20– 29. https://doi.org/10.1002/2017JA024650

Borovsky, J. E. (2020), What magnetospheric and ionospheric researchers should know about the solar wind, *J. Atmos. Sol. Phys*., 204, 105271, https://doi.org/10.1016/j.jastp.2020.105271.

Boyd, A. J., Spence, H. E., Huang, C.-L., Reeves, G. D., Baker, D. N., Turner, D. L., Claudepierre, S. G., Fennell, J. F., Blake, J. B., and Shprits, Y. Y. (2016), Statistical properties of the radiation belt seed population, *J. Geophys. Res. Space Physics*, 121, 7636– 7646, doi:10.1002/2016JA022652.

Brautigam, D. H., and J. T. Bell (1995), CRRESELE documentation, Rep. PL-TR-95-2128, Phillips Lab., Hanscom AFB, Mass.

Cai, L., Ma, S., Cai, H. *et al.* (2009), Prediction of SYM-H index by NARX neural network from IMF and solar wind data. *Sci. China Ser. E-Technol. Sci.* **52,** 2877–2885, https://doi.org/10.1007/s11431-009-0296-9

Chandorkar, M., Camporeale, E., and Wing, S. (2017), Probabilistic forecasting of the disturbance storm time index: An autoregressive Gaussian process approach, *Space Weather*, 15, 1004– 1019, doi:10.1002/2017SW001627.

Chen, Y., Reeves, G. D., Fu, X., & Henderson, M. (2019). PreMevE: New predictive model for megaelectron-volt electrons inside Earth's outer radiation belt. *Space Weather*, 17, 438– 454. https://doi.org/10.1029/2018SW002095

Claudepierre S. G., & O'Brien, T. P. (2020). Specifying high-altitude electrons using low-altitude LEO systems: The SHELLS model. *Space Weather*, 18, e2019SW002402. https://doi.org/10.1029/2019SW002402

Coleman, T., McCollough, J. P., Young, S., & Rigler, E. J. (2018). Operational nowcasting of electron flux levels in the outer zone of Earth's radiation belt. *Space*

Davis, T. N., and Sugiura, M. (1966), Auroral electrojet activity index *AE* and its universal time variations, *J. Geophys. Res.*, 71(3), 785– 801, doi:10.1029/JZ071i003p00785.

Dessler, A., and E. Parker (1959), Hydromagnetic theory of geomagnetic storms, *J. Geophys. Res.*, **64**(12), 2239–2252, doi:10.1029/JZ064i012p02239.

Ginet, G.P., O'Brien, T.P., Huston, S.L. *et al.* (2013), AE9, AP9 and SPM: New Models for Specifying the Trapped Energetic Particle and Space Plasma Environment. *Space Sci Rev* **179,** 579–615, https://doi.org/10.1007/s11214-013-9964-y

Green, J. C., and M. G. Kivelson (2004), Relativistic electrons in the outer radiation belt: Differentiating between acceleration mechanisms, J. Geophys. Res., 109, A03213, doi:10.1029/2003JA010153.

Horne, R. B., Glauert, S. A., Meredith, N. P., Boscher, D., Maget, V., Heynderickx, D., and Pitchford, D. (2013), Space weather impacts on satellites and forecasting the Earth's electron radiation belts with SPACECAST, *Space Weather*, 11, 169– 186, doi:10.1002/swe.20023.

Iyemori, T. (1990), Storm-time magnetospheric currents inferred from mid-latitude geomagnetic field variations, J. Geomag. Geoelectr., 42, 1249–1265.

Johnson, J. R., & Wing, S. (2018). An information-theoretical approach to space weather. In Machine learning techniques for space weather (pp. 45–69): Elsevier, ISBN:978-0-12-811788-0.

Kellerman, A. C., and Y. Y. Shprits (2012), On the influence of solar wind conditions on the outer-electron radiation belt, J. Geophys. Res., 117, A05217, doi:10.1029/2011JA017253.

Kellerman, A. C., Y. Y. Shprits, and D. L. Turner (2013), A Geosynchronous Radiation-belt Electron Empirical Prediction (GREEP) model, SpaceWeather, 11, doi:10.1002/swe.20074.

Koons, H. C., and Gorney, D. J. (1991), A neural network model of the relativistic electron flux at geosynchronous orbit, *J. Geophys. Res.*, 96(A4), 5549– 5556, doi:10.1029/90JA02380.

Li, W., Thorne, R. M., Angelopoulos, V., Bonnell, J. W., McFadden, J. P., Carlson, C. W., LeContel, O., Roux, A., Glassmeier, K. H., and Auster, H. U. (2009), Evaluation of whistler-mode chorus intensification on the nightside during an injection event observed on the THEMIS spacecraft, *J. Geophys. Res.*, 114, A00C14, doi:10.1029/2008JA013554.

Li, X., Temerin, M., Baker, D. N., Reeves, G. D., & Larson, D. (2001). Quantitative prediction of radiation belt electrons at geostationary orbit based on solar wind measurements. *Geophysical Research Letters*, **28**(9), 1887– 1890. https://doi.org/10.1029/2000GL012681

Li, X., D. N. Baker, M. Temerin, G. Reeves, R. Friedel, and C. Shen (2005), Energetic electrons, 50 keV to 6 MeV, at geosynchronous orbit: Their responses to solar wind variations, Space Weather, 3, S04001, doi:10.1029/2004SW000105.

512 Li, X., K. S. Oh, and M. Temerin (2007), Prediction of the AL index using solar wind parameters,
513 J. Geophys. Res., 112, A06224, doi:10.1029/2006JA011918.
514 Ling, A. G., Ginet, G. P., Hilmer, R. V., and Perry, K. L. (2010), A neural network–based
515 geosynchronous relativistic electron flux forecasting model, *Space Weather*, 8, S09003,
516 doi:10.1029/2010SW000576.
517 Luo, B., Li, X., Temerin, M., and Liu, S. (2013), Prediction of the *AU*, *AL*, and *AE* indices using
518 solar wind parameters, *J. Geophys. Res. Space Physics*, 118, 7683– 7694,
519 doi:10.1002/2013JA019188.
520 Lyatsky, W., and G. V. Khazanov (2008a), Effect of solar wind density on relativistic electrons at
521 geosynchronous orbit, Geophys. Res. Lett., 35, L03109, doi:10.1029/2007GL032524.
522 Lyatsky, W., and G. V. Khazanov (2008b), Effect of geomagnetic disturbances and solar wind
523 density on relativistic electrons at geostationary orbit, J. Geophys. Res., 113, A08224,
524 doi:10.1029/2008JA013048.
525 Maggiolo, R., Hamrin, M., De Keyser, J., Pitkänen, T., Cessateur, G., Gunell, H., & Maes, L.
526 (2017). The delayed time response of geomagnetic activity to the solar wind. Journal of
527 Geophysical Research: Space Physics, 122, 11,109– 11,127.
528 https://doi.org/10.1002/2016JA023793
529 Mauk, B. H., N. J. Fox, S. G. Kanekal, R. L. Kessel, D. G. Sibeck, and A. Ukhorskiy (2013),
530 Science objectives and rationale for the radiation belt storm probes mission, Space Science
531 Review, *179*(1-4), 3–27, doi:10.1007/s11214-012-9908-y.
532 Meredith, N. P., Horne, R. B., and Anderson, R. R. (2001), Substorm dependence of chorus
533 amplitudes: Implications for the acceleration of electrons to relativistic energies, *J. Geophys.*
534 *Res.*, 106(A7), 13165– 13178, doi:10.1029/2000JA900156.

535 Newell, P. T., S. Wing, C. I. Meng, and V. Sigillito (1990), A neural network based system for
536 monitoring the aurora, Johns Hopkins APL Tech. Dig., 11 (3 and 4), 291-299.
537 Newell, P. T., Wing, S., Meng, C.-I., and Sigillito, V. (1991), The auroral oval position, structure,
538 and intensity of precipitation from 1984 onward: An automated on-line data base, *J.*
539 *Geophys. Res.*, 96(A4), 5877– 5882, doi:10.1029/90JA02450.
540 Perry, K. L., G. P. Ginet, A. G. Ling, and R. V. Hilmer (2010), Comparing geosynchronous
541 relativistic electron prediction models, Space Weather, 8, S12002,
542 doi:10.1029/2010SW000581.
543 Paulikas, G. A., and J. B. Blake (1979), Effects of the solar wind on magnetospheric dynamics:
544 Energetic electrons at the synchronous orbit, in *Quantitative Modeling of Magnetospheric*
545 *Processes*, *Geophys. Monogr. Ser.*, Vol 21, pp. 180-202, AGU, Washington D.C.
546 Pinto, V. A., Kim, H.-J., Lyons, L. R., & Bortnik, J. (2018). Interplanetary parameters leading to
547 relativistic electron enhancement and persistent depletion events at geosynchronous orbit
548 and potential for prediction. *Journal of Geophysical Research: Space*
549 *Physics*, 123, 1134– 1145. https://doi.org/10.1002/2017JA024902
550 Pires de Lima, R., Chen, Y., & Lin, Y. (2020). Forecasting megaelectron-volt electrons inside
551 Earth's outer radiation belt: PreMevE 2.0 based on supervised machine learning
552 algorithms. *Space Weather*, 18, e2019SW002399. https://doi.org/10.1029/2019SW002399
553 Reeves, G. D. (1998), Relativistic electrons and magnetic storms: 1992–1995, Geophys. Res. Lett.,
554 25, 1817–1820, doi:10.1029/98GL01398.
555 Reeves, G. D. (2007), Radiation Belt Storm Probes: A New Mission for Space Weather
556 Forecasting. Space Weather, 5: n/a. doi:10.1029/2007SW000341
557 Reeves, G. D., S. K. Morley, R. H. W. Friedel, M. G. Henderson, T. E. Cayton, G. Cunningham, J.

B. Blake, R. A. Christensen, and D. Thomsen (2011), On the relationship between relativistic electron flux and solar wind velocity: Paulikas and Blake revisited, J. Geophys. Res., 116, A02213, doi:10.1029/2010JA015735.

Reeves, G. D., Chen, Y., Cunningham, G. S., Friedel, R. W. H., Henderson, M. G., Jordanova, V. K., Koller, J., Morley, S. K., Thomsen, M. F., and Zaharia, S. (2012), Dynamic Radiation Environment Assimilation Model: DREAM, *Space Weather*, 10, S03006, doi:10.1029/2011SW000729

Reeves, G., S. Morley, and G. Cunningham (2013), Long-term variations in solar wind velocity and radiation belt electrons, J. Geophys. Res. Space Physics, 118, 1040–1048, doi:10.1002/jgra.50126.

Rigler, E. J., M. Wiltberger, and D. N. Baker (2007), Radiation belt electrons respond to multiple solar wind inputs, J. Geophys. Res., 112, A06208, doi:10.1029/2006JA012181

Roederer, J. G. (1970), Dynamics of Geomagnetically Trapped Radiation, Springer, New York, https://doi.org/ 10.1007/978-3-642-49300-3

Rumelhart, D. E., and J. L. McClelland (Eds.) (1987), Parallel Distributed Processing, Vol. I, MIT Press, Cambridge, MA.

Schulz, M., and L.J. Lanzerotti (1974) , Particle Diffusion in the Radiation Belts, Springer, Berlin, 1974, https:// doi.org/10.1007/978-3-642-65675-0

Siciliano, F., Consolini, G., Tozzi, R., Gentili, M., Giannattasio, F., & De Michelis, P. (2021). Forecasting *SYM-H* index: A comparison between long short-term memory and convolutional neural networks. *Space Weather*, 19, e2020SW002589. https://doi.org/10.1029/2020SW002589

Simms, L. E., & Engebretson, M. J. (2020). Classifier neural network models predict relativistic

electron events at geosynchronous orbit better than multiple regression or ARMAX models. *Journal of Geophysical Research: Space Physics*, 125, e2019JA027357. https://doi.org/10.1029/2019JA027357

Shprits, Y. Y., D. Subbotin, and B. Ni (2009), Evolution of electron fluxes in the outer radiation belt computed with the VERB code, J. Geophys. Res., 114, A11209, doi:10.1029/2008JA013784.

Schmidhuber, J. (2015), Deep Learning in Neural Networks: An Overview, *Neural Networks*, **61**, 85–117, arXiv:1404.7828. doi:10.1016/j.neunet.2014.09.003

Smirnov, A. G., Berrendorf, M., Shprits, Y. Y., Kronberg, E. A., Allison, H. J., Aseev, N. A., et al. (2020). Medium energy electron flux in earth's outer radiation belt (MERLIN): A machine learning model. *Space Weather*, 18, e2020SW002532. https://doi.org/10.1029/2020SW002532

Spence, H.E., Reeves, G.D., Baker, D.N. et al. (2013), Science Goals and Overview of the Radiation Belt Storm Probes (RBSP) Energetic Particle, Composition, and Thermal Plasma (ECT) Suite on NASA's Van Allen Probes Mission. Space Sci Rev 179, 311–336, https://doi.org/10.1007/s11214-013-0007-5

Tang, C. L., Wang, Y. X., Ni, B., Zhang, J.-C., Reeves, G. D., Su, Z. P., Baker, D. N., Spence, H. E., Funsten, H. O., and Blake, J. B. (2017a), Radiation belt seed population and its association with the relativistic electron dynamics: A statistical study, *J. Geophys. Res. Space Physics*, 122, 5261– 5276, doi:10.1002/2017JA023905.

Tang, C. L., Wang, Y. X., Ni, B., Su, Z. P., Reeves, G. D., Zhang, J.-C., Baker, D. N., Spence, H. E., Funsten, H. O., and Blake, J. B. (2017b), The effects of magnetospheric processes on relativistic electron dynamics in the Earth's outer radiation belt, *J. Geophys. Res. Space Physics*, 122, 9952– 9968, doi:10.1002/2017JA024407.

Temerin, M., and Li, X. (2006), *Dst* model for 1995–2002, *J. Geophys. Res.*, 111, A04221, doi:10.1029/2005JA011257

Tsyganenko, N. A., and Sitnov, M. I. (2005), Modeling the dynamics of the inner magnetosphere during strong geomagnetic storms, *J. Geophys. Res.*, 110, A03208, doi:10.1029/2004JA010798.

610 Turner, D. L., Y. Shprits, M. Hartinger, and V. Angelopoulos (2012), Explaining sudden losses
611 of outer radiation belt electrons during geomagnetic storms, Nat. Phys., 8, 208–212,
612 doi:10.1038/nphys2185.
613 Turner, D. L., et al. (2014a), On the cause and extent of outer radiation belt losses during the 30
614 September 2012 dropout event, *J. Geophys. Res. Space Physics*, 119, 1530– 1540,
615 doi:10.1002/2013JA019446.
616 Turner, D. L., et al. (2014b), Competing source and loss mechanisms due to wave-particle
617 interactions in Earth's outer radiation belt during the 30 September to 3 October 2012
618 geomagnetic storm, *J. Geophys. Res. Space Physics*, 119, 1960– 1979,
619 doi:10.1002/2014JA019770.
620 Ukhorskiy, A. Y., M. I. Sitnov, A. S. Sharma, B. J. Anderson, S. Ohtani, and A. T. Y. Lui (2004),
621 Data-derived forecasting model for relativistic electron intensity at geosynchronous
622 orbit,Geophys. Res. Lett., 31, L09806, doi:10.1029/2004GL019616.
623 Ukhorskiy, A. Y., B. J. Anderson, P. C. Brandt, and N. A. Tsyganenko (2006), Storm time
624 evolution of the outer radiation belt: Transport and losses, J. Geophys. Res., 111, A11S03,
625 doi:10.1029/2006JA011690.
626 Vette, J. I. (1991), The AE-8 trapped electron model environment, Rep. NSSDC/WDC-A-R&S
627 91–24, NASA Goddard Space Flight Cent., Greenbelt, Md.
628 Wei, H.-L., Billings, S. A., Surjalal Sharma, A., Wing, S., Boynton, R. J., and Walker, S. N. (2011),
629 Forecasting relativistic electron flux using dynamic multiple regression models, Ann.
630 Geophys., 29, 415–420, https://doi.org/10.5194/angeo-29-415-2011.
631 Weigel, R., Horton, W., Tajima, T., & Detman, T. (1999). Forecasting auroral electrojet activity
632 from solar wind input with neural networks, *Geophysical research*

letters, **26**(10), 1353– 1356.

Wing, S., Greenwald, R. A., Meng, C.-I., Sigillito, V. G., and Hutton, L. V. (2003), Neural networks for automated classification of ionospheric irregularities in HF radar backscattered signals, Radio Sci., 38, 1063, doi:10.1029/2003RS002869.

Wing, S., Johnson, J. R., Jen, J., Meng, C.-I., Sibeck, D. G., Bechtold, K., Freeman, J., Costello, K., Balikhin, M., and Takahashi, K. (2005), Kp forecast models, *J. Geophys. Res.*, 110, A04203, doi:10.1029/2004JA010500.

Wing, S., J. R. Johnson, E. Camporeale, and G. D. Reeves (2016), Information theoretical approach to discovering solar wind drivers of the outer radiation belt, J. Geophys. Res. Space Physics, 121, 9378–9399, doi:10.1002/2016JA022711

Wing, S, J. R. Johnson (2019), Applications of Information Theory in Solar and Space Physics, *Entropy*, 21(2):140, https://doi.org/10.3390/e21020140

Wing, S., J. R. Johnson, D. L. Turner, A. Y. Ukhorskiy, and A. J. Boyd (2021), Untangling the solar wind and magnetospheric drivers of the radiation belt electrons, under review, J. Geophys. Res.

Wintoft, P., Wik, M., Matzka, J., and Shprits, Y. (2017). Forecasting Kp from Solar Wind Data: Input Parameter Study Using 3-hour Averages and 3-hour Range Values. *J. Space Weather Space Clim.* 7, A29. doi:10.1051/swsc/2017027

Wu, J., and H. Lundstedt (1997), Geomagnetic storm predictions from solar wind data with the use of dynamic neural networks, J. Geophys. Res., 102, 14,255-14,268.

Xiang, Z., Tu, W., Li, X., Ni, B., Morley, S. K., & Baker, D. N. (2017). Understanding the mechanisms of radiation belt dropouts observed by Van Allen Probes. *Journal of Geophysical Research: Space*

Physics, 122, 9858– 9879. https://doi.org/10.1002/2017JA024487

Zhao, H., Baker, D. N., Jaynes, A. N., Li, X., Elkington, S. R., Kanekal, S. G., Spence, H. E., Boyd, A. J., Huang, C.-L., and Forsyth, C. (2017), On the relation between radiation belt electrons and solar wind parameters/geomagnetic indices: Dependence on the first adiabatic invariant and L^*, *J. Geophys. Res. Space Physics*, 122, 1624– 1642, doi:10.1002/2016JA023658.

Input and output parameters of the model

	Input parameters	Output parameter
1	Vsw(t) to Vsw(t–72 hr)	PSD (t)
2	nsw(t) to nsw(t–12 hr)	
3	IMF |B(t)| to |B(t–10 hr)|	
4	IMF Bz(t) to Bz(t–10 hr)	
5	IMF By(t) to By(t–10 hr)	
6	SYM-H(t) to SYM-H(t–72 hr)	
7	AL(t) to AL(t–72 hr)	

Table 1. Input and output parameters of the model. Vsw = solar wind velocity. nsw = solar wind density. IMF (By, Bz) = GSM y and z component of the interplanetary magnetic field, respectively.

669

670

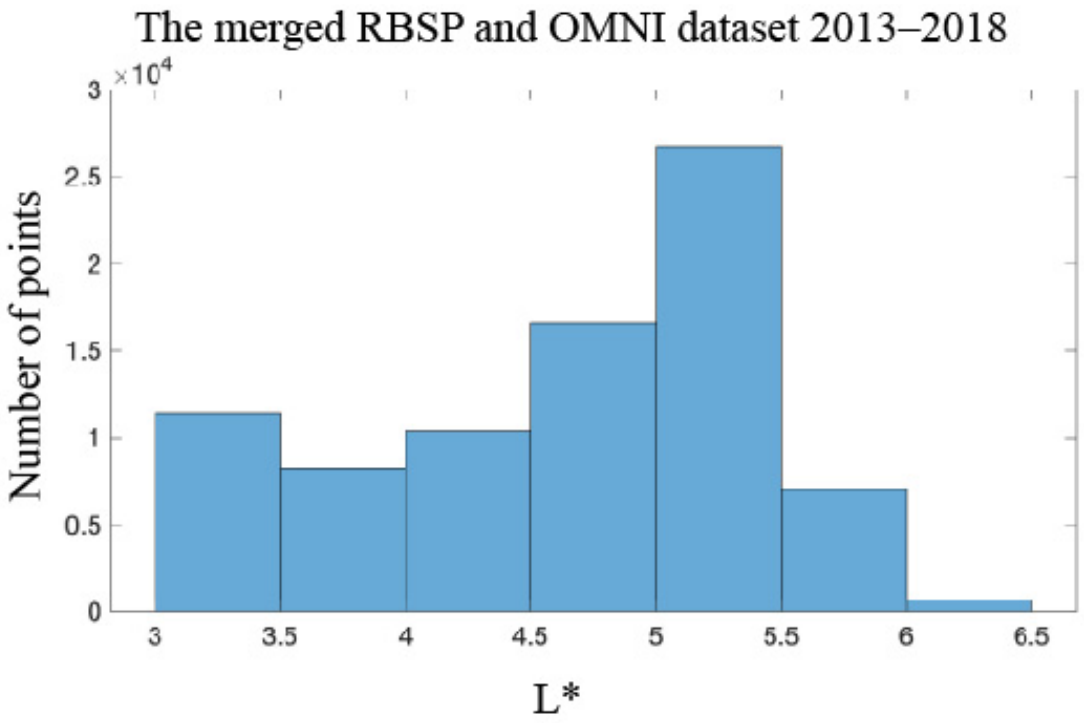

671

672 Figure 1. The distribution of the merged RBSP and OMNI dataset 2013–2018.

673

674

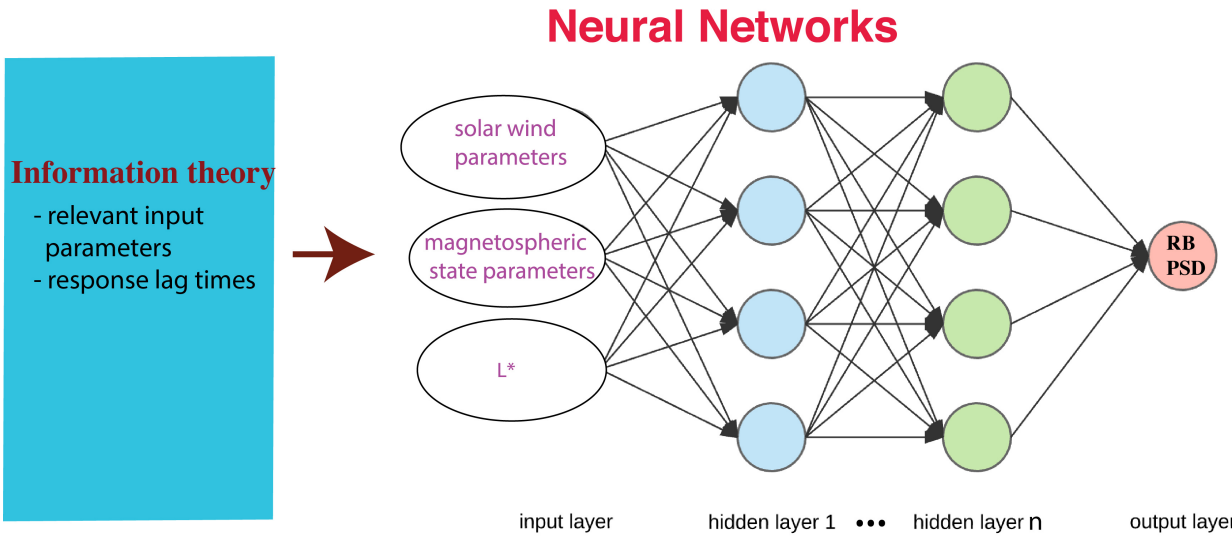

Figure 2. Schematic of the model that combines information theory and neural network. The neural network inputs the solar wind and magnetospheric parameters and L*; and outputs PSD (see Table 1). Information theory is used to select and rank solar wind and magnetospheric parameters and their lag times based on information transfer to radiation belt electron PSD. The model operates at L* range from 3 to 6.5.

686

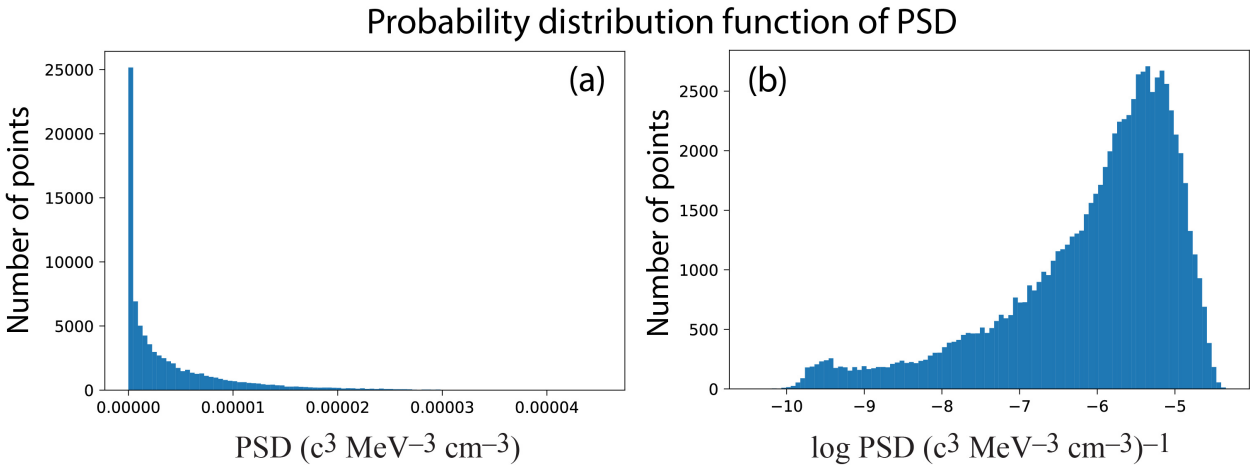

687

688 Figure 3. The distribution of PSD (a) and log PSD (b).
689

690

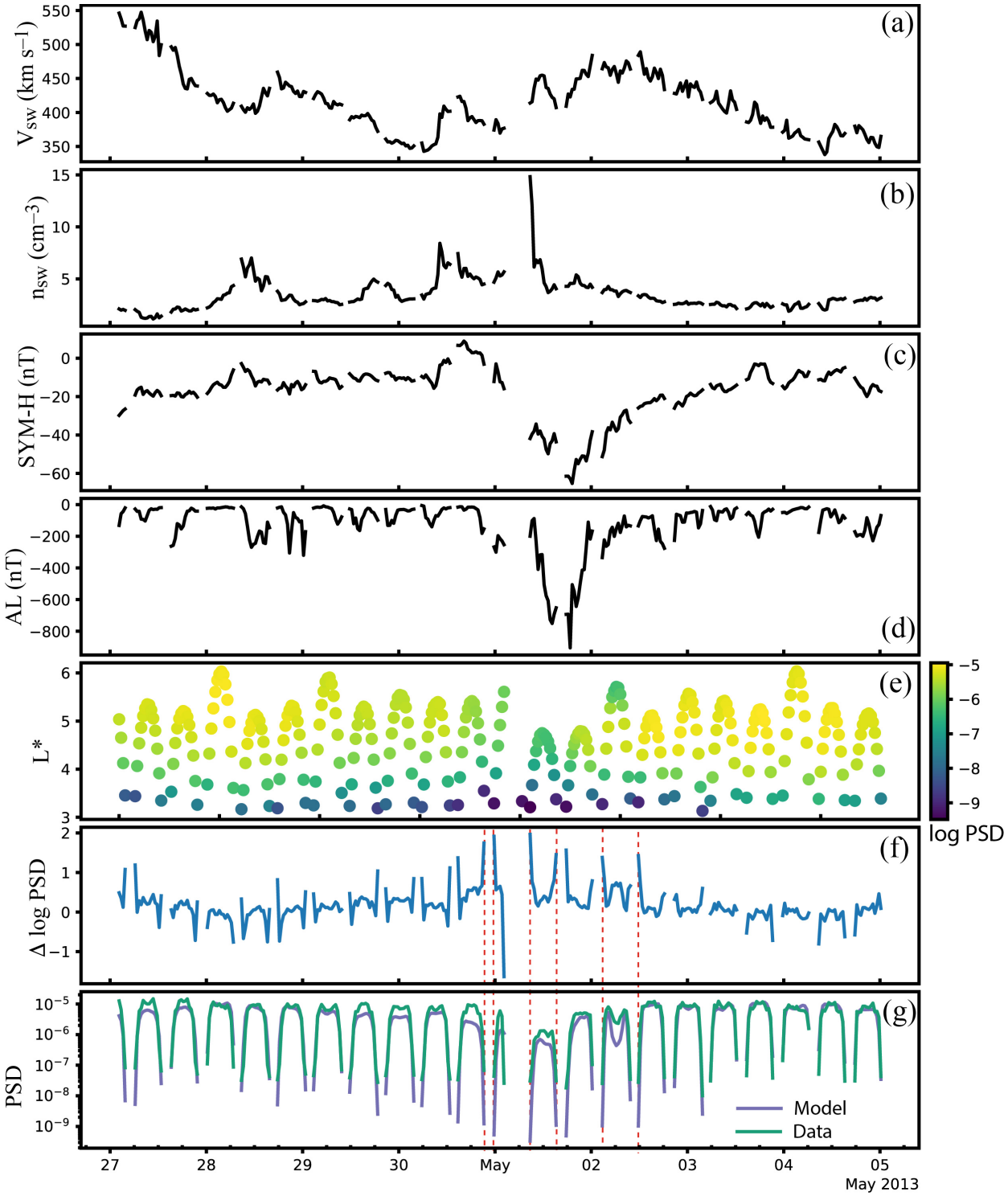

691

692 Figure 4. Solar wind velocity (a), solar wind density (b), SYM-H (c), AL (d), L* and log model
693 PSD (e), Δ log PSD = log(observed PSD) – log(model PSD) (f), and observed (green curve) and
694 model PSD (blue curve) (g) for 2013 April 27 – May 5, which is the first half of the first event.
695 The unit for PSD and ΔPSD is (c^3 MeV^{-3} cm^{-3}). In panels f and g, dotted vertical red lines are
696 drawn to show that generally large |Δ log PSD| can be associated with low PSD.

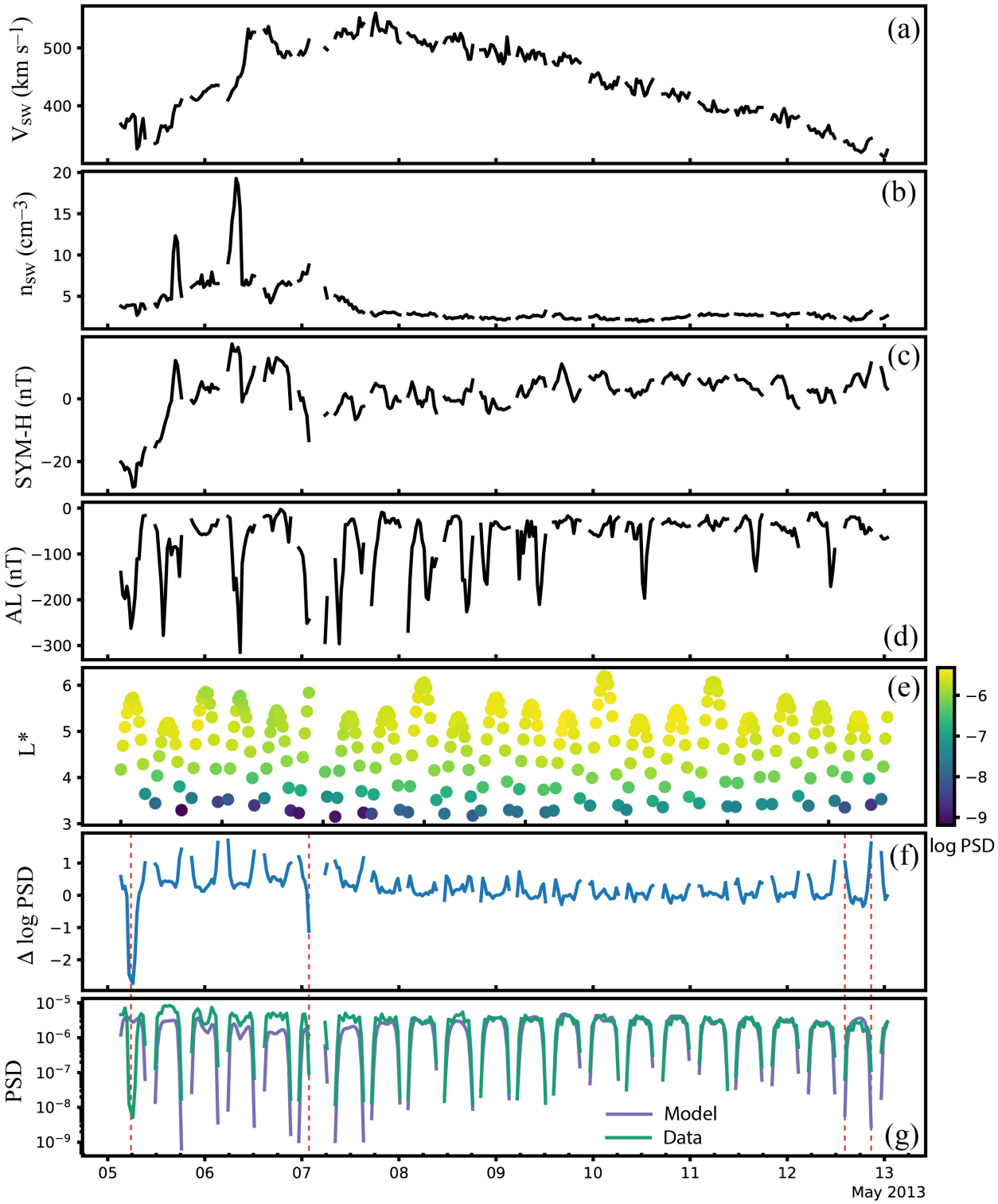

Figure 5. Solar wind velocity (a), solar wind density (b), SYM-H (c), AL (d), L* and log model PSD (e), Δ log PSD = log(observed PSD) – log(model PSD) (f), and observed (green curve) and model PSD (blue curve) (g) for 2013 May 5 – 13, which is the second half of the first event. The unit for PSD and ΔPSD is (c^3 MeV^{-3} cm^{-3}). In panels f and g, dotted vertical red lines are drawn to show that generally large |Δ log PSD| can be associated with low PSD.

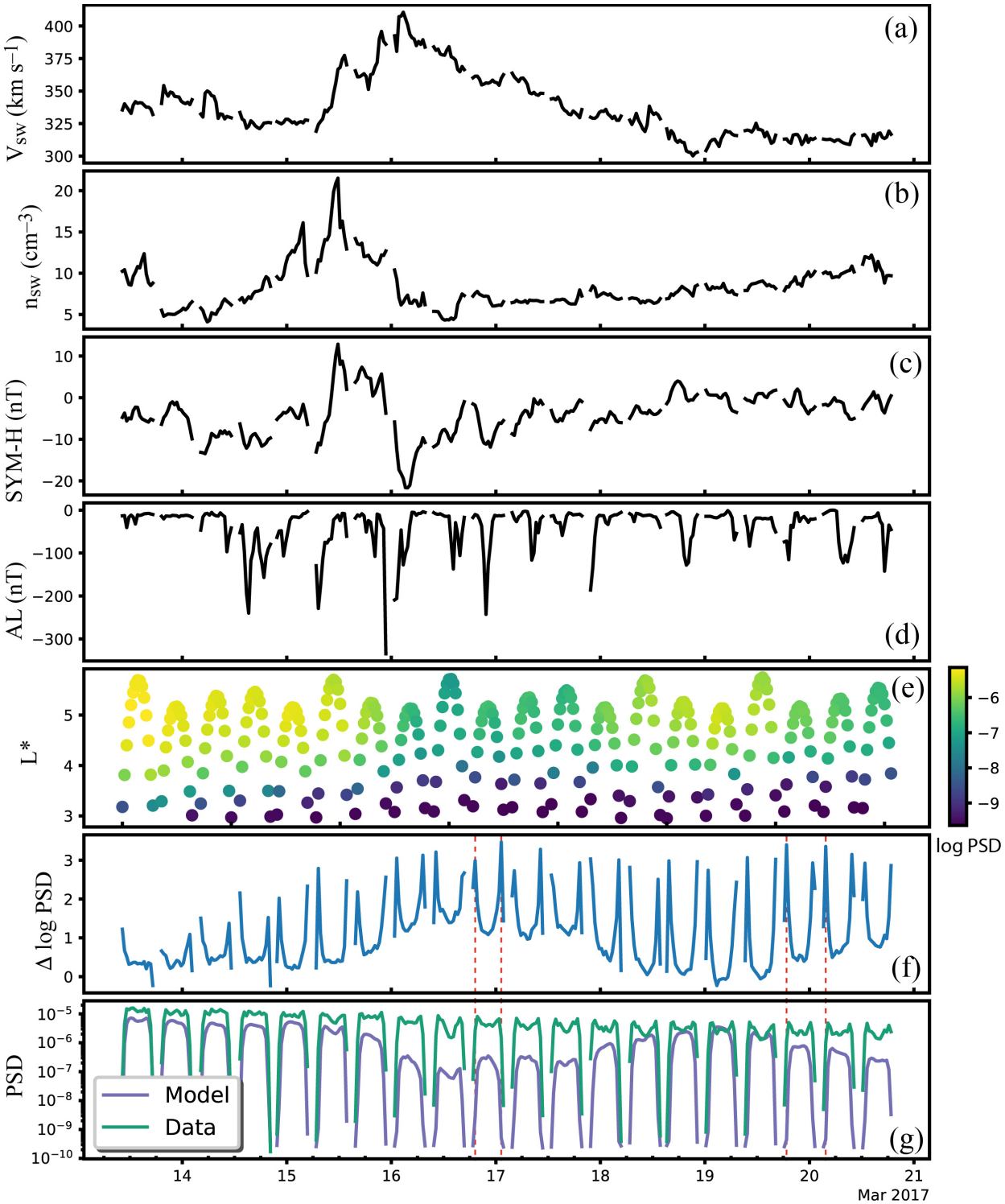

Figure 6. Solar wind velocity (a), solar wind density (b), SYM-H (c), AL (d), L* and log model PSD (e), Δ log PSD = log(observed PSD) – log(model PSD) (f), and observed (green curve) and model PSD (blue curve) (g) for 2017 Mar 13 – 21, which is the first half of the second event. The unit for PSD and ΔPSD is (c^3 MeV^{-3} cm^{-3}). In panels f and g, dotted vertical red lines are drawn to show that generally large |Δ log PSD| can be associated with low PSD.

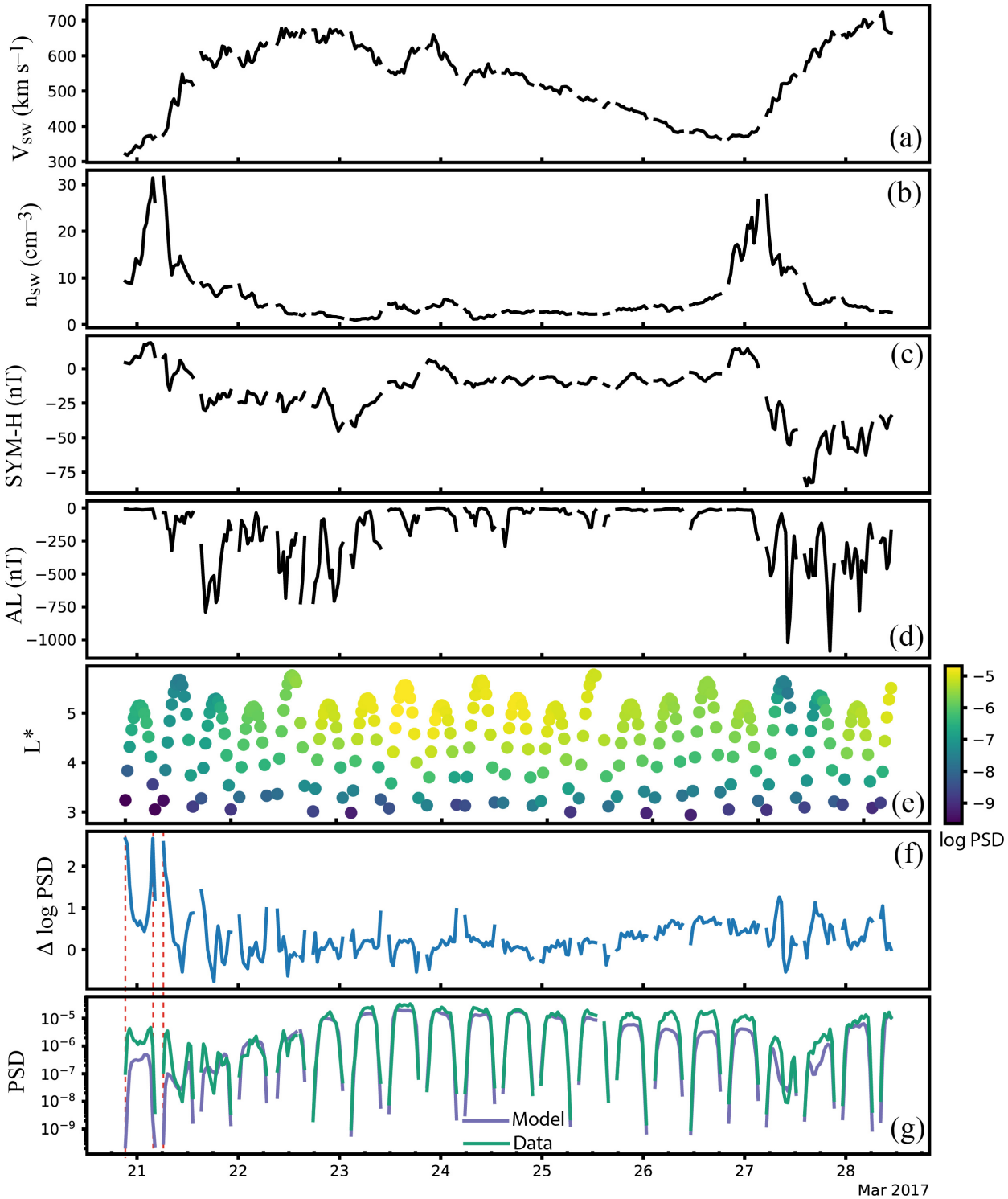

Figure 7. Solar wind velocity (a), solar wind density (b), SYM-H (c), AL (d), L* and log model PSD (e), Δ log PSD = log(observed PSD) – log(model PSD) (f), and observed (green curve) and model PSD (blue curve) (g) for 2017 Mar 21 – 29, which is the second half of the second event. The unit for PSD and ΔPSD is (c^3 MeV^{-3} cm^{-3}). In panels f and g, dotted vertical red lines are drawn to show that generally large |Δ log PSD| can be associated with low PSD.

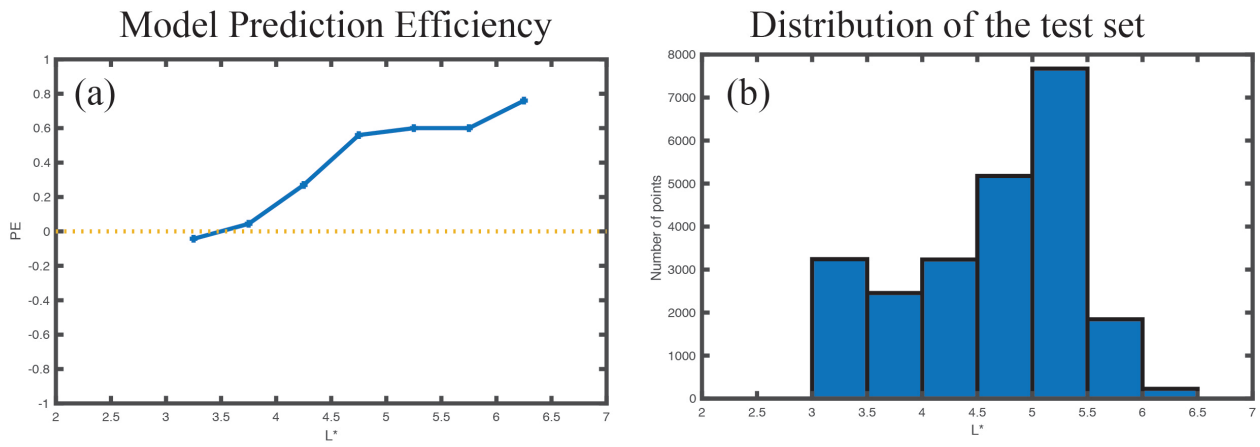

Figure 8. The model prediction efficiency (PE) of the test set as a function of L* (a). The PE is lower at L* < 4 or 4.5 because solar wind and magnetospheric parameters transfer little information to PSD at these L*. The distribution of the test set (b).

Untangling the solar wind and magnetospheric drivers of the radiation belt electrons

Simon Wing[1], Jay R. Johnson[2], Drew L. Turner[1], Aleksandr Y. Ukhorskiy[1], and Alexander J. Boyd[3]

[1]The Johns Hopkins University, Applied Physics Laboratory, Laurel, Maryland, USA

[2]Andrews University, Berrien Spring, Michigan, USA

[3]The Aerospace Corporation, El Segundo, California, USA

Abstract. Many solar wind parameters correlate with one another, which complicates the causal-effect studies of solar wind driving of the magnetosphere. Conditional mutual information (CMI) is used to untangle and isolate the effect of individual solar wind and magnetospheric drivers of the radiation belt electrons. The solar wind density (n_{sw}) negatively correlates with electron phase space density (PSD) (average energy ~ 1.6 MeV) with time lag (τ) = 15 hr. This effect of n_{sw} on PSD has been attributed to magnetopause shadowing losses, but when the effect of solar wind velocity (V_{sw}) is removed, τ shifts to 7–11 hr, which is a more accurate time scale for this process. The peak correlation between V_{sw} and PSD shifts from τ = 38 to 46 hr, when the effect of n_{sw} is removed. This suggests that the time scale for electron acceleration to 1–2 MeV is about 46 hr following V_{sw} enhancements. The effect of n_{sw} is significant only at L* = 4.5–6 (L* > 6 is highly variable) whereas the effect of V_{sw} is significant only at L* = 3.5–6.5. The peak response of PSD to V_{sw} is the shortest and most significant at L* = 4.5–5.5. As time progresses, the peak response broadens and shifts to higher τ at higher and lower L*, consistent with local acceleration at L* = 4.5–5.5 followed by outward and inward diffusion. The outward radial diffusion time scale at L* = 5–6 is ~40 hr per R_E.

ORCID ID: 0000-0001-9342-1813

Plain Language Summary

Many solar wind parameters correlate with one another, which complicates the causal-effect studies of solar wind driving of the magnetosphere. We use conditional mutual information (CMI), which is part of information theory, to untangle and isolate the effect of individual solar wind and magnetospheric drivers of the radiation belt electrons. For example, the solar wind density negatively correlates with electron phase space density (PSD) (average energy ~ 1.6 MeV) with the response time lag of 15 hours. This has been attributed to the electron loss process called magnetopause shadowing. The time lag suggests the time scale for this process is 15 hours. However, when the effect of solar wind velocity is removed, the time lag is 7–11 hours, which is a more accurate time scale for this process. As another example, the time lag of the correlation between solar wind velocity and PSD shifts 38 to 46 hours, when the effect of solar wind density is removed. This suggests that the time scale for electron acceleration to 1–2 MeV is about 46 hours following the solar wind velocity enhancements. We also show that the effects of solar wind velocity and density have dependence on radial distance.

Keywords: radiation belt, relativistic electrons, solar wind drivers, nonlinear relationships, information theory, local acceleration, diffusion time scale, electron acceleration, magnetopause shadowing.

Index terms: 2774, 2784, 2720, 2730, 4499

Major science question:

New Science knowledge:

Broad Implications: Information theoretical tools can be useful to untangle and isolate individual solar wind and magnetospheric drivers of the radiation belt.

Key points: (1) The effect of n_{sw} on radiation belt electrons is significant only at L* = 4.5–6 and not significant at L* < 3. (2) The effect of V_{sw} on radiation belt electrons is significant at L* = 3.5–6.5 and not significant at L* < 3.5. (3) The radiation belt response time lag to V_{sw} suggests local acceleration at L* = 4.5–5.5 followed by outward and inward diffusion.

1. Introduction

The Earth's radiation belt is populated by electrons having energies of hundreds of keVs to >10 MeVs. These electrons are hazardous to satellites that encounter them in the inner-magnetosphere r ~2–8 R_E, including at the geosynchronous orbit (GEO), and at their foot points at low earth orbit (LEO) in the ionosphere, where 1 R_E = radius of the Earth = 6372 km. The MeV electrons can penetrate deep into spacecraft leading to spacecraft or instrument malfunctions while those with energies < 1 MeV can accumulate on the surface of the spacecraft bodies, leading to electrical discharges.

It has long been recognized that the variabilities of the radiation belt electrons, to a large extent, are driven by the solar wind (e.g., *Baker et al*., 2018; *Li et al*., 2001; *Turner and Li*, 2008, *Reeves et al.*, 2013; *Xiang et al*., 2017; *Pinto et al*., 2018; *Zhao et al*., 2017). However, many solar wind parameters positively and negatively correlate with one another, which can complicate the interpretation of the solar wind drivers of the radiation belt (e.g., *Wing et al*., 2016; *Borovsky*, 2018; 2020; *Maggiolo et al*., 2017). For example, solar wind velocity (V_{sw}) positively correlates with radiation belt electron fluxes (J_e) (e.g., *Paulikas and Blake*, 1979; *Baker et al*., 1990; *Reeves et al*., 2011; *Balikhin et al*., 2011; *Li et al*., 2005; *Wing et al*., 2016). Solar wind density (n_{sw}) negatively correlates with radiation belt J_e (e.g., Li et al., 2005; *Lyatsky and Kazanov*, 2008; *Kellerman and Shprits*, 2012; *Rigler et al*., 2007; *Balikhin et al*., 2011; *Wing et al*., 2016). However, V_{sw} negatively correlates with n_{sw} (e.g., *Wing et al*., 2016; *Borovsky*, 2020). This raises the question that given the V_{sw}-n_{sw} negative correlation, if V_{sw} positively correlates with radiation belt electron J_e, then the negative correlation of n_{sw} with radiation belt electron J_e may simply be coincidental. Conversely, given the solar wind property, if n_{sw} negatively correlates with J_e, then the positive correlation of V_{sw} and radiation belt J_e may simply be coincidental. Of course, n_{sw} and

77 V_{sw} may independently exert influence on the radiation belt electrons. In that case, how can one
78 isolate the effect of an individual solar wind parameter?

79 A few studies attempted to separate the effects of n_{sw} from V_{sw} by using methods that bin
80 the data into small intervals of V_{sw} and n_{sw} or explicitly select events when one parameter is nearly
81 constant while the effect of the other parameter is investigated (e.g., *Lyatsky and Khazanov*, 2008).
82 This type of analysis has offered insights into the solar wind driving of the radiation belt J_e.
83 However, holding one parameter nearly constant, either explicitly or through small binning, in
84 order to investigate the second parameter does not completely eliminate the effect of the first
85 parameter. For example, selecting events when V_{sw} is nearly constant to investigate the effect of
86 n_{sw} does not completely eliminate the effect of V_{sw} because V_{sw} or its effect is not zero. Nearly
87 constant but high V_{sw} can still affect the correlation of n_{sw} and radiation belt J_e. Moreover, it does
88 not address the question of how much additional information n_{sw} provides to J_e, given V_{sw} and vice
89 versa. Many studies have shown that other solar wind parameters and magnetospheric parameters
90 can also contribute to J_e variations [e.g., *Balikhin et al*., 2011; *Rigler et al*., 2007; *Vassiliadis et*
91 *al*., 2005; *Li et al*., 2005; *Simms et al.*, 2014;], but presently, it is not entirely clear quantitatively
92 given a main driver, e.g., V_{sw} (or n_{sw}), how much additional information these parameters provide
93 to J_e.

94 The solar wind–magnetospheric system has been shown to be nonlinear [e.g., *Wing et al*.,
95 2005; *Johnson and Wing*, 2005; *Reeves et al*., 2011; *Kellerman and Shprits*, 2012; *Wing et al*.,
96 2016]. For nonlinear system, linear correlational analysis can be misleading [e.g., *Balikhin et al*.,
97 2010; 2011].

98 Information theory has been shown to be quite useful for studies of the Earth's
99 magnetosphere (*Balasis et al*., 2009; *Stumpo et al*., 2020; *March et al*., 2005; *Johnson and Wing*,

2005; 2014, *Wing et al*., 2016; *Johnson et al*., 2018; *Runge et al*., 2018; *Papadimitriou et al*., 2020; *Manshour et al*., 2021), Kronian magnetosphere (*Wing et al*., 2020), and the Sun (*Consolini et al*., 2009; *Wing et al.*, 2018; *Snelling et al*., 2020). Information theory can help identify nonlinearities in the system and information transfer from one variable to another. Moreover, information theory can also help untangle the drivers that are positively or negatively correlated with one another (*Wing et al., 2016*; *Wing and Johnson*, 2019).

Wing et al. (2016) used information theoretic tools to study the solar wind driving of the radiation belt electrons. The study used the publicly available Los Alamos National Laboratory (LANL) satellite data, which provide geosynchronous electron flux measurements at daily resolution. When the study began in early 2015, the Radiation Belt Storm Probes (RBSP) or Van Allen Probes satellites had only been operational for a few years, and there was not enough data for a statistical study. Usage of the daily resolution of the radiation belt electron data prevented *Wing et al*. (2016) from resolving any electron response lag time to the solar wind drivers that is shorter than 24 hours. For example, the LANL MeV electron J_e negatively correlates with daily averaged n_{sw} with a lag time (τ) of 1 day. Zhao et al. (2017) correlated daily averaged radiation belt electron phase space density (PSD) with n_{sw} and also obtained τ = 1 day for MeV electrons (μ > 700 MeV G^{-1}). However, if the effect of V_{sw} is properly removed, τ shifts to 0 day (*Wing et al*., 2016). In other words, the radiation belt electron response to n_{sw} is less than 24 hr. However, the study could not pinpoint exactly how much less than 24 hr with the daily resolution LANL data. Another limitation of *Wing et al*. (2016) study is that the LANL data only provide the electron observations at a fixed radial distance from the Earth, at the geosynchronous orbit.

Since *Wing et al.* (2016) study, RBSP has gathered seven years of radiation belt electron data (2013-2019) at high time resolution (< 1 min) from $2 < L^* < 7$. Hence, the time is ripe for a

follow up study that uses the RBSP data. As in *Wing et al*. (2016), the present study uses information theory to determine the solar wind and magnetospheric drivers of the radiation belt electrons and the response time scales. In order to focus on the drivers of the nonadiabatic heating and acceleration, the present study examines the response of the radiation belt electron phase space density (PSD) to the drivers.

2. Data set

Van Allen Probe (or RBSP) mission, which was launched in 2012, had two identically instrumented spacecraft in near-equatorial orbit (about 10° inclination) with perigee at 600 km altitude and apogee at 5.8 R_E geocentric (*Mauk et al.*, 2013). The MAGnetic Electron Ion Spectrometer (MagEIS) and Relativistic Electron-Proton Telescope (REPT) instruments are part of the Energetic particle, Composition, and Thermal plasma Suite (ECT) instrument on board of RBSP (*Spence et al.,*, 2013). MagEIS measured the energy range of 30 keV to 4 MeV for electrons and 20 keV to 1 MeV for ions (*Blake et al*., 2013) while REPT measured electrons with energy range 1.5 to ≥ 10 MeV and protons with energy range 20 to 75 MeV (*Baker et al*., 2012).

The present study focuses only on the electron data. Radiation belt electron dynamics can often be described by their adiabatic invariants and PSD (μ, K, L*) where μ = the first adiabatic invariant related to the gyromotion perpendicular to the magnetic field line, K = the second adiabatic invariant related to the bounce motion along the field line, and L or L* = the third adiabatic invariant related to the curvature and gradient drift motion around the Earth (actually L* is inversely proportional to the third invariant Φ) (*Roederer*, 1970; *Schulz and Lanzerotti*, 1974; *Lejosne and Kollman*, 2020).

Data from the RBSP-ECT Combined dataset (Boyd et al., 2021) are used to obtain electron

PSD as a function of adiabatic invariants across the full MagEIS and REPT energy range. The PSD is calculated using the techniques outlined in (*Turner et al.*, 2014a; 2014b; *Boyd et al.*, 2014) at ~5 min time cadence. The PSD calculation uses TS04 magnetic field model (*Tsyganenko and Sitnov*, 2005). We select the electrons with μ = 725–875 MeV G^{-1} and K = 0.09–0.13 R_E $G^{-0.5}$. These electrons have an average energy of ~1.6 MeV, but they range from 480 keV to 4.8 MeV spanning over L* of 2.5 to 6.8.

The solar wind, AL, and SYM-H data 2013-2019 come from OMNI 1 min resolution data provided by NASA (http://omniweb.gsfc.nasa.gov/). Both the PSD and OMNI data 2013-2019 are averaged with 30 min sliding window.

We merge each OMNI solar wind parameter (V_{sw}, n_{sw} etc.) with the RBSP electron PSD. As described in Section 3, we perform time shifted correlation and conditional mutual information analysis to determine the radiation belt electron response lag time up to 120 hr. Depending on the solar wind parameter, typically the merged datasets have approximately 60,000 to 85,000 points.

3. Methodology

Mutual information and conditional mutual information are briefly described below, but they are also described in *Balasis et al*. (2013), and *Wing et al*. (2016, 2018).

Let variables x and y have n and m elements in sets $\aleph_1$ and $\aleph_2$, respectively,

$$x \in \{\hat{x}_1, \hat{x}_2, \cdots, \hat{x}_n\} \equiv \aleph_1; \quad y \in \{\hat{y}_1, \hat{y}_2, \cdots, \hat{y}_m\} \equiv \aleph_2 \qquad (1)$$

The entropy associated with each of the variables is defined as

$$H(x) = -\sum_{\aleph_1} p(\hat{x}) \log p(\hat{x}) ; \qquad H(y) = -\sum_{\aleph_2} p(\hat{y}) \log p(\hat{y}) \qquad (2)$$

where $p(\hat{x})$ is the probability of finding the word $\hat{x}$ in the set of x-data and $p(\hat{y})$ is the probability of finding word $\hat{y}$ in the set of y-data. To examine the relationship between the variables, we

extract the word combinations $(\hat{x}, \hat{y})$ from the dataset. The joint entropy is defined by

$$H(x,y) = -\sum_{\aleph_1 \aleph_2} p(\hat{x},\hat{y}) \log p(\hat{x},\hat{y}) \quad (3)$$

where $p(\hat{x},\hat{y})$ is the probability of finding the word combination $(\hat{x},\hat{y})$ in the set of (x, y) data. Then, the mutual information (MI) (*Tsonis*, 2001; *Li*, 1990; *Darbellay and Vajda*, 1999) is defined as

$$\mathrm{MI}(x, y) = \mathrm{H}(x) + \mathrm{H}(y) - \mathrm{H}(x, y) \quad (4)$$

MI compares the uncertainty of measuring variables jointly with the uncertainty of measuring the two variables independently. MI gives a measure of linear and nonlinear dependence between two variables. Conditional mutual information (CMI) gives a measure of conditional dependency with respect to a conditioner variable z where $\hat{z} \in \{ z_1, z_2, \ldots z_k\} \equiv \aleph_3$. CMI is defined as (Wyner, 1978)

$$\mathrm{CMI}(x, y \mid z) = \sum_{\aleph_1 \aleph_2 \aleph_3} p(\hat{x},\hat{y},\hat{z}) \log \frac{p(\hat{x},\ \hat{y} \mid \hat{z})}{p(\hat{x} \mid \hat{z})\, p(\hat{y} \mid \hat{z})} = \mathrm{H}(x,z) + \mathrm{H}(y,z) - \mathrm{H}(x,y,z) - \mathrm{H}(z) \quad (5)$$

CMI determines the mutual information between x and y given that z is known. In other words, CMI determines how much additional information is known given another variable. If x or y is known based on z, then $\mathrm{CMI}(x,y|z) = 0$. The maximum CMI occurs when x and y do not depend on the conditioner variable z, in which case $\mathrm{CMI}(x, y|z) = \mathrm{MI}(x, y)$ and the maximum CMI and MI is $\max(\mathrm{H}(x), \mathrm{H}(y))$. CMI is a special case of the more general conditional redundancy that allows the variable z to be a vector (e.g., *Prichard and Theiler*, 1995; *Johnson and Wing*, 2014).

Herein, we use the short hand Pearson's linear correlation $\mathrm{corr}(x(t), y(t + \tau))$ as $\mathrm{corr}(x \rightarrow y)$. Likewise, $\mathrm{CMI}(x(t), y(t + \tau)| z(t))$ is denoted as $\mathrm{CMI}(x \rightarrow y| z)$. We define i_{tr} = information transfer = $\mathrm{CMI}(x \rightarrow y| z)$ – mean noise, where noise = $\mathrm{CMI}(\mathrm{sur}(x) \rightarrow y| z)$, $\mathrm{sur}(x)$ is the surrogate data of x and is obtained by randomly permuting the order of the time series of array x. Mean and σ of the noise are calculated from an ensemble of 100 values of $\mathrm{CMI}(\mathrm{sur}(x) \rightarrow y| z)$. The mean

noise and σ estimate are valuable diagnostics included on all of the CMI data presented here: any CMI outside the 3σ noise range are significant and CMI less than the 3σ from the noise is considered not significant. Furthermore, we define $i_{tr\_max} = i_{tr}$ at the peak τ and significance = i_{tr}/σ.

We note that the surrogate data is constructed to be consistent with our null hypothesis. In our correlation and CMI analysis, the null hypothesis is that variables *x* and *y* are unrelated (random). We test whether *x* and *y* are (linearly and nonlinearly) correlated. If we would like to determine the degree to which *x* and *y* are nonlinearly correlated or if we would like to remove the linear correlation from our CMI, then we could use a red noise type surrogate such that CMI would be insignificant if *x* and *y* are linearly correlated. We could also use the method described in *Prichard and Theiler* (1995) and later used in *Johnson and Wing* (2005) to construct surrogates that share the same linear correlations as the original data to isolate the nonlinear dependence. As a future study, it would be interesting to explore different types of surrogate data.

4. Applying information theory to radiation belt MeV electron data

4.1 A simple example of an application of conditional mutual information (CMI)

CMI can be quite useful to untangle the effects of multiple drivers of a system. Figure 1 presents a simple example that illustrates this point. Figure 1a plots corr($V_{sw} \rightarrow$ PSD). The figure shows that V_{sw} positively correlates with PSD and the correlation peaks at τ = 38 hr. The correlation is significant with n = 84,729 points and correlation coefficient (r) = 0.47 and $p < 0.01$. Previous studies have also found good correlations between V_{sw} and radiation belt electrons with ~2 days lag and the lag time has been attributed to the time scale to accelerate the electrons to 1–2 MeV due to local acceleration, radial transport, or some other acceleration mechanisms (e.g.,

Baker et al., 1990; *Shprits et al.*, 2008; *Reeves et al*., 2011; *Li et al*., 2005; *Ukhorskiy et al*., 2005; *Summers et al*., 2007; *Thorne et al*., 2013; *Turner and Li*, 2008; *Boyd et al.*, 2018). Figure 1b plots the corr($n_{sw} \rightarrow$ PSD), which shows that n_{sw} negatively correlates with PSD with a minimum at τ = 15 hr, r = –0.22, n = 84,729, $p < 0.01$. *Lyatsky and Khazanov* (2008) also found the same negative correlation at τ = 15 hr. The negative correlation has been previously attributed to the magnetopause shadowing: an increase in n_{sw} would increase solar wind dynamic pressure (P_{dyn}), which would compress the magnetosphere leading to radiation belt electron losses (e.g., *Li et al.*, 2001; *Kellerman and Shprits*, 2012; *Turner et al*., 2012; *Ukhorskiy et al*., 2006). Figure 1c plots the corr($P_{dyn} \rightarrow$ PSD), which shows that the radiation belt electron response to P_{dyn}, which is ~ n_{sw} V_{sw}^2, has dual modes. At small τ, τ < ~20 hr, P_{dyn} negatively correlates with PSD, which is similar to the effect of n_{sw} and can be attributed to the magnetopause shadowing. However, at large τ, τ > 40 hr, P_{dyn} positively correlates with PSD, which is similar to the effect of V_{sw}. The correlations are significant at $p < 0.01$ and n = 82,652. Zhao et al. (2017) correlated P_{dyn} with PSD at daily time resolution and also found a dual response mode of the PSD to P_{dyn}. Figure 1d plots CMI($P_{dyn} \rightarrow$ PSD| n_{sw}), which shows the dependence of PSD on P_{dyn}, given n_{sw}. It shows that if we remove the effect of n_{sw}, the effect of P_{dyn} on PSD is similar to that of V_{sw} in Figure 1a, as expected. The CMI curve does not match exactly the correlation curve in Figure 1a because the CMI curve takes into account the nonlinearities in the data.

In Figure 1d, the green solid and dashed curves are mean noise and 3σ from the noise, respectively. The significance at peak τ = 51 hr is 203σ and hence it is significant.

4.2 Isolating the effects of the solar wind velocity from density and vice versa

Wing et al. (2016) isolated the effects of V_{sw} and n_{sw} on the radiation belt electron J_e using

CMI. They found that CMI($V_{sw} \rightarrow J_e | n_{sw}$) peaks at τ = 2-3 days while CMI($n_{sw} \rightarrow J_e | V_{sw}$) peaks at τ = 0 day. However, the lag times, τ, in *Wing et al*. (2016) are imprecise due to the usage of the daily resolution LANL electron data. Furthermore, LANL data are limited to GEO, but the outer belt is not accurately represented by data at GEO alone, especially for the heart of the outer belt between $4 \leq L \leq 5$ (e.g., *Baker et al*., 2019b). In the present study, we recompute the CMIs using 30 min resolution RBSP PSDs representative of ~1 MeV electrons throughout the entire outer belt and solar wind data. Furthermore, by using electron PSD for fixed values of the first and second adiabatic invariants in place of J_e as a function of energy, the data used here further deconvolute the energy and pitch angle dependencies of the underlying physical processes that drive radiation belt enhancements and losses.

Figures 2a and 2b replot corr($V_{sw} \rightarrow$ PSD) and corr($n_{sw} \rightarrow$ PSD), which are plotted in Figures 1a and 1b, respectively. However, V_{sw} negatively correlates with n_{sw} and corr($V_{sw} \rightarrow n_{sw}$) has a minimun at τ = 15 hr (r = –0.48, n = 105,459, $p < 0.01$), as shown in Figure 2c. For completeness, Figure 2c also plots corr($n_{sw} \rightarrow V_{sw}$) (red curve), which has r = 0.10, $p < 0.01$. The figure shows that $|\text{corr}(V_{sw} \rightarrow n_{sw})| > |\text{corr}(n_{sw} \rightarrow V_{sw})|$. The negative correlation between V_{sw} and n_{sw} have been previously reported with similar τ (e.g., *Wing et al*., 2016; *Maggiolo et al*., 2017; *Borovsky*, 2020). Note that τ may vary from year to year (*Wing et al*., 2016), leading to an overall broadening of the peak when considering an ensemble of intervals across the solar cycle.

Given that V_{sw} negatively correlates with n_{sw}, if n_{sw} negatively correlates with PSD (Figure 2b), then the positive correlation between V_{sw} and PSD may be deemed just coincidental. Figure 2d, which plots CMI($V_{sw} \rightarrow$ PSD| n_{sw}), shows that even after the effect of n_{sw} has been removed, there is still strong information transfer from Vsw to PSD, which peaks at τ = 46 hr (n = 78,811, significance = 378σ). Apparently, removing the effect of n_{sw}, shifts the peak to the right. The lag

time of $\tau = 46$ hr obtained from CMI is considered a more accurate radiation belt electron response time to the V_{sw} (the time scale for electron acceleration to 1-2 MeV energy range) than the lag time of $\tau = 38$ hr obtained from Pearson's correlation.

We can also check whether or not corr($n_{sw} \rightarrow$ PSD) is coincidental. Figure 2e plots CMI($n_{sw} \rightarrow$ PSD$|\ V_{sw}$), which shows two peaks. The primary peak at τ = 7–11 hr (n = 78,811, significance = 52σ) can be compared to the minimum in corr($n_{sw} \rightarrow$ PSD) in Figure 2b. Apparently, removing the effect of V_{sw}, shifts the peak to the left. The lag time of τ = 7–11 hr is considered a more accurate radiation belt electron response time to the magnetopause shadowing than the τ = 15 hr obtained from the correlational analysis. Note that CMI only gives positive values and does not distinguish negative from positive correlations. As such, CMI is analogous to $|r|$.

Figure 2e shows that there is a secondary broad peak at τ = 80–120 hr (or even larger). Unlike the primary peak, which is a negative correlation, the secondary peak is a positive correlation with n_{sw}. In order to show this, we plot PSD(t + τ) vs. V_{sw}(t) vs. n_{sw}(t) for τ = 0, 5, 10, 40, 80, 100, and 120 hr in Figure 3 panels a to g, respectively. In all panels, it can be seen that at high V_{sw}, V_{sw} > ~500 km s^{-1}, V_{sw} positively correlates with the radiation belt electron PSD as previously reported (*Reeves et al*., 2011; *Wing et al*., 2016). However, for V_{sw} < ~450 km s^{-1}, and small τ (τ = 0, 5, and 10 hr), n_{sw} negatively correlates with the radiation belt electron PSD, e.g., yellow and brown region clustering at the bottom, which corresponds to the first and primary peak in Figure 2e. At τ = 40 hr, there is little or no correlation between n_{sw} and the PSD, which corresponds to the minimum in Figure 2e. However, at large τ, τ = 80, 100, 120 hr and V_{sw} < ~450 km s^{-1}, n_{sw} positively correlates with PSD, e.g., yellow and brown region clustering at the top, which corresponds to the secondary peak in Figure 2e. This positive correlation between n_{sw} and

electron PSD at large τ cannot be seen in the corr(n_{sw} → PSD) in Figure 2b because the effect has been smeared or cancelled out by the effects for all V_{sw} where high electron PSD can correspond to high and low n_{sw} (Figure 3 panels e–g).

It is not clear what causes the positive linear and nonlinear correlation between n_{sw} and electron PSD at large τ. n_{sw} may be a proxy for another parameter. For example, n_{sw} positively correlates with |IMF B| (*Borovsky*, 2020; *Maggiolo et al*., 2017). Whatever the mechanism is, our result shows that the time scale for such process to energize electrons to 1–2 MeV is slow, > 80 hr.

4.3 The radial dependence of the radiation belt electrons on the solar wind density and velocity

The effects of the n_{sw} and V_{sw} on the radiation belt electrons have a dependence on the radial distance or L* (e.g., *Baker et al*., 2019a; *Tang et al*., 2017; *Turner et al*., 2019; *Zhao et al*., 2017; *W. Li et al*., 2014). In order to show this, PSD data are binned from L* = 3 to 6.5 into 7 bins with bin width = 0.5. The data coverage for the electrons with μ = 725–875 MeV G^{-1} and K = 0.09–0.13 R_E $G^{-0.5}$ is poor for L* < 3 and L* > 6.5. Figure 4 shows corr(n_{sw} → PSD) as a function of L*. It shows that the correlation is near 0 at L* = 3–3.5, but slowly decreases with increasing L*. Except for L* = 3–3.5 (n = 8435, Figure 4a), the correlations are significant ($p < 0.01$) at the minimum τ (τ = 15, 16, 17, 17, 17, 13 hr), r = (–0.086, –0.17, –0.27, –0.31, –0.34, –0.50), (n = 8,302, 11,481, 17,7891, 27,060, 6,236, 528) for panels (b–g), respectively. The number of points in L* = 6–6.5 (Figure 4g) is the fewest, which results in a noisier correlation. However, as discussed in the Sections 1, 4.1, and 4.2, the correlation may be inaccurate because n_{sw} negatively correlates with V_{sw} (Figure 2c) and the system is nonlinear (Wing et al., 2016). Hence, we calculate

307 CMI($n_{sw} \rightarrow$ PSD| V_{sw}) for the PSD data in the same bins. The results are plotted in Figure 5. The
308 figure shows that the effect of n_{sw} on PSD is at the noise level at L* = 3–4.5, is significant at L* =
309 5–6, and back to the noise level at L* = 6–6.5. However, the result for L* = 6–6.5 is considered
310 not reliable because of the small number of points (n = 528). The response lag times based on the
311 first peak are τ = 9, 10, and 7 hr (n = 16,629, 25,238, and 5865; significance = 17, 42, and 5 σ) at
312 L* = 4.5–5, 5–5.5, and 5.5–6, respectively. Notice that the response lag times are quite different
313 in Figures 4 and 5.

314 For completeness, we examine the effect of P_{dyn} on the PSD. Figure 6 plots CMI($P_{dyn} \rightarrow$
315 PSD| V_{sw}) as a function of L* in the same format as Figure 5. It shows that the effect of P_{dyn} on
316 PSD is similar to that of n_{sw}, as expected. The largest effect of P_{dyn} on electron PSD can be found
317 at L* = 4.5–6. (significance = 32, 53, 17 σ for L* = 4.5–5, 5–5.5, and 5.5–6), respectively. The
318 number of points in each bin in Figure 5 is the same as that in Figure 6. Taken together, Figures
319 5 and 6 suggest that the magnetopause shadowing is effective only at L* = 4.5–6. At L* = 6–6.5,
320 there is a high variability of PSD and the bin has fewest number of points and hence the result is
321 inconclusive.

322 Moreover, the significances are higher for the first peak in Figure 6 panels d–f than their
323 counterparts for CMI($n_{sw} \rightarrow$ PSD| V_{sw}) in Figure 5 panels d–f, suggesting that the real causal
324 parameter for the magnetopause shadowing is P_{dyn} rather than n_{sw}. However, the opposite is true
325 for the secondary peak. This would suggest that the secondary peak may be more causally related
326 to n_{sw} (or its proxy) than P_{dyn}.

327 We perform the same analysis with V_{sw} and electron PSD. Figure 7 shows corr($V_{sw} \rightarrow$
328 PSD) as a function of L* in the same format as Figure 4. The correlations are all significant at $p <$
329 0.01 at the maximum τ (τ = 40–120, 30–120, 38, 30, 37, 45, 30–90 hr), (r = 0.14, 0.27, 0.42. 0.57,

330 0.62, 0.64, 0.70) for L* = 3–3.5, 3.5–4, 4.–4.5, 4.5–5, 5–5.5, 5.5–6, and 6–6.5, respectively. Baker
331 et al. (2019a) also found higher correlation with increasing L (r = 0.32, 0.51, and 0.61 for L = 3.5,
332 4.5, and 5.5, respectively). For comparison, Figure 8 plots CMI($V_{sw} \rightarrow$ PSD| n_{sw}) as a function of
333 L* in the same format as Figure 5. The number of points in each bin is the same as that in Figure
334 5. Figure 8 shows that the CMI is at the noise level at L* = 3–3.5 (panel a), unlike its counterpart
335 in Figure 7a. At L* = 3.5–4.5, the CMI has a broad peak from $\tau \sim$ 50–100 hr (or larger for the case
336 L* = 3.5–4) and the peaks are significant (peak significance = 18 and 46 σ for L* = 3.5–4 and 4–
337 4.5), respectively. At L* = 4.5–6, the CMI peaks are narrower (peak τ = 40, 46, 57 hr; significance
338 = 236, 399, and 100 σ), respectively. Interestingly, at τ = 6–6.5, the peak broadens again but
339 remains significant (peak significance = 19 σ). To help visualize the evolution of the CMI, red
340 dashed vertical lines at τ = 40 hr is drawn in Figure 8.
341 The radiation belt electron response lag times as a function of L* is further examined in
342 Figure 9. The figure shows the normalized i_{tr} for each L* bin (the blue curve subtracted by the
343 solid green curve in Figure 8). The orange and yellow color correspond roughly to the top 20% of
344 i_{tr} in each L* bin. At L* = 4.5–5.5, response lag time peaks around τ = 35–50 hours, which is
345 consistent or close to the previously reported time scale of 2 days to accelerate electrons to 1-2
346 MeV (*Paulikas and Blake*, 1979; *Reeves et al*., 2011; *Li et al*., 2001; *Wing et al*., 2016). At higher
347 L*, L* = 5.5–6, the peak broadens and shifts to larger τ, τ = 45–65 hr. At L* = 6–6.5, the peak is
348 even broader at τ = 40–100 hr. At lower L*, L* = 4–4.5 and 3.5–4, one can also see successive
349 broadening of the peak as the peak shifts to larger τ, τ = 35–55 hr and τ = 45–60 hr, respectively.
350 Section 5.3 discusses how the result is consistent with local acceleration where the peak of the
351 electron acceleration region is located at L* = 4.5–5.5, from where electrons diffuse outward and
352 inward.

353

354 **4.4 The dependence of the radiation belt electrons on the magnetospheric state**

355 The radiation belt electrons depend not just on the external (solar wind) drivers but also
356 the internal state of the magnetosphere (e.g., *Baker et al.*, 2019a; *Borovsky and Denton*, 2014;
357 *Borovsky*, 2017; *Zhao et al*., 2017). In order to determine how the radiation belt electrons depend
358 on the internal state of the magnetosphere, we examine the relationships of the electron PSD with
359 AL and SYM-H indices. SYM-H index gives a measure of the strength of the ring current and
360 storm (*Iyemori*, 1990) while AL gives a measure of the strength of the westward auroral electrojets
361 and substorm (*Davis and Sugiura*, 1966). SYM-H is similar to Disturbance Storm Time (D_{st})
362 index (*Dessler and Parker*, 1959), except that SYM-H index is defined to have a one minute time
363 resolution whereas D_{st} index has one hour resolution. Both SYM-H (proxy for storms) and AL
364 (proxy for substorms) can be associated with plasma injections to the inner magnetosphere, which
365 can enhance the whistler mode chorus waves and provide the seed population for the local
366 acceleration (*Katus et al*., 2013; *Wing et al*., 2014).

367 Figure 10a plots corr(AL $\rightarrow$ PSD), which shows that AL negatively correlates with electron
368 PSD with a minimum $\tau \sim 53$ hr ($n = 70{,}125$, $r = -0.33$, $p < 0.01$). A smaller (more negative) AL
369 corresponds to a more intense substorm and larger auroral electrojets. Figure 10b plots corr(V_{sw}
370 $\rightarrow$ PSD) (same as Figure 1a). Figure 10c plots corr($V_{sw} \rightarrow$ AL), which shows that the auroral
371 electrojet response to V_{sw} is fairly quick $\tau = 0$ hr (< 30 min) ($n = 82{,}995$, $r = -0.40$, $p < 0.01$).
372 Similar correlation was obtained by *Smirnov et al*. (2020). Given the positive correlation of V_{sw}
373 and electron PSD, and the negative correlation of V_{sw} and AL, one may ask the question whether
374 the negative correlation between AL and electron PSD may just simply be coincidental or whether
375 AL can independently affect PSD. Figure 10d plots CMI(AL $\rightarrow$ PSD| V_{sw}), which shows that the

radiation belt electrons still have strong dependence on AL even after the effect of V_{sw} has been removed. The CMI peaks at $\tau \sim 50–80$ hr (significance = 58σ, n = 64,564), suggesting that perhaps the time scale to accelerate electrons to 1–2 MeV energy range from the time of substorm onset or substorm particle injection is about 50–80 hr. This time scale is an ensemble average for all L*. To help visualize the comparison of Figures 10a and 10d, a dashed vertical red line is drawn at τ = 53 hr (the minimum of corr(AL $\rightarrow$ PSD)). It shows that removing the effect of V_{sw}, shifts the peak to the right (to a larger τ) by a little bit (~10 hr).

Figure 11 displays the normalized i_{tr} as a function of L* and τ where i_{tr} = CMI(AL $\rightarrow$ PSD| V_{sw}) – mean noise in the same format as Figure 9. The i_{tr} is at the noise level at L* = 3–3.5 (n = 6409). At L* = 6–6.5, there is a high variability in PSD and the bin has the fewest number of points (n = 216) and hence the result is unclear and not shown. The region with the largest significance is L* = 4.5–5 and 5–5.5 with peak τ = 40–80 and 45–85 hr and peak significance = 33 and 38 σ (n = 13,825 and 20,527) respectively. The peak shifts to larger τ, τ = 75–100 hr, at L* = 5.5 –6 (n = 4686, peak significance = 18σ). At L* = 4–4.5, the peak is broad, τ = 35–80 hr (n = 8802; peak significance = 19 σ). At L* = 3.5–4, the peak is broad at τ = 60–110 hr, but the peak significance is relatively small (n = 6379, peak significance = 9 σ). Section 5.3 discusses this result in terms of local acceleration and subsequent inward and outward diffusion.

We perform similar analysis with SYM-H. Figure 12 is similar to Figure 10, except that it is for SYM-H instead of AL index. Figure 12a plots corr(SYM-H $\rightarrow$ PSD), which shows that SYM-H negatively correlates with electron PSD with a minimum at $\tau \sim 40$ hr (n = 91,589, r = –0.35, p < 0.01) while Figure 12b plots corr($V_{sw}\rightarrow$ PSD) (same as Figure 10b). V_{sw} negatively correlates with SYM-H and the correlation has a minimum at τ = 2–4 hr (n = 91,589, r = –0.35, p < 0.01) (Figure 12c), suggesting that the ring current response to V_{sw} has a lag time of about 2–4

hr. Similar correlation was obtained in previous studies (e.g., *Maggiolo et al*., 2017). Figures 12 a–c pose the same dilemma as Figures 10 a–c do for AL. That is, given the positive correlation of V_{sw} and electron PSD and the negative correlation of V_{sw} and SYM-H, one may ask whether the negative correlation of SYM-H and PSD could just simply be coincidental or whether SYM-H provides additional information about PSD. Figure 12d plots CMI(SYM-H $\rightarrow$ PSD| V_{sw}), which shows that SYM-H indeed provides additional information to electron PSD even after the effect of V_{sw} has been removed. The CMI peaks at $\tau \sim$ 30–70 hr (n = 84,729, significance = 109 σ), suggesting that perhaps the time scale to accelerate electrons to 1–2 MeV energy range from the time of ring current enhancement is about 30–70 hr. However, the effect of SYM-H has a dependence on radial distance, as discussed next.

Figure 13 plots i_{tr} as a function of L* where i_{tr} = CMI(SYM-H $\rightarrow$ PSD| V_{sw}) – mean noise in the same format as Figure 11. At L* = 6–6.5, i_{tr} is at the noise level, which can be attributed to high PSD variabilities as well as small number of points (n = 336). The highest peak significance can be found at L* = 5 – 5.5 (peak τ = 20–55 hr, significance = 79σ, n = 27,060). The peak shifts to higher τ at higher L*. At L* = 5.5–6, the peak can be found at τ = 60–75 hr (n = 6236, peak significance = 26 σ). At L* = 4–4.5 and 4.5–5, the i_{tr} peaks at τ = 30–60 and 30–75 hr (n = 11,495 and 17,924; peak significance = 38 and 47 σ, respectively). At L* = 3.5–4, the peak is very broad at τ = 20–120 hr or even higher (n = 8317, peak significance = 23 σ). At L* = 3–3.5, the CMI peaks at τ = 110–120 hr or even higher (n = 8435, peak significance = 14). Section 5.3 discusses this result in terms of local acceleration and the subsequent inward and outward diffusion.

It is worth noting that out of all the parameters that we have examined, only SYM-H can provide information about radiation belt electron PSD at L* = 3–3.5 albeit only a small amount. The CMI at L* = 3–3.5 and τ < 100 hr is low, which is consistent with *Turner et al*. (2019) study

that found storms have little effect on 1–2 MeV electrons at L < 3.5 (see their Figure 2), but apparently at $\tau > 100$ hr, the storm effect is significant but only moderately.

4.5 The rankings of solar wind and magnetospheric parameters by the information transfer to the radiation belt electrons

In the previous sections, we calculate the dependence of the PSD on V_{sw}, n_{sw}, P_{dyn}, AL, and SYM-H. V_{sw} transfers the most information to the PSD by significantly larger amount than any other solar wind variables. In this section, we calculate the CMI from other solar wind parameters to the PSD, given V_{sw}. Specifically, we calculate CMI($x \rightarrow$ PSD| V_{sw}) where x = IMF |B|, $B_z < 0$, $B_z > 0$, B_y, Esw, and σ(IMF B).

Table 1 ranks these parameters based on the information transfer to the radiation belt electron PSD, given V_{sw} for L* = 3 – 6.5. The information transfer is calculated as i_{tr_max} = maximum of (CMI – mean noise). The information transfer from V_{sw} to the PSD is calculated from CMI($V_{sw} \rightarrow$ PSD| n_{sw}). It shows the dominance of V_{sw} in terms of information transfer to the PSD. SYM-H, which is ranked second, transfers only about a quarter as much information to the PSD. In Table 1, if the response lag time has a broad peak, τ is reported as having a range of values. Table 1 shows that the radiation belt electron response lag time to the solar wind and magnetospheric parameters fall into two categories. The electron response with a small τ ($\tau <$ 15 hr) is a decrease in PSD (electron loss) while the response at large τ ($\tau > 40$ hr) is an enhancement in PSD.

Zhao et al. (2017) correlated PSD with solar wind (Vsw, nsw, Pdyn) and magnetospheric parameters (SYM-H, AL) and found that AL has the best correlation with PSD with t = 2-5 days for $\mu > 700$ MeV G^{-1}. However, their study differs from the present study in two key aspects: (1)

their study used daily resolution data; (2) more importantly, they did not remove the effect of Vsw from AL, SYM-H, and other parameters. The second point is particularly consequential because AL negatively correlates with V_{sw} (Figure 10c) and some of the good correlation between AL and PSD can be partially attributed to the good correlation between V_{sw} and PSD.

Many of the parameters, namely IMF |B|, IMF $B_z < 0$, IMF B_y, n_{sw}, and P_{dyn}, produce dual response modes in the radiation belt electrons. At small τ ($\tau < 15$ hr), the response is a decrease in PSD or electron loss while at large τ ($\tau > 30$ hr), the response is an enhancement in PSD. For these parameters, the ranking is based on the mode that has the higher i_{tr_max}. The response to IMF |B| has roughly the same i_{tr_max} at small and large τ, although Table 1 lists the response to the large τ. The response to IMF|B|, IMF $B_z < 0$, and IMF B_y at $\tau < 15$ hr is electron loss and is mainly due to their correlations with n_{sw}. If the effect of n_{sw} is removed, this peak will diminish or disappear.

The ranking presented in Table 1 can be useful for modeling radiation belt electrons. The table may help modelers decide which parameters need to be considered as inputs to their models.

5. Discussion

5.1 Untangling the solar wind and magnetospheric drivers

An important factor that is often ignored and underappreciated in many solar wind-magnetosphere interaction studies is that many solar wind parameters positively or negatively correlate with one another, which may introduce complications and ambiguities in the causal-effect interpretation of the data. In the present study, we use conditional mutual information, CMI, to untangle the effects of the solar wind and magnetospheric drivers of the radiation belt electrons PSD having μ = 725–875 MeV G^{-1} and K = 0.09–0.13 R_E $G^{-0.5}$ (average energy ~1.6 MeV).

The radiation belt electron response time lags to V_{sw}, n_{sw}, AL, and SYM-H obtained from

correlational analysis differ from those obtained from CMIs that have removed the effect of the V_{sw} or n_{sw} as summarized in Table 2 (from Figures 2, 10, and 12). For the purpose of facilitating a more precise comparison, Table 2 lists only the peak τ even if the peak may be broad whereas Table 1 lists a range of τ, if the peak is broad. The response lag times obtained by CMIs are deemed more accurate because the effect of V_{sw} or n_{sw} has been removed. For example, CMI($n_{sw} \rightarrow$ PSD$|\ V_{sw}$) peaks at t = 7–11 hr whereas corr($n_{sw} \rightarrow$ PSD) has a minimum at τ = 15 hr (*Lyatsky and Khazanov*, 2008). The smaller τ is deemed a more accurate time scale for magnetopause shadowing, which physically makes sense and and is consistent with observations (e.g., *Turner et al*., 2014a; *Xiang et al*., 2017; 2018; *Turner and Ukhorskiy*, 2020). The shift in the peak CMI depends on the conditional variable z in the CMI($x \rightarrow y| z$). If the (linear and nonlinear) correlation of z with y is smaller than that between x and y, then removing the effect of z would shift the peak to a larger value and vice versa.

The response of the radiation belt electrons to n_{sw} has dual mode. At small τ, n_{sw} negatively correlates with the electron PSD with a peak response time at τ = 7–11 hr, which can be attributed to the magnetopause shadowing effect. However, at large τ (τ > 80 hr), n_{sw} positively correlates with the electron PSD as shown in Figures 2e and 3. It is not clear what causes this positive correlation. n_{sw} may be a proxy for another solar wind parameter. An increase in n_{sw} is sometimes accompanied by n_{sw} fluctuations, which can drive ULF waves in the magnetosphere and accelerate electrons (e.g., *Kepko and Viall*, 2019, *Ukhorskiy et al*., 2005). Whichever parameter drives the electron acceleration, the result suggests a rather slow process for electron acceleration, τ > 80 hr. This will be investigated in our follow up study.

5.2 The radial dependences of the radiation belt electrons

The responses of radiation belt electrons to V_{sw}, n_{sw}, P_{dyn}, AL, and SYM-H have radial dependence. The data coverage for the electrons with μ = 725–875 MeV G^{-1} and K = 0.09–0.13 $R_E\ G^{-0.5}$ is poor for L* < 3 and L* > 6.5. Hence, the present study does not consider these L* ranges. The effect of n_{sw} and P_{dyn} on the radiation belt electron PSD appear to be significant only at L* = 4.5–6 and insignificant at L* = 3–4.5. This suggests that the magnetopause shadowing is effective mostly at L* = 4.5–6. At L* = 6–6.5, there is a high variability in PSD and the bin has the fewest number of points (n = 336) and hence the result is deemed unreliable. In contrast, the effect of V_{sw} on the electron PSD appears to be significant at a larger range of L*, L* = 3.5 to 6.5.

An increase in n_{sw} or P_{dyn} compresses the magnetosphere leading to the electron loss at high L*, e.g., L* > 7. However, ULF waves generated throughout the magnetosphere due to the compression would redistribute the loss to lower L*. Our result shows that the electron loss can be seen at L* = 4.5–6, consistent with understanding from observations and simulations (*Turner et al*. 2012, 2014a; *Xiang et al*. 2017; 2018; *Turner and Ukhorskiy*, 2020). At higher L*, the noise in the CMI($n_{sw} \rightarrow$ PSD$|\ V_{sw}$) is higher, which can be attributed to higher variability of the PSD. For example, the PSD initially decreases due to the magnetopause compression and then increase because of the outward diffusion (*Turner et al*., 2012; *Shprits et al*., 2006). Our result differs from Zhao et al. (2017) that found that P_{dyn} negatively correlates with PSD only at a small range of L* band near 6 (see their Figure 4c).

The radiation belt electrons also have strong dependences on the internal state of the magnetosphere. In the present study, this is explored and exemplified with AL and SYM-H, which can be used as proxies for magnetospheric state. However, the dependences on AL and SYM-H vary with radial distance or L*. The dependence of the radiation belt electrons on AL is significant at L* = 4–6 while the dependence on SYM-H is significant at L* = 3–6. The response of the

514 radiation belt electrons to AL and SYM-H peak at τ = 40–80 and τ = 20–60 hr, respectively. These
515 lag times are averaged for all L*, but the smaller τ for SYM-H can also be seen when the data are
516 binned by L* = 0.5 (Figures 11 and 13). This difference in response lag times are also seen in the
517 corr(AL $\rightarrow$ PSD) and corr(SYM-H $\rightarrow$ PSD) in Zhao et al. (2017), but their peak τ are smaller,
518 which may be attributed, at least partly, to their usage of daily resolution data and their correlations
519 did not remove the effect of V_{sw}. The responses to AL and SYM-H are discussed further in Section
520 5.3.
521
522 **5.3 Implications to electron acceleration mechanism and transport**
523 One of the fundamental questions in radiation belt physics is how the electrons are
524 accelerated to relativistic energies (> 1 MeV). There have been many proposed mechanisms, but
525 most tend to fall into two categories: (1) local acceleration and (2) radial transport (see review in
526 Friedel et al., 2002).
527 In the local acceleration mechanism, substorms or storms transport low energy electrons (a
528 few to tens of keVs) from the plasma sheet into the inner magnetosphere, which are often referred
529 to as the source population (e.g,, *Baker et al*., 1996; *Tang et al.*, 2017; *Boyd et al*., 2016). The
530 temperature anisotropy in the source population leads to the growth of the VLF whistler mode
531 chorus waves (e.g., *Meredith et al*., 2001; *W. Li et al*., 2009). Substorms and storms also transport
532 high energy electrons (a few tens to hundreds keVs) electrons from the plasma sheet into the inner
533 magnetosphere, which are commonly referred to as seed population. Then, the chorus waves
534 interact with the seed electrons and energize them to relativistic energies (e.g., *Summers et al*.,
535 1998; 2002; *Horne et al*., 2005; Thorne, 2010; Reeves et al., 2013; *W. Li et al.*, 2014).
536 In the radial transport acceleration mechanism, electrons at larger L* get accelerated as

they move inward to the inner magnetosphere through interactions with ULF waves (e.g., *Baker et al*., 1998; *Li and Temerin*, 2001; *Li et al*., 2005; *Ukhorskiy et al*., 2005; *Mathie and Mann*, 2000; *Elkington et al*., 1999; *Kepko and Viall*, 2019). These ULF waves can be associated with high V_{sw} and Kelvin-Helmholtz Instability (KHI) or n_{sw} or P_{dyn} fluctuations (e.g., *Johnson et al*., 2014; *Engebretson et al.*, 1998; *Vennerstrøm*, 1999; *Claudepierre et al*., 2010; *Takahashi and Ukhorskiy*, 2007; *Liu et al*., 2010).

The result of CMI($V_{sw} \rightarrow$ PSD$|\, n_{sw}$) as a function of L* (Figures 8 and 9) can be interpreted in terms of local acceleration mechanism. Figure 9 shows that the radiation belt electrons at L* = 4.5–5.5 have the shortest response lag time with peak τ = 35–50 hr and the highest significance. The response lag time is larger and broader at higher L*, τ = 45–65 hr (L* = 5.5–6), τ = 40–100 hr (L* = 6–6.5), and at lower L*, τ = 35–55 hr (L* = 4–4.5) and τ = 45–60 hr (L* = 3.5–4). This would suggest that local acceleration peaks at L* = 4.5–5.5 and the shifting of the peak to a larger τ at higher or lower L* suggests outward or inward diffusion, respectively.

Previous studies also found evidence for local acceleration at this L* band by examining the MeV PSD or electron fluxes as a function of radial distance (*Green and Kivelson*, 2004) or microburst MeV electron precipitation (*O'Brien et al*., 2003). More recently, in the RBSP era, Tang et al. (2017) found evidence of local acceleration of 1 MeV electrons at L ~ 4–5 in 74 storm events. *Boyd et al*. (2018) found the peak PSD is located mostly at L* = 4.5 – 5.5 in 80 storm events. They concluded that 70 out of 80 events show evidence of local acceleration based on the PSD vs. L* spectra.

However, there is also evidence that suggests localized acceleration in tandem with outward or inward diffusion originating from L* = 4.5–5.5 (e.g., Allison and Shprits, 2020). For example, at L* = 4–4.5, one can see that the i_{tr} starts increasing at τ = 25 hr, very much about the

same time i_{tr} increases at L* = 4.5–5.5 hr, but the significance is lower (Figure 8). This may suggest that the whistler mode chorus waves are also present at L* = 4–4.5 and not all 1–2 MeV electrons are transported from L* = 4.5–5.5. The same dynamics can be seen at the outermost L*, L* = 6–6.5.

The radial diffusion time scale can be estimated from the peak τ at each L* band. In Figure 9, the peak τ increases from ~ 40 hr at L* = 4.5–5.5 to ~60 hr at L* = 5.5–6, suggesting outward diffusion time scale of 40 hr per R_E. The diffusion time scale of 40 hr (or about 2 days) per R_E can be compared with the theoretical estimate of 1–6 days that is attributed to ULF waves at L* = 6 (e.g., *Elkington et al*., 2003).

Although the present study does not rule out the ULF waves and radial transport as the acceleration source and such mechanism is certainly operational in some or many cases, the local acceleration signature appears to be dominant statistically.

Our interpretation of local acceleration and time scale based on the information theoretic analysis of the observations can be complemented and strengthened with physics-based modeling (e.g., *Shprits et al*. 2009; *Reeves et al.*, 2012; *Horne et al*., 2013; *Camporeale et al.*, 2013; 2016). It would be interesting to analyze the simulation data using CMI in a similar manner done in the present study.

The result of CMI(AL $\rightarrow$ PSD| V_{sw}) can also be interpreted as consistent with local acceleration at L* = 4–5.5 and inward and outward diffusion to lower and higher L*, respectively. This may not be too surprising because the link between V_{sw} and PSD involves substorm injections.

Iles et al. (2006) examined a substorm event and found that peak PSD for electrons > 0.8 MeV is located at L* = 4.3–5.5, which is close to the L* band with the largest CMI significance, L* = 4.5–5.5. They also found evidence of local acceleration and radial diffusion.

583 The radiation belt electron response lag time appears more complicated for CMI(SYM-H
584 $\rightarrow$ PSD| V_{sw}) (Figure 13). The peak τ is most significant and smallest at L* = 5–5.5 suggesting
585 local acceleration peaks at this L* band. There is evidence for inward and outward diffusion from
586 this L* band. However, there is also evidence for local acceleration at smaller L*. The
587 complication may stem from the competing processes that would increase and decrease PSD and
588 electron fluxes. A decrease of SYM-H would indicate increase in the ring current and the intensity
589 of storms. The general response to storm plasma injections would be an increase in whistler mode
590 chorus waves and electron acceleration, leading to an increase in PSD. However, storm would
591 increase the ring current, which would reduce |B|. This would cause outward diffusion and
592 reduction of PSD as the electrons would attempt to conserve the third adiabatic invariant (*Turner*
593 *et al.*, 2012). This D_{st} or SYM-H effect would be stronger with increasing radial distance because
594 magnetospheric |B| decreases with r^{-3}. This could be a contributing factor in the high noise and
595 variability seen in L* = 6-6.5. Studies have shown that the radiation belt electron response at the
596 outermost L* band can sometimes be enhancement, depletion, or no change (*O'Brien et al*., 2001;
597 *Reeves et al*., 2003). These competing processes may contribute to this variability in the radiation
598 belt response. Also, different types of storms would affect different L* differently. For example,
599 *Turner et al* (2019) reported that full coronal mass ejection (CME) storms cause MeV electron
600 enhancements at L < ~5 while stream interaction region (SIR) storms cause enhancements at L >
601 ~4.5. CME sheaths and CME ejecta can cause depletions throughout the outer radiation belt.
602 Comparisons of Figures 11 and 13 show that response lag time (τ) for SYM-H (Figure 13)
603 is smaller than that for AL by about 9–10 hr (Figure 11). Our interpretation is that in both cases
604 particle injections lead to local accelerations. During storm time, on average, the peak of the main
605 phase (minimum SYM-H) is reached about 9 hr after the start of the main phase (start of particle

injection) (Yokoyama and Kamide, 1997; Fok et al., 2011). On the other hand, AL is a proxy for the auroral electrojets and their peak enhancement (minimum AL) can be reached fairly quickly from the time of substorm injections, within minutes. Thus, the smaller response time scale seen for SYM-H (Figure 13) may be attributed to the relative time scale for electron acceleration to MeV energy range and SYM-H reaching its minimum from the start of particle injection. As mentioned above, it would be useful to confirm this with a physics-based modeling study (e.g., *Shprits et al*. 2009; *Reeves et al.*, 2012; *Horne et al*., 2013; *Camporeale et al.*, 2013; 2016)

5.4 Ranking of the solar wind and magnetospheric drivers

We rank the solar wind and magnetospheric parameters based on the information transfer to the radiation belt electron PSD. This ranking can be useful for modelers who would like to develop models that input solar wind and magnetospheric parameters and predict radiation belt electrons having energies 1–2 MeV. This is shown in Table 1. The table shows that V_{sw} transfers the most information to the radiation belt electrons and hence should be considered an important, if not the most important, input parameter to radiation belt models. However, SYM-H can also be an important input parameter for models for two reasons: (1) SYM-H transfers the second most information to the radiation belt electrons; and (2) Out of a long list of parameters (V_{sw}, n_{sw}, P_{dyn}, AL, SYM-H), only SYM-H has information the radiation belt electrons at L* = 3–3.5 albeit only a small amount of information. SYM-H can play a crucial role for models that predict the radiation belt electrons at L* = 3–3.5.

6. Summary

The following summarizes the main results of our study.

- CMI can be a powerful tool to untangle the effect of solar wind and magnetospheric drivers of the radiation belt electrons.
- Pearson correlations give lag times that are different than those obtained using CMI that removes the effect of another driver. Table 2 shows some of the comparisons. For example, CMI($n_{sw} \rightarrow$ PSD$|\, V_{sw}$) peaks at τ = 7-11 hr, whereas |corr($n_{sw} \rightarrow$ PSD)| peaks at τ = 15 hr. The smaller response lag time of 7-11 hr physically makes more sense because the magnetopause shadowing process should be quick.
- There is a long-range positive correlation between nsw and PSD at τ = 80–120 hr.
- The magnetopause shadowing effect is only significant at L* = 4.5-6.
- The effect of Vsw is significant at L* = 3.5–6.5.
- The analysis of Vsw, AL, and SYM-H as a function of L* can be interpreted in terms of local acceleration and subsequent inward and outward diffusion.
- Table 1 ranks solar wind and magnetospheric parameters based on information transfer to the radiation belt electron PSD.

Acknowledgments. The solar wind, SYM-H, and AL dataset were obtained from NASA OMNIweb https://omniweb.gsfc.nasa.gov/. All RBSP-ECT data are publicly available at the website http://www.rbsp-ect.lanl.gov. All the derived data products in this paper are publicly available at the Zenodo Archive (Wing, 2021). Simon Wing acknowledges support of NASA Van Allen Probe Contract NNN16AA09T and NASA Grants NNX16AQ87G, 80NSSC20K0704, 80NSSC19K0843, 80NSSC19K0822, 80NSSC20K0188, 80NSSC20K1279, and

80NSSC20K1271. Drew Turner is thankful for funding from NASA grants 80NSSC19K0280 and 80NSSC18K1377. This work has benefitted from discussions within the International Space Science Institute (ISSI) Team # 455 “Complex Systems Perspectives Pertaining to the Research of the Near-Earth Electromagnetic Environment.”

References

Allison, H.J., Shprits, Y. Y. (2020), Local heating of radiation belt electrons to ultra-relativistic energies. *Nat Commun* **11,** 4533, https://doi.org/10.1038/s41467-020-18053-z

Baker, D. N., R. L. McPherron, T. E. Cayton, and R. W. Klebesadel (1990), Linear prediction filter analysis of relativistic electron properties at 6.6 R_E , J. Geophys. Res., 95(A9),15133–15140, doi:10.1029/JA095iA09p15133.

Baker, D. N., Pulkkinen, T. I., Angelopoulos, V., Baumjohann, W., and McPherron, R. L. (1996), Neutral line model of substorms: Past results and present view, *J. Geophys. Res.*, 101(A6), 12975– 13010, doi:10.1029/95JA03753.

Baker, D. N., X Li, J. B Blake, S. Kanekal (1998), Strong electron acceleration in the Earth's magnetosphere, Adv. Space Res., 21, 609-613, doi:10.1016/S0273-1177(97)00970-8.

Baker, D. N., et al. (2012), The Relativistic Electron-Proton Telescope (REPT) Instrument on Board the Radiation Belt Storm Probes (RBSP) Spacecraft: Characterization of Earth's Radiation Belt High-Energy Particle Populations, Space Sci. Rev., doi:10.1007/s11214-012-9950-9.

Baker, D.N., Erickson, P.J., Fennell, J.F. *et al.* Space Weather Effects in the Earth's Radiation Belts. *Space Sci Rev* **214,** 17 (2018). https://doi.org/10.1007/s11214-017-0452-7

Baker, D. N., Hoxie, V., Zhao, H., Jaynes, A. N., Kanekal, S., Li, X., & Elkington, S. (2019a). Multiyear measurements of radiation belt electrons: Acceleration, transport, and loss. *Journal of Geophysical Research: Space Physics*, 124, 2588– 2602. https://doi.org/10.1029/2018JA026259

Baker, D. N., Zhao, H., Li, X., Kanekal, S. G., Jaynes, A. N., Kress, B. T., et al. (2019b). Comparison of Van Allen Probes Energetic Electron Data with corresponding GOES-15

Measurements: 2012–2018. Journal of Geophysical Research: Space Physics,124, https://doi.org/10.1029/2019JA027331

Balasis, G., Daglis, I. A., Papadimitriou, C., Kalimeri, M., Anastasiadis, A., and Eftaxias, K. (2009), Investigating dynamical complexity in the magnetosphere using various entropy measures, *J. Geophys. Res.*, 114, A00D06, doi:10.1029/2008JA014035.

Balasis, G.; Donner, R.V.; Potirakis, S.M.; Runge, J.; Papadimitriou, C.; Daglis, I.A.; Eftaxias, K.; Kurths (2013), J. Statistical mechanics and information-theoretic perspectives on complexity in the Earth system. Entropy, 15, 4844–4888, doi:10.3390/e15114844.

Balikhin, M. A., R. J. Boynton, S. A. Billings, M. Gedalin, N. Ganushkina, D. Coca, and H. Wei (2010), Data based quest for solar wind-magnetosphere coupling function, Geophys. Res. Lett., 37, L24107, doi:10.1029/2010GL045733.

Balikhin, M. A., R. J. Boynton, S. N. Walker, J. E. Borovsky, S. A. Billings, and H. L. Wei(2011), Using the NARMAX approach to model the evolution of energetic electrons fluxes at geostationary orbit, Geophys. Res. Lett., 38, L18105, doi:10.1029/2011GL048980.

Blake, J.B., Carranza, P.A., Claudepierre, S.G. *et al.* The *Magnetic Electron Ion Spectrometer* (MagEIS) Instruments Aboard the Radiation Belt Storm Probes (RBSP) Spacecraft. *Space Sci Rev* **179,** 383–421 (2013). https://doi.org/10.1007/s11214-013-9991-8

Borovsky, J. E. (2017). Time-integral correlations of multiple variables with the relativistic-electron flux at geosynchronous orbit: The strong roles of substorm-injected electrons and the ion plasma sheet. *Journal of Geophysical Research: Space Physics*, 122, 11,961– 11,990. https://doi.org/10.1002/2017JA024476

Borovsky, J. E. (2018), On the origins of the intercorrelations between solar wind variables. *Journal of Geophysical Research: Space Physics*, 123, 20– 29. https://doi.org/10.1002/2017JA024650

Borovsky, J. E. (2020), What magnetospheric and ionospheric researchers should know about the solar wind, *J. Atmos. Sol. Phys*., 204, 105271, https://doi.org/10.1016/j.jastp.2020.105271.

Boyd, A. J., Spence, H. E., Claudepierre, S. G., Fennell, J. F., Blake, J. B., Baker, D. N., Reeves, G. D., and Turner, D. L. (2014), Quantifying the radiation belt seed population in the March 17, 2013 electron acceleration event, *Geophys. Res. Lett.*, 41, 2275– 2281, doi:10.1002/2014GL059626.

Boyd, A. J., Spence, H. E., Huang, C.-L., Reeves, G. D., Baker, D. N., Turner, D. L., Claudepierre, S. G., Fennell, J. F., Blake, J. B., and Shprits, Y. Y. (2016), Statistical properties of the radiation belt seed population, *J. Geophys. Res. Space Physics*, 121, 7636– 7646, doi:10.1002/2016JA022652.

Boyd, A. J., Turner, D. L., Reeves, G. D., Spence, H. E., Baker, D. N., & Blake, J. B. (2018). What causes radiation belt enhancements: A survey of the Van Allen Probes Era. *Geophysical Research Letters*, 45, 5253– 5259. https://doi.org/10.1029/2018GL077699

Boyd, A. J., Spence, H. E., Reeves, G. D., Funsten, H. O., Skoug, R. M., Larsen, B. A., et al. (2021). RBSP-ECT combined pitch angle resolved electron flux data product. *Journal of Geophysical Research: Space Physics*, 126, e2020JA028637. https://doi.org/10.1029/2020JA028637

Camporeale, E., Delzanno, G. L., Zaharia, S., and Koller, J. (2013), On the numerical simulation of particle dynamics in the radiation belt: 1. Implicit and semi-implicit schemes, *J. Geophys. Res. Space Physics*, 118, 3463– 3475, doi:10.1002/jgra.50293.

Camporeale, E., Shprits, Y., Chandorkar, M., Drozdov, A., and Wing, S. (2016), On the propagation of uncertainties in radiation belt simulations, *Space Weather*, 14, 982– 992, doi:10.1002/2016SW001494

Claudepierre, S. G., M. K. Hudson, W. Lotko, J. G. Lyon, and R. E. Denton (2010), Solar wind driving of magnetospheric ULF waves: Field line resonances driven by dynamic pressure fluctuations, J. Geophys. Res., 115, A11202, doi:10.1029/2010JA015399.

Consolini, G., R. Tozzi, and P. De Michelis (2009), Complexity in the sunspot cycle, A&A 506, 1381–1391, DOI: 10.1051/0004-6361/200811074

Davis, T. N., and Sugiura, M. (1966), Auroral electrojet activity index *AE* and its universal time variations, *J. Geophys. Res.*, 71(3), 785– 801, doi:10.1029/JZ071i003p00785.

Darbellay, G. A., and I. Vajda (1999), Estimation of the Information by an Adaptive Partitioning of the Observations Space, IEEE Transactions on Information Theory, 45, 1315–1321.

Dessler, A., and E. Parker (1959), Hydromagnetic theory of geomagnetic storms, *J. Geophys. Res.*, **64**(12), 2239–2252, doi:10.1029/JZ064i012p02239.

Elkington, S. R., M. K. Hudson, and A. A. Chan (1999), Acceleration of relativistic electrons via drift-resonant interaction with toroidal-mode Pc-5 ULF oscillations, Geophys. Res. Lett., 26, 3273.

Elkington, S. R., Hudson, M. K., and Chan, A. A. (2003), Resonant acceleration and diffusion of outer zone electrons in an asymmetric geomagnetic field, *J. Geophys. Res.*, 108, 1116, doi:10.1029/2001JA009202

Engebretson, M., K.-H. Glassmeier, M. Stellmacher, W. J. Hughes, and H. Lühr (1998), The dependence of high-latitude PcS wave power on solar wind velocity and on the phase of

high-speed solar wind streams, J. Geophys. Res., 103(A11), 26271–26283, doi:10.1029/97JA03143.

Fok, M.-C., Moore, T. E., Slinker, S. P., Fedder, J. A., Delcourt, D. C., Nosé, M., and Chen, S.-H. (2011), Modeling the superstorm in November 2003, *J. Geophys. Res.*, 116, A00J17, doi:10.1029/2010JA015720.

Friedel, R. H. W., G. D. Reeves, and T. Obara (2002), Relativistic electron dy- namics in the inner magnetosphere—A review, J. Atmos. Sol. Terr. Phys., 64, 265.

Green, J. C., and M. G. Kivelson (2004), Relativistic electrons in the outer radiation belt: Differentiating between acceleration mechanisms, J. Geophys. Res., 109, A03213, doi:10.1029/2003JA010153.

Horne, R. B., R. M. Thorne, S. A. Glauert, J. M. Albert, N. P. Meredith, and R. R. Anderson (2005), Timescale for radiation belt electron acceleration by whistler mode chorus waves,J. Geophys. Res., 110, A03225, doi:10.1029/2004JA010811

Horne, R. B., Glauert, S. A., Meredith, N. P., Boscher, D., Maget, V., Heynderickx, D., and Pitchford, D. (2013), Space weather impacts on satellites and forecasting the Earth's electron radiation belts with SPACECAST, *Space Weather*, 11, 169– 186, doi:10.1002/swe.20023.

Iles, R. H. A., Meredith, N. P., Fazakerley, A. N., and Horne, R. B. (2006), Phase space density analysis of the outer radiation belt energetic electron dynamics, *J. Geophys. Res.*, 111, A03204, doi:10.1029/2005JA011206.

Iyemori, T. (1990), Storm-time magnetospheric currents inferred from mid-latitude geomagnetic field variations, J. Geomag. Geoelectr., 42, 1249–1265.

770 Johnson, J. R., and S. Wing (2005), A solar cycle dependence of nonlinearity in magnetospheric
771 activity, J. Geophys. Res., 110, A04211, doi:10.1029/2004JA010638.
772 Johnson, J. R., and S. Wing (2014), External versus internal triggering of substorms: An
773 information-theoretical approach, Geophys. Res. Lett., 41, 5748–5754,
774 doi:10.1002/2014GL060928.
775 Johnson, J. R., S. Wing, and P. A. Delamere (2014), Kelvin Helmholtz Instability in Planetary
776 Magnetospheres, Space Sci. Rev., 184, 1 – 31, doi:10.1007/s11214-014-0085-z.
777 Johnson, J. R., Wing, S., and Camporeale, E. (2018), Transfer entropy and cumulant-based cost as
778 measures of nonlinear causal relationships in space plasmas: applications to D_{st}, Ann.
779 Geophys., 36, 945-952, https://doi.org/10.5194/angeo-36-945-2018
780 Katus, R. M., Liemohn, M. W., Gallagher, D. L., Ridley, A., and Zou, S. (2013), Evidence for
781 potential and inductive convection during intense geomagnetic events using normalized
782 superposed epoch analysis, *J. Geophys. Res. Space Physics*, 118, 181– 191,
783 doi:10.1029/2012JA017915.
784 Kellerman, A. C., and Y. Y. Shprits (2012), On the influence of solar wind conditions on the outer-
785 electron radiation belt, J. Geophys. Res., 117, A05217, doi:10.1029/2011JA017253.
786 Kepko, L., & Viall, N. M. (2019). The source, significance, and magnetospheric impact of periodic
787 density structures within stream interaction regions. Journal of Geophysical Research: Space
788 Physics, 124, 7722– 7743. https://doi.org/10.1029/2019JA026962
789 Lejosne, S., Kollmann, P. Radiation Belt Radial Diffusion at Earth and Beyond. *Space Sci*
790 *Rev* **216,** 19 (2020). https://doi.org/10.1007/s11214-020-0642-6
791 Li, W. (1990), Mutual Information Functions Versus Correlation Functions, J. Stat. Phys., 60, 823–
792 837.

Li, W., Thorne, R. M., Angelopoulos, V., Bonnell, J. W., McFadden, J. P., Carlson, C. W., LeContel, O., Roux, A., Glassmeier, K. H., and Auster, H. U. (2009), Evaluation of whistler-mode chorus intensification on the nightside during an injection event observed on the THEMIS spacecraft, *J. Geophys. Res.*, 114, A00C14, doi:10.1029/2008JA013554.

Li, W., et al. (2014), Radiation belt electron acceleration by chorus waves during the 17 March 2013 storm, *J. Geophys. Res. Space Physics*, 119, 4681– 4693, doi:10.1002/2014JA019945.

Li, X., and M. A. Temerin (2001), The electron radiation belt, Space Sci. Rev., 95, 569 - 580.

Li, X., M. Temerin, D. Baker, G. Reeves, and D. Larson (2001), Quantitative prediction of radiation belt electrons at geostationary orbit based on solar wind measurements,*Geophys. Res. Lett.*, **28**(9), 1887–1890.

Li, X., D. N. Baker, M. Temerin, G. Reeves, R. Friedel, and C. Shen (2005), Energetic electrons, 50 keV to 6 MeV, at geosynchronous orbit: Their responses to solar wind variations, Space Weather, 3, S04001, doi:10.1029/2004SW000105.

Li, X., Barker, A. B., Baker, D. N., Tu, W. C., Sarris, T. E., Selesnick, R. S., Friedel, R., and Shen, C. (2009), Modeling the deep penetration of outer belt electrons during the "Halloween" magnetic storm in 2003, *Space Weather*, 7, S02004, doi:10.1029/2008SW000418.

Liu, W., Sarris, T. E., Li, X., Ergun, R., Angelopoulos, V., Bonnell, J., and Glassmeier, K. H. (2010), Solar wind influence on Pc4 and Pc5 ULF wave activity in the inner magnetosphere, *J. Geophys. Res.*, 115, A12201, doi:10.1029/2010JA015299.

Lyatsky, W., and G. V. Khazanov (2008), Effect of solar wind density on relativistic electrons at geosynchronous orbit, Geophys. Res. Lett., 35, L03109, doi:10.1029/2007GL032524.

Maggiolo, R., Hamrin, M., De Keyser, J., Pitkänen, T., Cessateur, G., Gunell, H., & Maes, L. (2017). The delayed time response of geomagnetic activity to the solar wind. Journal of

816 Geophysical Research: Space Physics, 122, 11,109– 11,127.
817 https://doi.org/10.1002/2016JA023793
818 March, T. K., Chapman, S. C., and Dendy, R. O. (2005), Mutual information between
819 geomagnetic indices and the solar wind as seen by WIND: Implications for propagation time
820 estimates, *Geophys. Res. Lett.*, 32, L04101, doi:10.1029/2004GL021677.
821 Mathie, R. A., & Mann, I. R. (2000). A correlation between extended intervals of ULF wave power
822 and stormtime geosynchronous relativistic electron flux enhancements. Geophysical
823 Research Letters, 27(20), 3261–3264. https://doi.org/10.1029/2000gl003822
824 Manshour,P., Balasis,G.; Consolini, G.; Papadimitriou, C., Paluš, M. (2021), Causality and
825 Information Transfer Between the Solar Wind and the Magnetosphere–Ionosphere System.
826 *Entropy*, *23*, 390. https://doi.org/10.3390/e23040390
827 Mathie, R. A., and I. R. Mann (2000), A correlation between extended intervals of ULF wave
828 power and storm-time geosynchronous relativistic electron flux enhancements, *Geophys.*
829 *Res. Lett.*, **27**, 3621–3264, doi:10.1029/2000GL003822.
830 Mathie, R. A., and I. R. Mann (2001), On the solar wind control of Pc5 ULF pulsation power at
831 mid-latitudes: Implications for MeV electron acceleration in the outer radiation belt, J.
832 Geophys. Res., 106(A12), 29783–29796, doi:10.1029/2001JA000002.
833 Mauk, B. H., N. J. Fox, S. G. Kanekal, R. L. Kessel, D. G. Sibeck, and A. Ukhorskiy (2013),
834 Science objectives and rationale for the radiation belt storm probes mission, Space Science
835 Review, *179*(1-4), 3–27, doi:10.1007/s11214-012-9908-y.
836 Meredith, N. P., Horne, R. B., and Anderson, R. R. (2001), Substorm dependence of chorus
837 amplitudes: Implications for the acceleration of electrons to relativistic energies, *J. Geophys.*
838 *Res.*, 106(A7), 13165– 13178, doi:10.1029/2000JA900156.

O'Brien, T. P., McPherron, R. L., Sornette, D., Reeves, G. D., Friedel, R., and Singer, H. J. (2001), Which magnetic storms produce relativistic electrons at geosynchronous orbit?, *J. Geophys. Res.*, 106(A8), 15533– 15544, doi:10.1029/2001JA000052.

O'Brien, T. P., Lorentzen, K. R., Mann, I. R., Meredith, N. P., Blake, J. B., Fennell, J. F., Looper, M. D., Milling, D. K., and Anderson, R. R. (2003), Energization of relativistic electrons in the presence of ULF power and MeV microbursts: Evidence for dual ULF and VLF acceleration, J. Geophys. Res., 108, 1329, doi:10.1029/2002JA009784, A8.

Papadimitriou, Constantinos; Balasis, Georgios; Boutsi, Adamantia Z.; Daglis, Ioannis A.; Giannakis, Omiros; Anastasiadis, Anastasios; Michelis, Paola D.; Consolini, Giuseppe. (2020), Dynamical Complexity of the 2015 St. Patrick's Day Magnetic Storm at Swarm Altitudes Using Entropy Measures, *Entropy*, 22, 5, 574, https://doi.org/10.3390/e22050574

Paulikas, G. A., and J. B. Blake (1979), Effects of the solar wind on magnetospheric dynamics: Energetic electrons at the synchronous orbit, in *Quantitative Modeling of Magnetospheric Processes*, *Geophys. Monogr. Ser.*, Vol 21, pp. 180-202, AGU, Washington D.C.

Pinto, V. A., Kim, H.-J., Lyons, L. R., & Bortnik, J. (2018). Interplanetary parameters leading to relativistic electron enhancement and persistent depletion events at geosynchronous orbit and potential for prediction. *Journal of Geophysical Research: Space Physics*, 123, 1134– 1145. https://doi.org/10.1002/2017JA024902

Prichard, D., and J. Theiler (1995), Generalized redundancies for time series analysis, *Physica D: Non-linear Phenomena,* 84, 476–493, doi:10.1016/0167-2789(95)00041-2.

Reeves, G. D. (1998), Relativistic electrons and magnetic storms: 1992–1995, Geophys. Res. Lett., 25, 1817–1820, doi:10.1029/98GL01398.

Reeves, G. D., McAdams, K. L., Friedel, R. H. W., and O'Brien, T. P. (2003), Acceleration and

loss of relativistic electrons during geomagnetic storms, *Geophys. Res. Lett.*, 30, 1529, doi:10.1029/2002GL016513

Reeves, G. D., S. K. Morley, R. H. W. Friedel, M. G. Henderson, T. E. Cayton, G. Cunningham, J. B. Blake, R. A. Christensen, and D. Thomsen (2011), On the relationship between relativistic electron flux and solar wind velocity: Paulikas and Blake revisited, J. Geophys. Res., 116, A02213, doi:10.1029/2010JA015735.

Reeves, G. D., Chen, Y., Cunningham, G. S., Friedel, R. W. H., Henderson, M. G., Jordanova, V. K., Koller, J., Morley, S. K., Thomsen, M. F., and Zaharia, S. (2012), Dynamic Radiation Environment Assimilation Model: DREAM, *Space Weather*, 10, S03006, doi:10.1029/2011SW000729

Reeves, G., S. Morley, and G. Cunningham (2013), Long-term variations in solar wind velocity and radiation belt electrons, J. Geophys. Res. Space Physics, 118, 1040–1048, doi:10.1002/jgra.50126.

Rigler, E. J., M. Wiltberger, and D. N. Baker (2007), Radiation belt electrons respond to multiple solar wind inputs, J. Geophys. Res., 112, A06208, doi:10.1029/2006JA012181

Roederer, J. G. (1970), Dynamics of Geomagnetically Trapped Radiation, Springer, New York, https://doi.org/ 10.1007/978-3-642-49300-3

Runge, J., Balasis, G., Daglis, I.A. *et al.* Common solar wind drivers behind magnetic storm–magnetospheric substorm dependency. *Sci Rep* **8,** 16987 (2018). https://doi.org/10.1038/s41598-018-35250-5

Schulz, M., and L.J. Lanzerotti (1974) , Particle Diffusion in the Radiation Belts, Springer, Berlin, 1974, https:// doi.org/10.1007/978-3-642-65675-0

Simms, L. E., V. Pilipenko, M. J. Engebretson, G. D. Reeves, A. J. Smith, and M.

885 Clilverd (2014),Prediction of relativistic electron flux at geostationary orbit following
886 storms: Multiple regression analysis, J. Geophys. Res. Space Physics, 119, 7297–7318,
887 doi:10.1002/2014JA019955.
888 Shprits, Y. Y., R. M. Thorne, R. Friedel, G. D. Reeves, J. Fennell, D. N. Baker, and S. G.
889 Kanekal (2006), Outward radial diffusion driven by losses at magnetopause, J. Geophys.
890 Res., 111, A11214, doi:10.1029/2006JA011657
891 Shprits, Y. Y., D. A. Subbotin, N. P. Meredith, S. R. Elkington (2008), Review of modeling of
892 losses and sources of relativistic electrons in the outer radiation belt II: Local acceleration
893 and loss, J. Atmos. Sol. Terr. Phys., 70, 1694-1713, doi:10.1016/j.jastp.2008.06.014.
894 Shprits, Y. Y., D. Subbotin, and B. Ni (2009), Evolution of electron fluxes in the outer radiation
895 belt computed with the VERB code, J. Geophys. Res., 114, A11209,
896 doi:10.1029/2008JA013784.
897 Smirnov, A. G., Berrendorf, M., Shprits, Y. Y., Kronberg, E. A., Allison, H. J., Aseev, N. A., et
898 al. (2020). Medium energy electron flux in earth's outer radiation belt (MERLIN): A
899 machine learning model. *Space Weather*, 18,
900 e2020SW002532. https://doi.org/10.1029/2020SW002532
901 Snelling, Jesse M., Jay R. Johnson, Jake Willard, Yosia Nurhan, Jonathan Homan, and Simon
902 Wing (2020), Information Theoretical Approach to Understanding Flare Waiting Times, The
903 Astrophysical Journal, 899, 148, http://dx.doi.org/10.3847/1538-4357/aba7b9
904 Spence, H.E., Reeves, G.D., Baker, D.N. et al. (2013), Science Goals and Overview of the
905 Radiation Belt Storm Probes (RBSP) Energetic Particle, Composition, and Thermal Plasma
906 (ECT) Suite on NASA's Van Allen Probes Mission. Space Sci Rev 179, 311–336,
907 https://doi.org/10.1007/s11214-013-0007-5
908 Stumpo, Mirko; Consolini, Giuseppe; Alberti, Tommaso; Quattrociocchi, Virgilio. 2020.
909 "Measuring Information Coupling between the Solar Wind and the Magnetosphere–
910 Ionosphere System" *Entropy* 22, no. 3: 276. https://doi.org/10.3390/e22030276

911 Summers, D., R. M. Thorne, and F. Xiao (1998), Relativistic theory of wave-particle resonant
912 diffusion with application to electron acceleration in the magnetosphere, J. Geophys.
913 Res., 103(A9), 20487–20500, doi:10.1029/98JA01740.
914 Summers, D., Ma, C., Meredith, N. P., Horne, R. B., Thorne, R. M., Heynderickx, D.,
915 and Anderson, R. R. (2002), Model of the energization of outer-zone electrons by whistler-
916 mode chorus during the October 9, 1990 geomagnetic storm, *Geophys. Res. Lett.*, 29(24),
917 2174, doi:10.1029/2002GL016039.
918 Summers, D., B. Ni, and N. P. Meredith (2007), Timescales for radiation belt electron acceleration
919 and loss due to resonant wave-particle interactions: 1. Theory, J. Geophys. Res., 112,
920 A04206, doi:10.1029/2006JA011801.
921 Tang, C. L., Wang, Y. X., Ni, B., Zhang, J.-C., Reeves, G. D., Su, Z. P., Baker, D. N., Spence, H.
922 E., Funsten, H. O., and Blake, J. B. (2017a), Radiation belt seed population and its
923 association with the relativistic electron dynamics: A statistical study, *J. Geophys. Res.*
924 *Space Physics*, 122, 5261– 5276, doi:10.1002/2017JA023905.
925 Takahashi, K., and Ukhorskiy, A. Y. (2007), Solar wind control of Pc5 pulsation power at
926 geosynchronous orbit, *J. Geophys. Res.*, 112, A11205, doi:10.1029/2007JA012483.
927 Thorne, R. M. (2010), Radiation belt dynamics: The importance of wave-particle
928 interactions,Geophys. Res. Lett., 37, L22107, doi:10.1029/2010GL044990
929 Thorne, R. M., et al. (2013), Rapid local acceleration of relativistic radiation-belt electrons by
930 magnetospheric chorus, Nature, 504(7480), 411–414, doi:10.1038/nature12889.
931 Tsonis, A. A. (2001), Probing the linearity and nonlinearity in the transitions of the atmospheric
932 circulation, Nonlinear Processes in Geophysics, 8, 341–345.
933 Tsyganenko, N. A., and Sitnov, M. I. (2005), Modeling the dynamics of the inner magnetosphere
934 during strong geomagnetic storms, *J. Geophys. Res.*, 110, A03208,
935 doi:10.1029/2004JA010798
936 Turner, D. L., and Li, X. (2008), Quantitative forecast of relativistic electron flux at
937 geosynchronous orbit based on low-energy electron flux, Space Weather, 6, S05005,
938 doi:10.1029/2007SW000354.
939 Turner, D. L., and X. Li (2011), Using spacecraft measurements ahead of Earth in the Parker spiral

to improve terrestrial space weather forecasts, Space Weather, 9, S01002, doi:10.1029/2010SW000627

Turner, D. L., Y. Shprits, M. Hartinger, and V. Angelopoulos (2012), Explaining sudden losses of outer radiation belt electrons during geomagnetic storms, Nat. Phys., 8, 208–212, doi:10.1038/nphys2185.

Turner, D. L., et al. (2014a), On the cause and extent of outer radiation belt losses during the 30 September 2012 dropout event, *J. Geophys. Res. Space Physics*, 119, 1530– 1540, doi:10.1002/2013JA019446.

Turner, D. L., et al. (2014b), Competing source and loss mechanisms due to wave-particle interactions in Earth's outer radiation belt during the 30 September to 3 October 2012 geomagnetic storm, *J. Geophys. Res. Space Physics*, 119, 1960– 1979, doi:10.1002/2014JA019770.

Turner, D. L., Kilpua, E. K. J., Hietala, H., Claudepierre, S. G., O'Brien, T. P., Fennell, J. F., et al. (2019). The response of Earth's electron radiation belts to geomagnetic storms: Statistics from the Van Allen Probes era including effects from different storm drivers. Journal of Geophysical Research: Space Physics, 124, 1013– 1034. https://doi.org/10.1029/2018JA026066

Turner, D. L., and A. Y. Ukhorskiy (2020), Chapter 1 - Outer radiation belt losses by magnetopause incursions and outward radial transport: new insight and outstanding questions from the Van Allen Probes era**,** in The dynamic loss of Earth's radiation belts eds. Allison N. Jaynes and Maria E. Usanova, Elsevier (2020), pp. 1–20, ISBN 9780128133712, https://doi.org/10.1016/B978-0-12-813371-2.00001-9

Ukhorskiy, A. Y., K. Takahashi, B. J. Anderson, and H. Korth (2005), Impact of toroidal ULF

963 waves on the outer radiation belt electrons, J. Geophys. Res., 110, A10202,
964 doi:10.1029/2005JA011017.
965 Ukhorskiy, A. Y., B. J. Anderson, P. C. Brandt, and N. A. Tsyganenko (2006), Storm time
966 evolution of the outer radiation belt: Transport and losses, J. Geophys. Res., 111, A11S03,
967 doi:10.1029/2006JA011690.
968 Vassiliadis, D., S. F. Fung, and A. J. Klimas (2005), Solar, interplanetary, and magnetospheric
969 parameters for the radiation belt energetic electron flux, J. Geophys. Res., 110, A04201,
970 doi:10.1029/2004JA010443.
971 Vennerstrøm, S. (1999), Dayside magnetic ULF power at high latitudes: A possible long-term
972 proxy for the solar wind velocity?, J. Geophys. Res., 104(A5), 10145–10157,
973 doi:10.1029/1999JA900015.
974 Wing, S., Johnson, J. R., Jen, J., Meng, C.-I., Sibeck, D. G., Bechtold, K., Freeman, J., Costello,
975 K., Balikhin, M., and Takahashi, K. (2005), Kp forecast models, *J. Geophys. Res.*, 110,
976 A04203, doi:10.1029/2004JA010500.
977 Wing, S., J. R. Johnson, C. C. Chaston, M. Echim, C. P. Escoubet, B. Lavraud, C. Lemon, K.
978 Nykyri, A. Otto, J. Raeder, and C.-P. Wang (2014), Review of solar wind entry into and
979 transport within the plasma sheet, Space Science Reviews, 184, 33 – 86,
980 doi:10.1007/s11214-014-0108-9
981 Wing, S., J. R. Johnson, E. Camporeale, and G. D. Reeves (2016), Information theoretical
982 approach to discovering solar wind drivers of the outer radiation belt, J. Geophys. Res. Space
983 Physics, 121, 9378–9399, doi:10.1002/2016JA022711
984 Wing, S., J. Johnson, and A. Vourlidas (2018), Information theoretic approach to discovering
985 causalities in the solar cycle, *Ap J*, **854,** 85, https://doi.org/10.3847/1538-4357/aaa8e7

Wing, S, J. R. Johnson (2019), Applications of Information Theory in Solar and Space Physics, *Entropy*, 21(2):140, https://doi.org/10.3390/e21020140

Wing, S., P. C. Brandt, D. G. Mitchell, J. R. Johnson, W. S. Kurth and J. D. Menietti (2020), Periodic Narrowband Radio Wave Emissions and Inward Plasma Transport at Saturn's Magnetosphere, Ap J, 159, 249, 10.3847/1538-3881/ab818d, https://doi.org/10.3847/1538-3881/ab818d

Wing, Simon (2021), Untangling the drivers of the radiation belt, Zenodo. https://doi.org/10.5281/zenodo.5153481.

Wyner, A. D. (1978), A definition of conditional mutual information for arbitrary ensembles, Info. and Control, 38, 51–59.

Xiang, Z., Tu, W., Li, X., Ni, B., Morley, S. K., & Baker, D. N. (2017). Understanding the mechanisms of radiation belt dropouts observed by Van Allen Probes. *Journal of Geophysical Research: Space Physics*, 122, 9858– 9879. https://doi.org/10.1002/2017JA024487

Xiang, Z., Tu, W., Ni, B., Henderson, M. G., & Cao, X. (2018). A statistical survey of radiation belt dropouts observed by Van Allen Probes. Geophysical Research Letters, 45. https://doi.org/10.1029/2018GL078907

Yokoyama, N., and Kamide, Y. (1997), Statistical nature of geomagnetic storms, *J. Geophys. Res.*, 102(A7), 14215– 14222, doi:10.1029/97JA00903

Zhao, H., Baker, D. N., Jaynes, A. N., Li, X., Elkington, S. R., Kanekal, S. G., Spence, H. E., Boyd, A. J., Huang, C.-L., and Forsyth, C. (2017), On the relation between radiation belt electrons and solar wind parameters/geomagnetic indices: Dependence on the first adiabatic invariant and L^*, *J. Geophys. Res. Space Physics*, 122, 1624– 1642,

1009 doi:10.1002/2016JA023658.

1010

1011

rank	solar wind and magnetospheric parameters	i_{tr_max}	peak τ (hour)
1	V_{sw}	0.12	46
2	SYM-H	0.030	20–60
3	AL	0.020	50–80
4	P_{dyn}[a]	0.018	7–11
5	IMF |B|[a]	0.018	50–110
6	IMF $B_z < 0$[a]	0.017	50–110
7	n_{sw}[a]	0.016	7–11
8	IMF B_y[a]	0.012	0–16
9	Esw	0.012	40–90
10	IMF $B_z > 0$	0.011	0–16
11	σ(IMF B)	0.0083	0–10

Table 1. Ranking of the the solar wind and magnetospheric parameters based on information transfer to radiation belt electron PSD. Parameters 2–11 are calculated from CMI($x \rightarrow$ PSD$|V_{sw}$) where x = IMF |B|, $B_z < 0$, $B_z > 0$, B_y, Esw, and σ(IMF B). Parameter 1 from CMI($V_{sw} \rightarrow$ PSD$|n_{sw}$). i_{tr_max} = peak CMI – mean noise where noise is calculated for surrogate data (see Section 4.1).

[a] the response has dual mode: at small τ (τ < 15 hr) the response is electron loss and at large τ (τ > 40 hr) the response is electron enhancement. The ranking is based on the larger i_{tr_max} of the two responses (see text for explanation).

Parameters	Correlation	Peak τ (hr)	Conditional Mutual Information (CMI)	Peak τ (hr)
V_{sw}	**corr(V_{sw} → PSD)**	**38**	**CMI(V_{sw} → PSD| n_{sw})**	**46**
n_{sw}	**corr(n_{sw} → PSD)**	**15**	**CMI(n_{sw} → PSD| V_{sw})**	**7**
AL	**corr(AL → PSD)**	**53**	**CMI(AL → PSD| V_{sw})**	**76**
SYM-H	**corr(SYM-H → PSD)**	**40**	**CMI(SYM-H → PSD| V_{sw})**	**55**

Table 2. Highlighting the differences between correlation and CMI. τ = is the radiation belt response lag time.

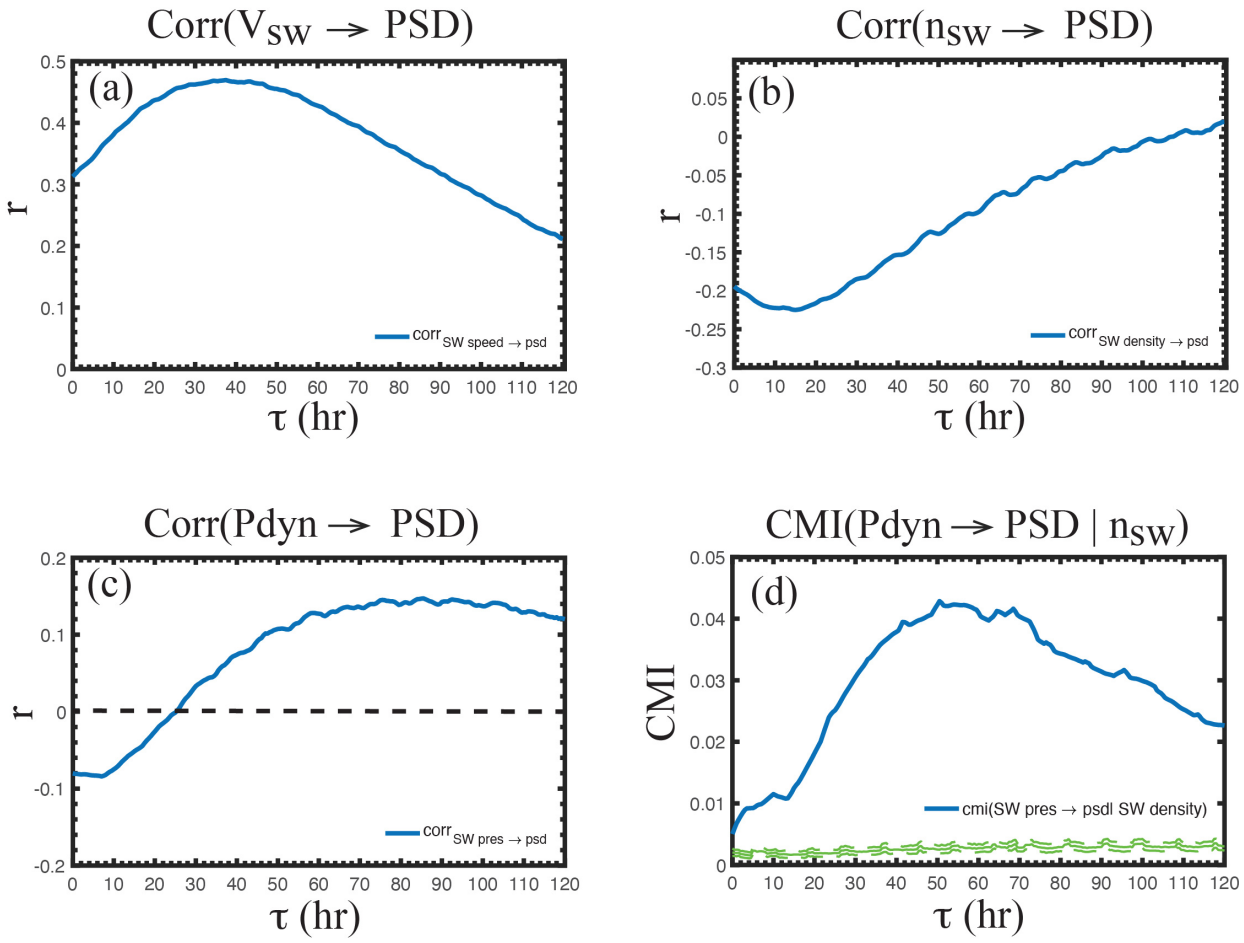

Figure 1. (a) V_{sw} positively correlates with radiation belt electron PSD. (b) n_{sw} negatively correlates with PSD. (c) The PSD response to solar wind dynamic pressure (P_{dyn}) has two modes: at small τ, P_{dyn} negatively correlates with PSD, similar to n_{sw} while at large τ, P_{dyn} positively correlates with PSD, similar to V_{sw}. (d) CMI(P_{dyn} → PSD| V_{sw}) is plotted as the blue curve. It shows that removing the effect of V_{sw}, the information transfer from P_{dyn} to PSD is similar to V_{sw} correlation with PSD, as expected. The mean noise and 3σ from the noise are plotted as solid and dashed green curves, respectively. The peak of the blue curve is 203σ above the mean noise and hence significant.

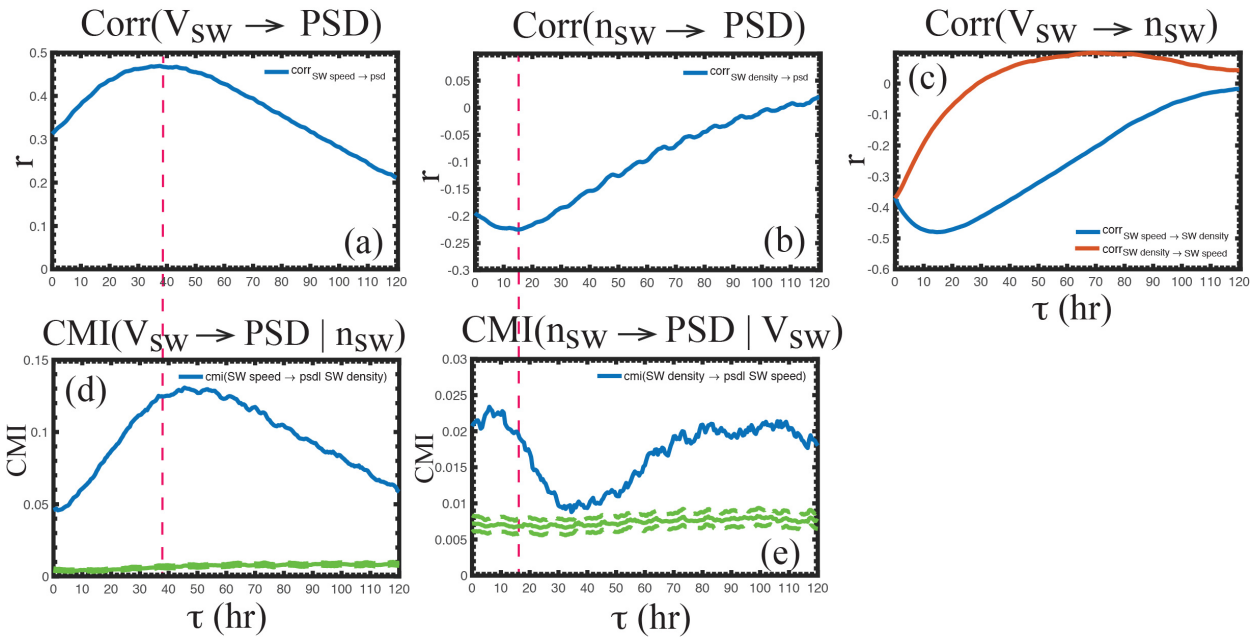

Figure 2. (a) V_{sw} positively correlates with PSD (same as Figure 1a). (b) n_{sw} negatively corelates with PSD (same as Figure 1b). (c) corr($V_{sw} \rightarrow n_{sw}$) = blue curve and corr($n_{sw} \rightarrow V_{sw}$) = red curve. The negative correlation between V_{sw} and n_{sw} raises the question that (a) or (b) may be coincidental. (d) CMI($V_{sw} \rightarrow$ PSD| n_{sw}) shows that (1) there is still information transfer from V_{sw} to PSD even after the effect of n_{sw} is removed and (2) removing the effect of n_{sw} shifts the peak of corr($V_{sw} \rightarrow$ PSD) to the right. (e) CMI($n_{sw} \rightarrow$ PSD| V_{sw}) shows that (1) there is still information transfer from n_{sw} to PSD even after the effect of V_{sw} is removed and (2) removing the effect of V_{sw} shifts the peak of corr($n_{sw} \rightarrow$ PSD) to the left. The red dashed vertical lines help visualize the shifts of the peaks in the correlations. CMI($n_{sw} \rightarrow$ PSD| V_{sw}) has a secondary peak at τ = 80–120 hr. The mean noise and 3σ from the noise are plotted as solid and dashed green curves, respectively.

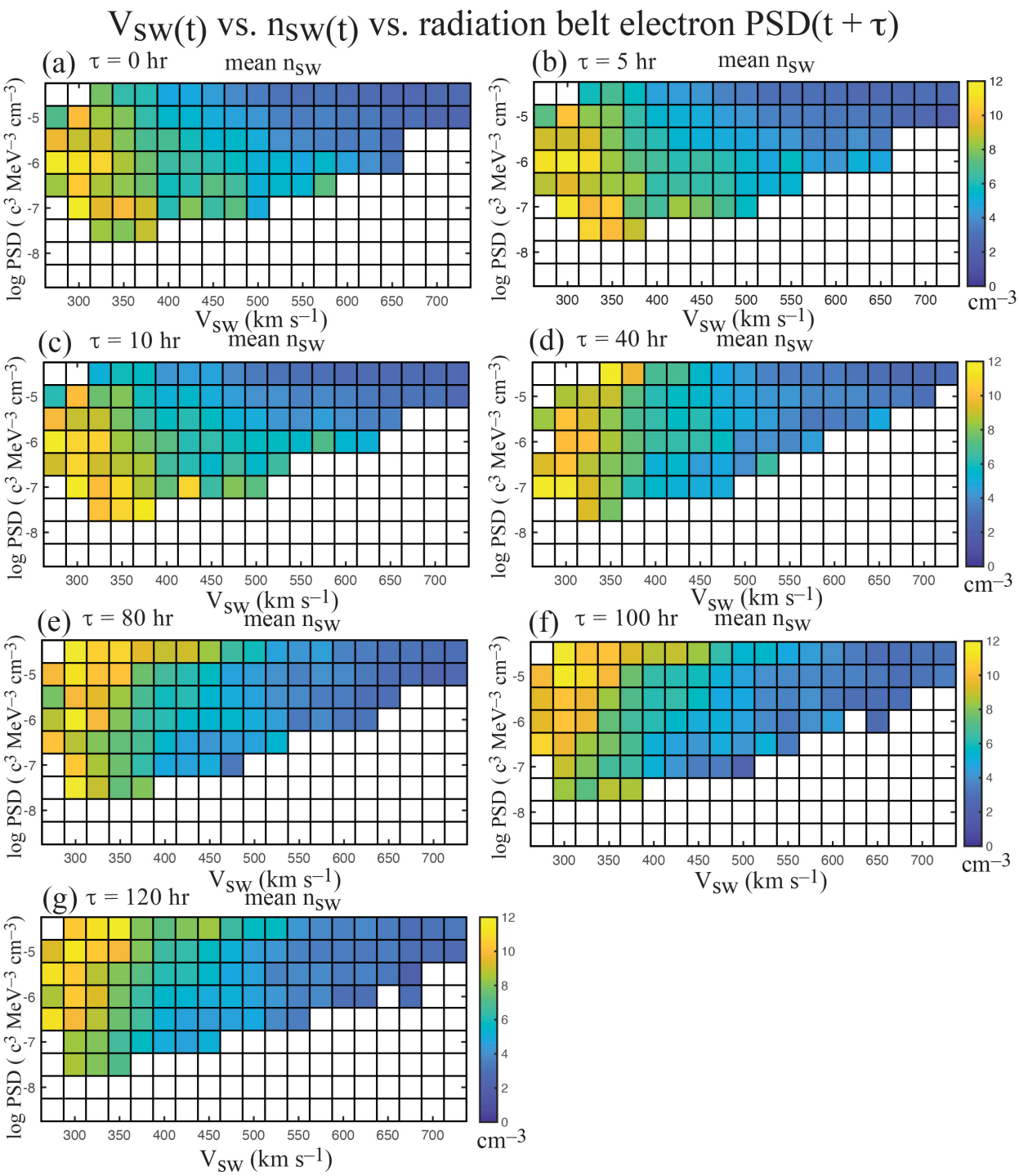

Figure 3. (a–g) log PSD(t + τ) vs. V_{sw}(t) vs. n_{sw}(t) for τ = 0, 5, 10, 40, 80, 100, and 120 hr, respectively. The color is n_{sw}. Large V_{sw} (V_{sw} > 450 km s^{-1}) corresponds to high PSD. For small V_{sw} (V_{sw} < 450 km s^{-1}), at small τ (τ = 0, 5, 10 hr), n_{sw} negatively correlates with PSD, but at large τ (τ = 80, 100, 120 hr), n_{sw} positively correlates with PSD. At τ = 40, the correlation is weak. Figure 3 is consistent with CMI(n_{sw} → PSD| V_{sw}) plotted in Figure 2e.

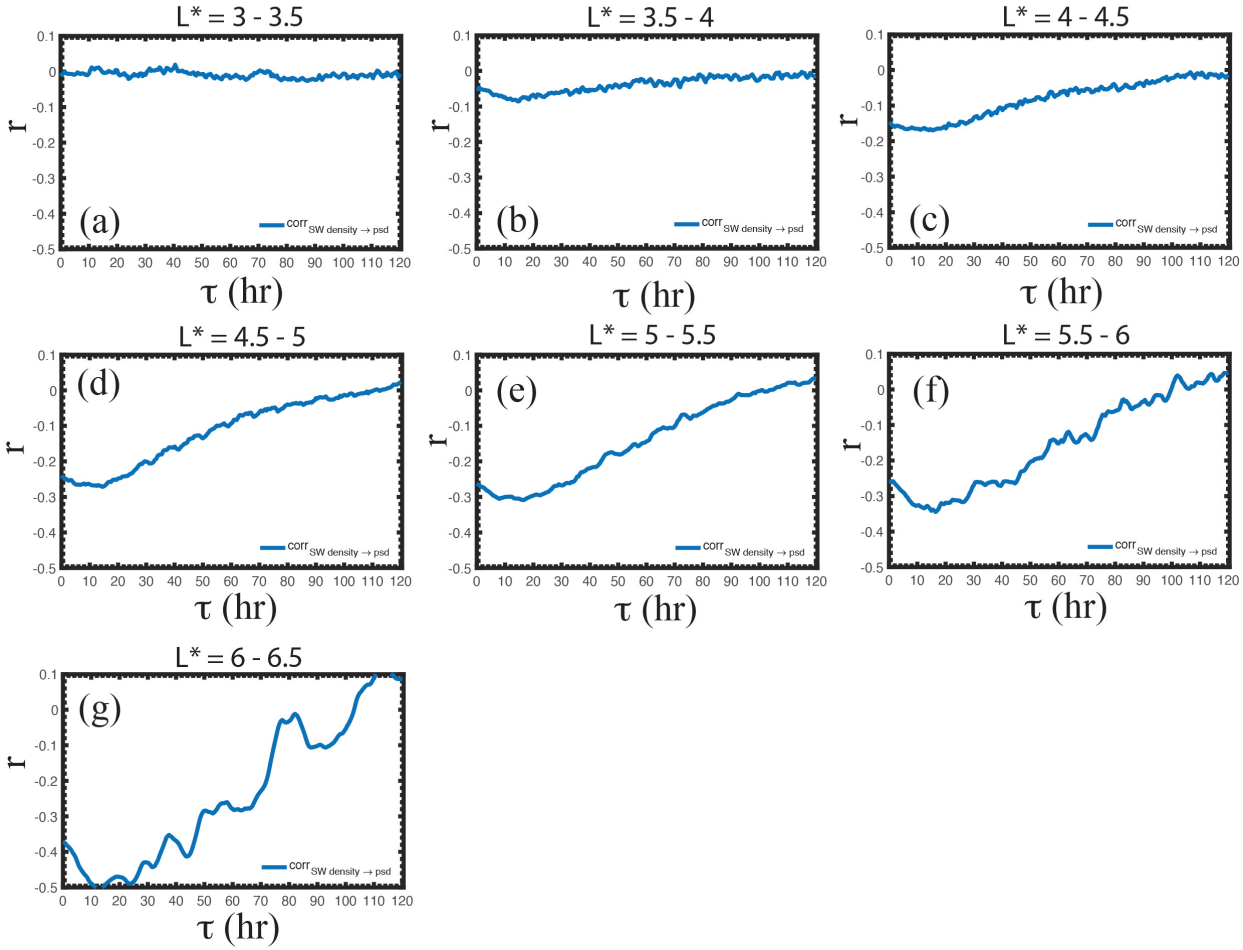

Figure 4. corr(n_{sw} → PSD) from L* = 3 to 6.5 in seven bins each with width = 0.5. (a) The correlation is insignificant at L* = 3–3.5, but slowly increases with increasing L*. (b–g) The correlations are significant ($p < 0.01$) at the minimum τ (τ = 15, 16, 17, 17, 17, 13 hr), r = (–0.086, –0.17, –0.27, –0.31, –0.34, –0.50), and n = (8,302, 11,481, 17,7891, 27,060, 6,236, 528), respectively.

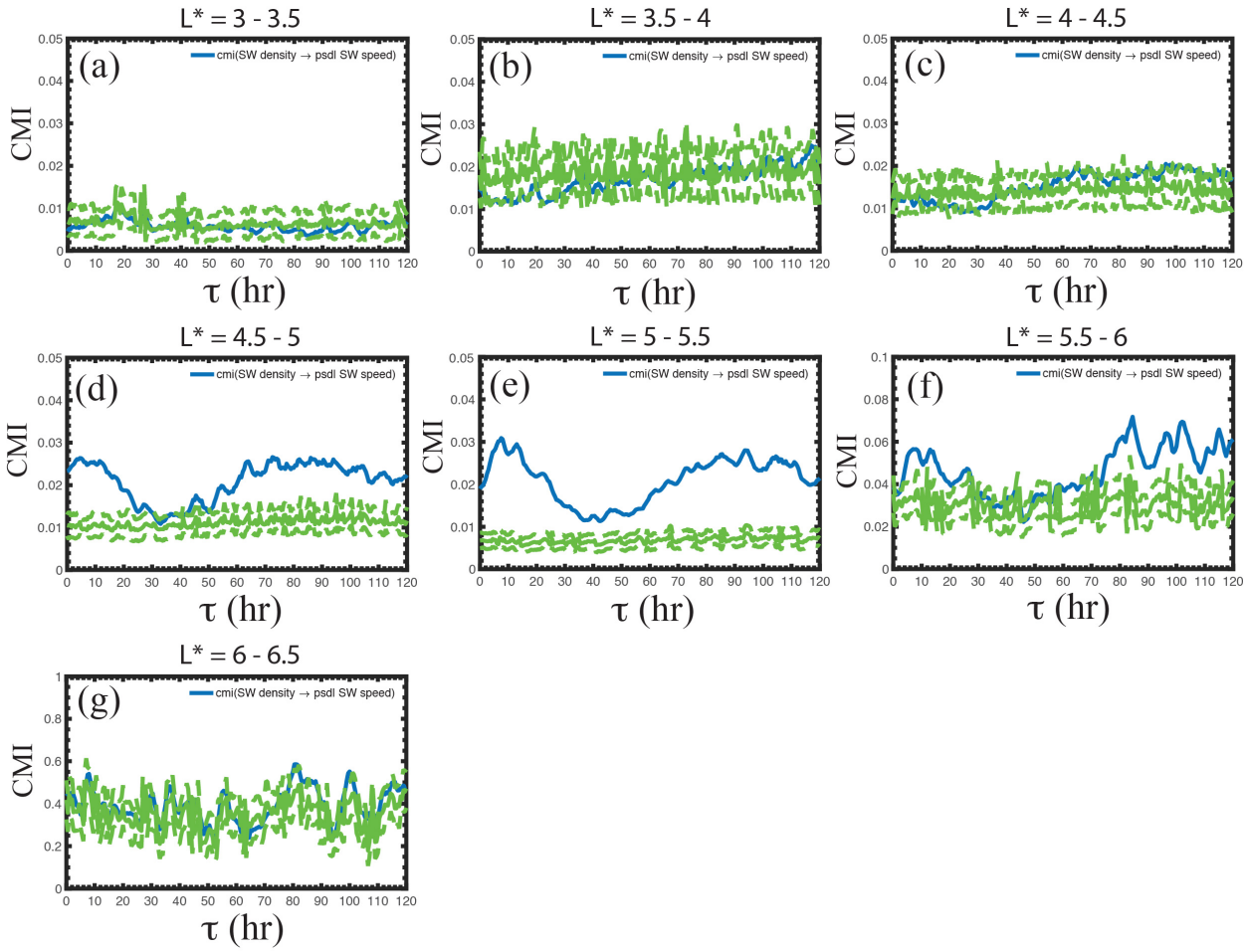

Figure 5. CMI($n_{sw} \rightarrow$ PSD| V_{sw}) from L* = 3 to 6.5 in seven bins each having width = 0.5. The mean noise and 3σ from the noise are plotted as solid and dashed green curves, respectively. (a) The CMI is at the noise level at L* = 3–3.5, which is consistent with the correlation in Figure 4a. (b–c) CMI is at the noise level at L* = 3.5–4.5, unlike the correlation in Figures 4b and 4c. (d–e) The peak CMI is significant at L* = 4.5–5.5 and (f) barely significant at L* = 5.5–6. (g) The CMI is at the noise level at L* = 6–6.5 where there is a large variability in PSD at this outermost L* layer.

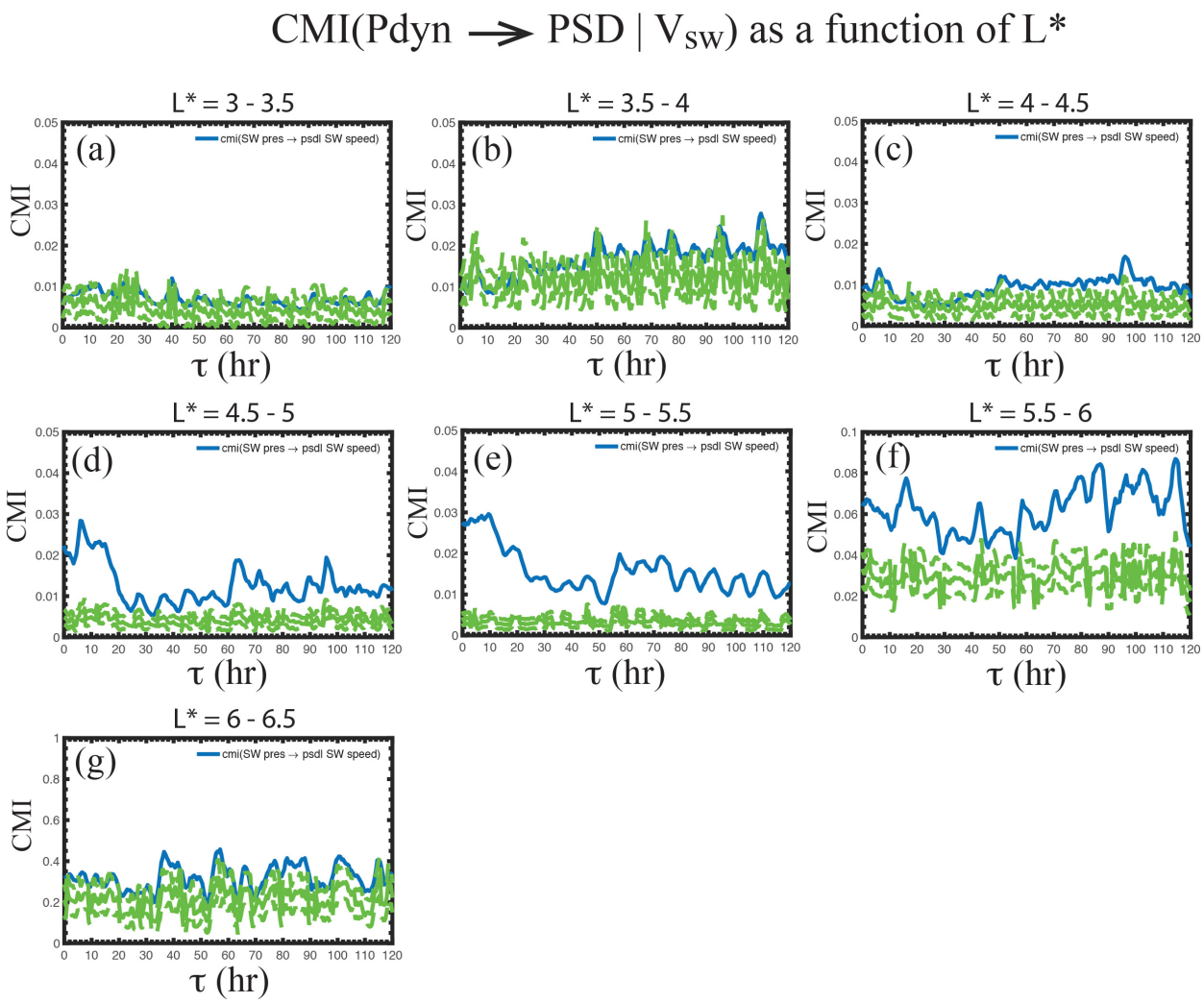

Figure 6. CMI(P_{dyn} → PSD| V_{sw}) from L* = 3 to 6.5 in seven bins in the same format as in Figure 5. The mean noise and 3σ from the noise are plotted as solid and dashed green curves, respectively. Similar to their counterparts in Figure 5 panels d–f, the primary peak CMIs are significant only at L* = 4.5–5.5 (d–e) and barely significant at L* = 5.5–6. The significances at L* = 4.5–6 are higher than their counterparts in Figure 5 panels d–f for CMI(n_{sw} → PSD| V_{sw}), suggesting that P_{dyn} is the real causal variable rather than n_{sw}. The opposite is true for the secondary peak, suggesting the causal variable is related more to n_{sw} rather than P_{dyn}.

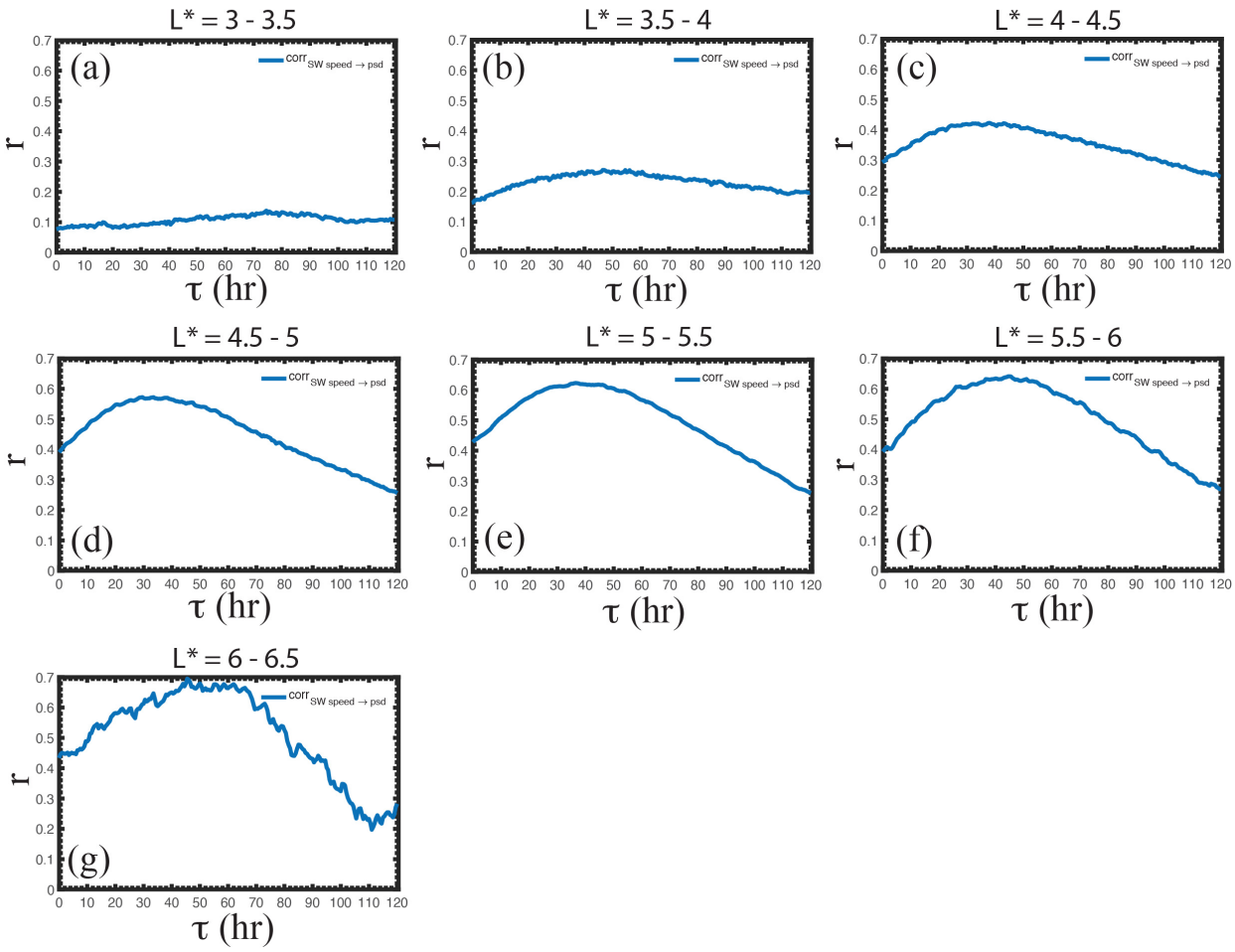

Figure 7. corr(V_{sw} → PSD) from L* = 3 to 6.5 in seven bins in the same format as Figrue 5. (a–g) The correlations are all significant at $p < 0.01$ at the maximum τ (τ = 40–120, 30–120, 38, 30, 37, 45, 30–90 hr), (r = 0.14, 0.27, 0.42. 0.57, 0.62, 0.64, 0.70) for L* = 3–3.5, 3.5–4, 4.–4.5, 4.5–5, 5–5.5, 5.5–6, and 6–6.5, respectively.

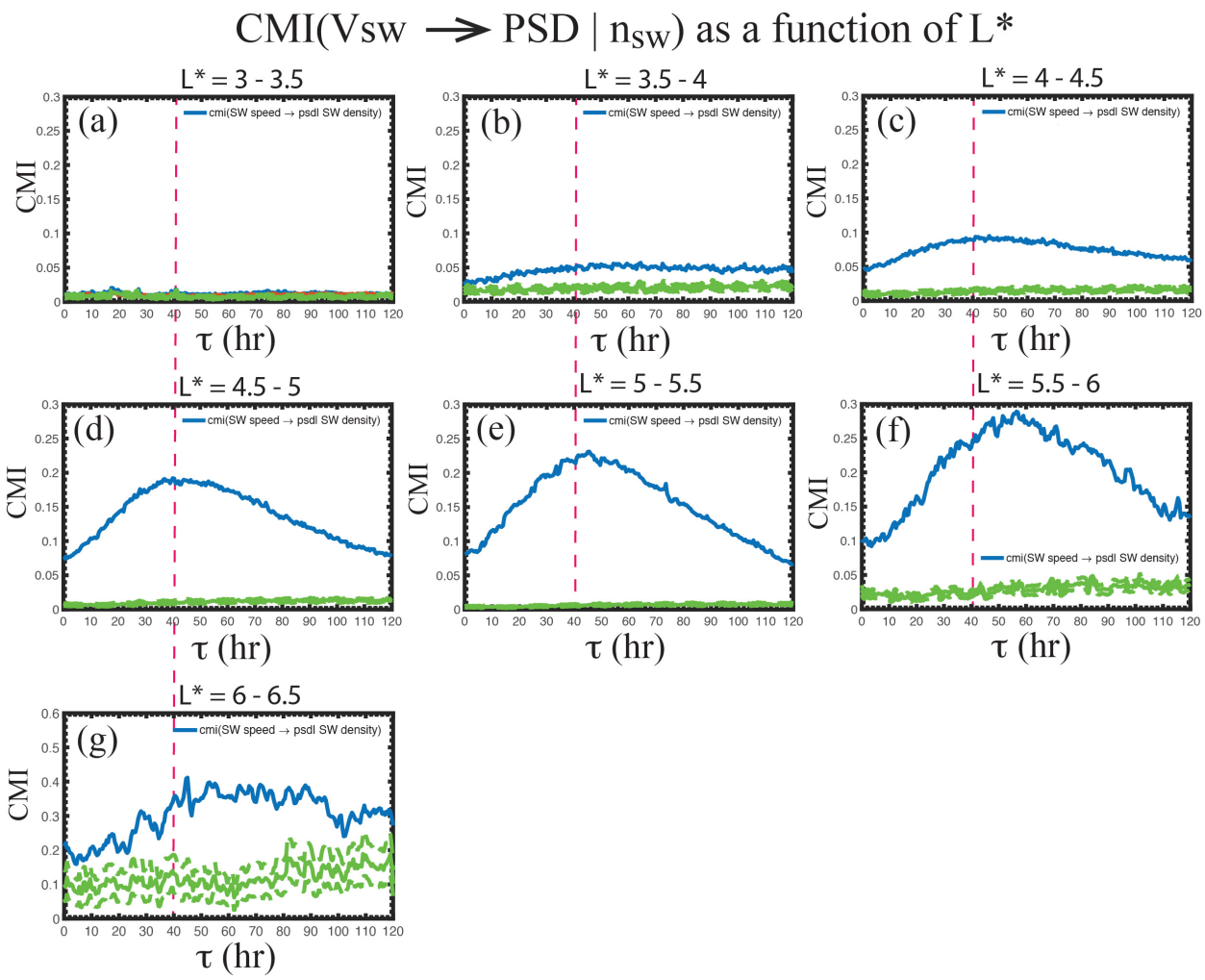

Figure 8. CMI(V_{sw} → PSD| n_{sw}) from L* = 3 to 6.5 in seven bins in the same format as Figure 5. The mean noise and 3σ from the noise are plotted as solid and dashed green curves, respectively. (a) The CMI is at the noise level at L* = 3–3.5, unlike the correlation in Figure 7a. (b–c) At L* = 3.5–4.5, the CMI has broad peaks from τ ~ 50 to 100 hr (or larger in the case L* = 3.5 – 4) and the peaks are significant. (d–f) At L* = 4.5–6, the CMI peaks are narrower (peak τ = 40, 46, 57 hr, respectively). (g) At τ = 6–6.5, the peak broadens again but remains significant.

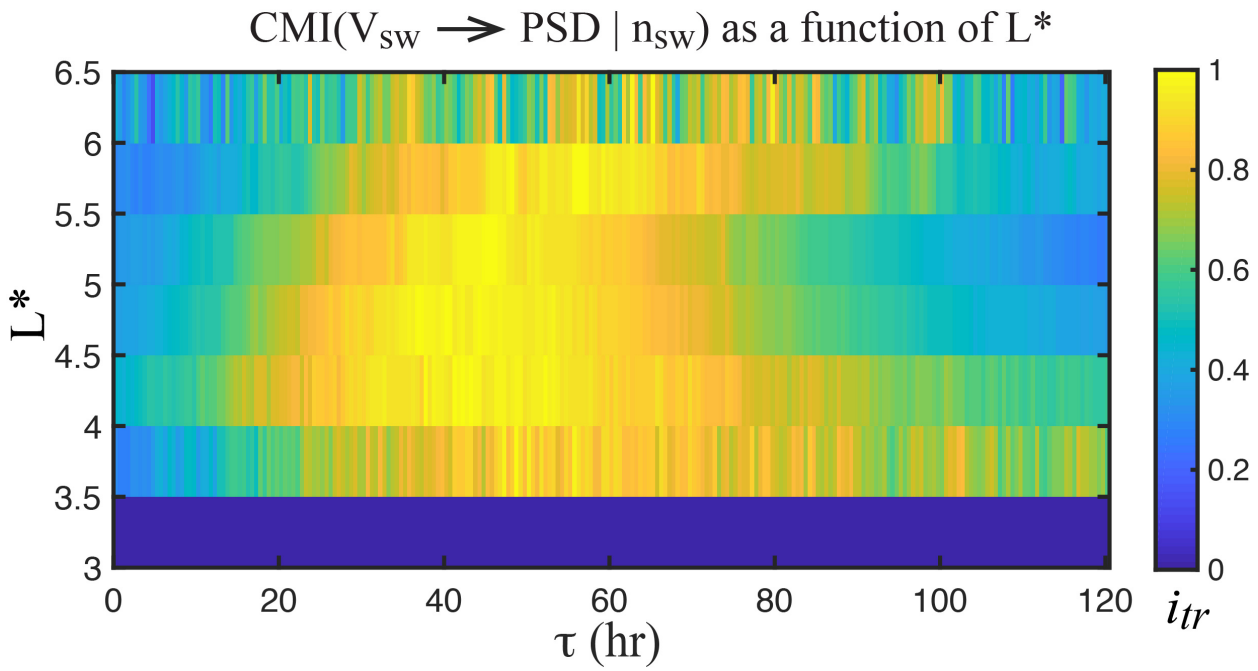

Figure 9. The normalized i_{tr} as a function of L* and τ where i_{tr} = the amount of information transferred = CMI(V_{sw} → PSD| n_{sw}) – mean noise (the blue curve subtracted by the solid green curve in Figure 8). The orange and yellow correspond roughly to the top 20% of i_{tr} in each L* bin. The smallest peak τ can be found at L* = 4.5 –5.5 where τ = 35–50 hr. The peak τ broadens and shifts to larger τ at higher L* (t = 45–65 and 40–100 hr for L* = 5.5–6 and 6–6.5, respectively) and lower L* (τ = 35–55 and 45–60 hr for L* = 4–4.5 and 3.5–4, respectively). The broadening and shifting of the peak to higher τ may suggest outward and inward diffusion from L* = 4.5–5.5. At L* = 4–4.5, peak τ starts about the same time as that at L* = 4.5–5.5, which is suggestive of local acceleration at this L* band as well.

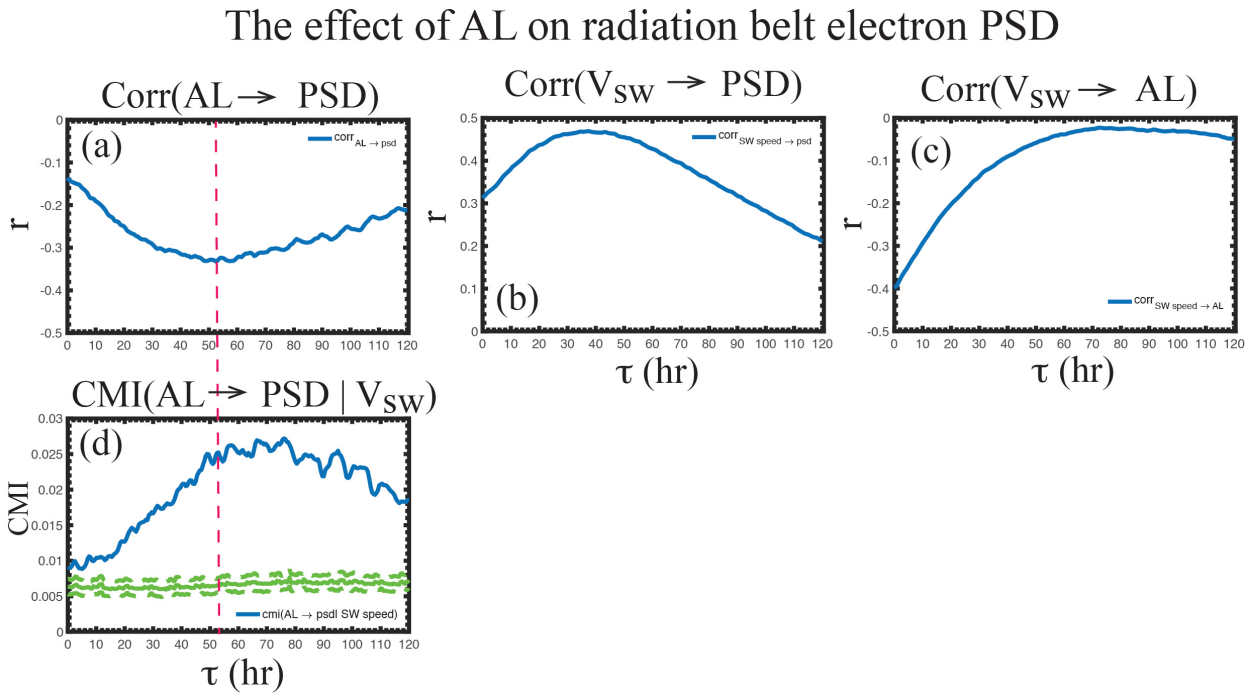

Figure 10. (a) AL negatively correlates with radiation belt electron PSD. (b) V_{sw} positively correlates with PSD (same as Figure 1a). (c) V_{sw} negatively corelates with AL. Given (b) and (c), the correlation in (a) may just be coincidental. (d) CMI(AL → PSD| V_{sw}) shows that even after the effect of V_{sw} has been removed, AL still has an effect on PSD. The mean noise and 3σ from the noise are plotted as solid and dashed green curves, respectively.

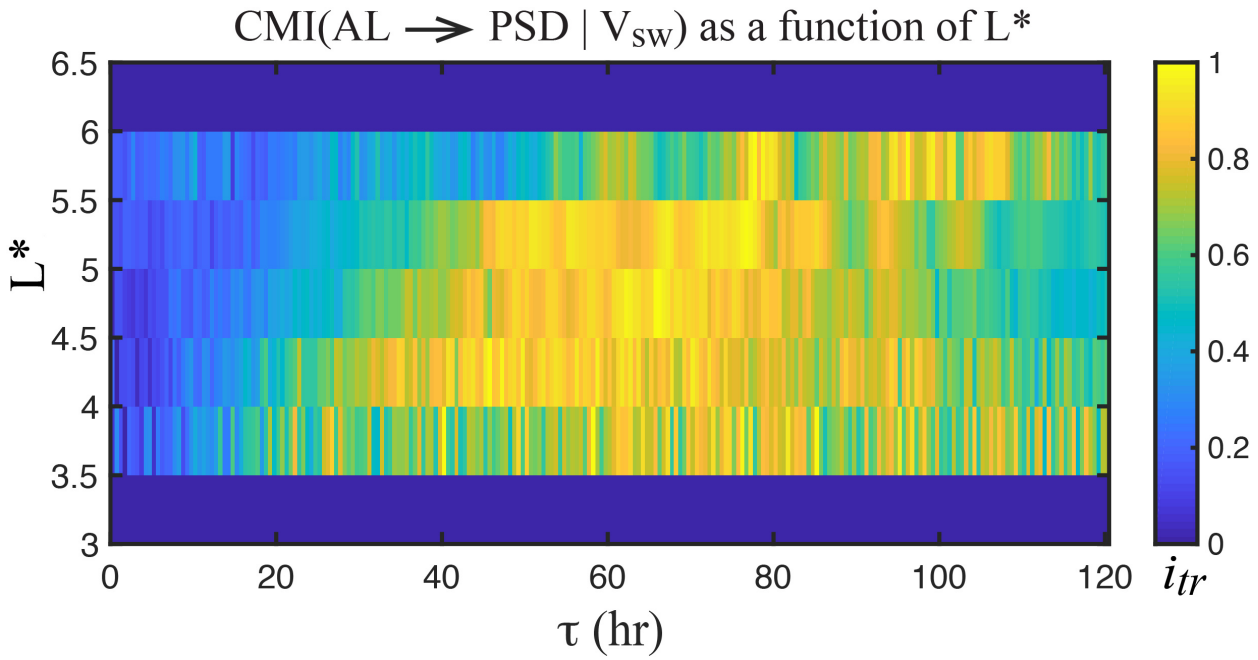

Figure 11. The normalized i_{tr} as a function of L* and τ where i_{tr} = the amount of information transferred = CMI(AL → PSD| V_{sw}) – mean noise in the same format as Figure 9. The orange and yellow correspond roughly to the top 20% of i_{tr} in each L* bin. The i_{tr} is at the noise level at L* = 3–4 and 6–6.5. The region with the largest significance is L* = 4.5–5 and 5 –5.5 with τ = 40–80 and 45–85 hr, respectively. The peak shifts to higher τ, τ = 75–100 hr, at L* = 5.5–6, suggesting outward diffusion from L* = 4.5–5.5. At L* = 4–4.5, the peak is the broad at τ = 35–80 hr. Because the peak τ starts about the same time as that at L* = 4.5–5, it may suggest local acceleration at this L*. The slow decay of τ suggests inward diffusion or longer lasting wave activity.

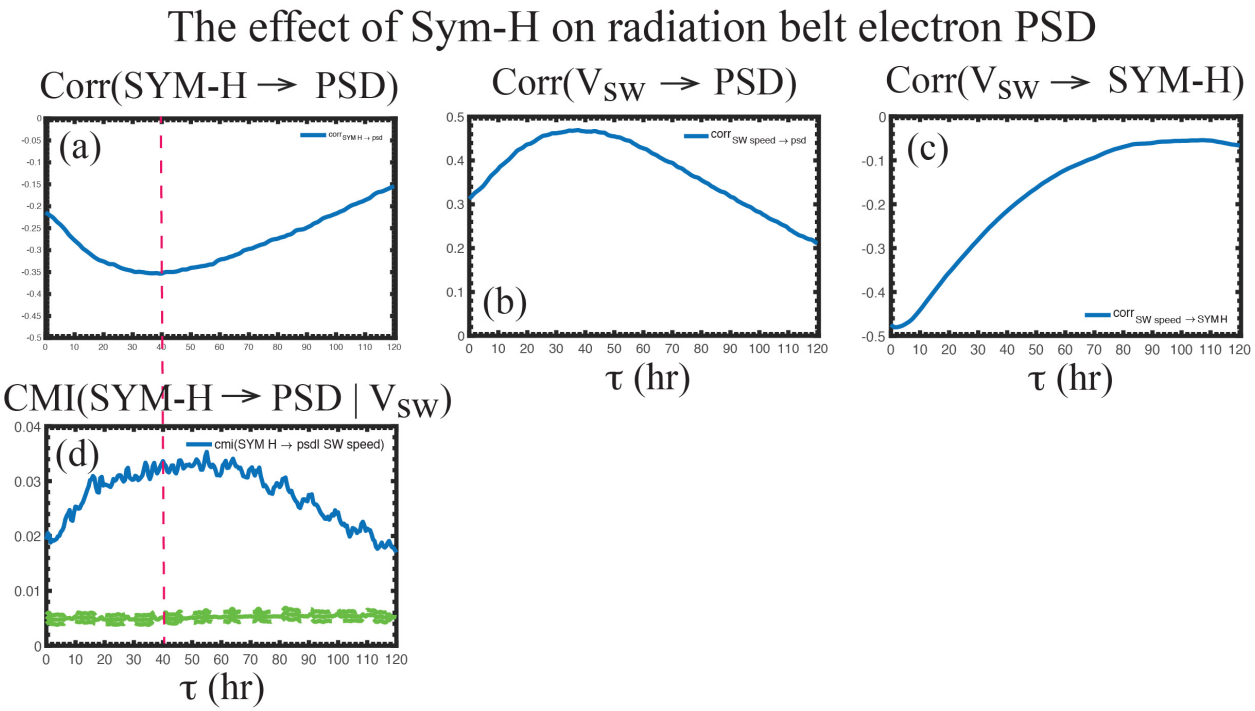

Figure 12. (a) SYM-H negatively correlates with radiation belt electron PSD. (b) V_{sw} positively correlates with PSD (same as Figure 1a). (c) V_{sw} negatively corelates with SYM-H. Given (b) and (c), the correlation in (a) may just be coincidental. (d) CMI(SYM-H → PSD| V_{sw}) shows that even after the effect of V_{sw} has been removed, SYM-H still has an effect on PSD. The mean noise and 3σ from the noise are plotted as solid and dashed green curves, respectively.

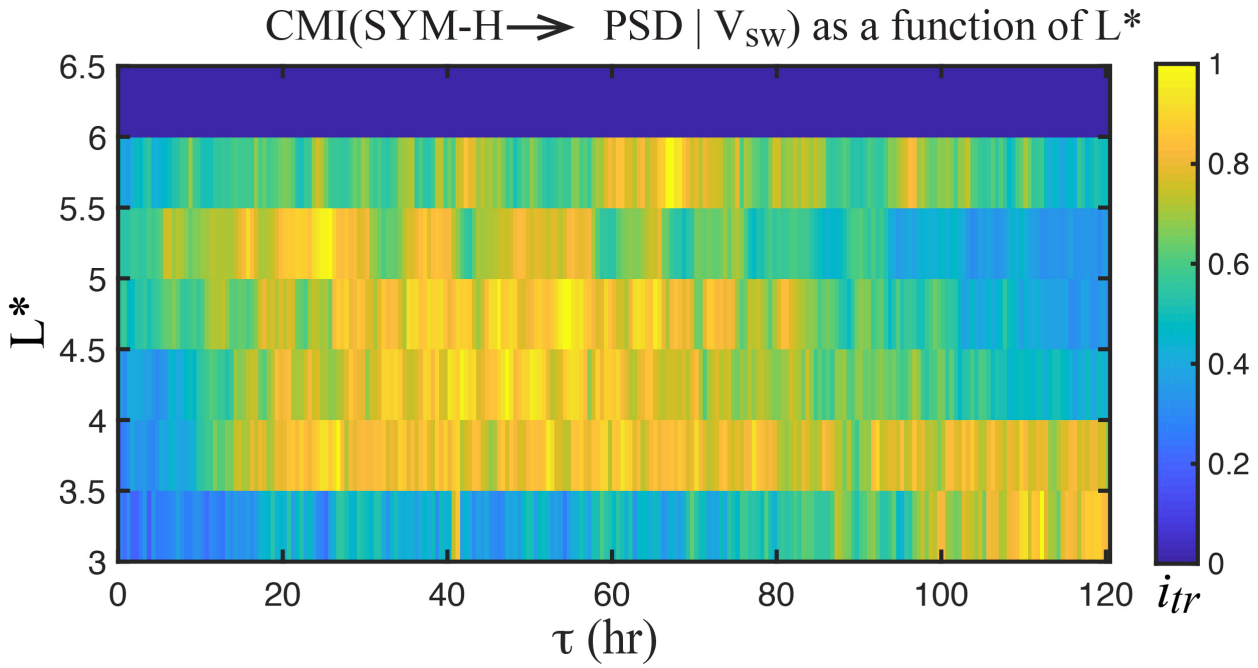

Figure 13. The normalized i_{tr} as a function of L* and τ where i_{tr} = the amount of information transferred = CMI(SYM-H → PSD| V_{sw}) – mean noise in the same format as Figure 9. The orange and yellow correspond roughly to the top 20% of i_{tr} in each L* bin. The i_{tr} is at the noise level at L* = 6–6.5 where there is a large variability in the radiation belt electron PSD. The highest peak significance can be found at L* = 5–5.5 with τ = 20–55 hr. The peak broadens and shifts to higher τ, τ = 60–75 hr at L* = 5.5–6, suggesting outward diffusion from L* = 5–5.5. At L* = 4–4.5 and 4.5–5, the i_{tr} peaks at τ = 30–60 and 30–75 hr. At L* = 3.5–4, the peak is very broad at τ = 20–120 hr, which may suggest local acceleration and inward diffusion from higher L*. At L* = 3–3.5, the i_{tr} peaks at τ = 110–120 hr or may be even higher, which may suggest slow diffusion from higher L*.